Design and Assessment of Active Heating Devices to Reduce Cold Start Emissions of Gasoline Internal Combustion Engines

---

Progettazione e Analisi di Dispositivi di Riscaldamento Attivo per Ridurre le Emissioni Inquinanti da Avviamento a Freddo di Motori a Combustione Interna a Benzina

PhD Candidate
Vincenzo Rossi

Academic Tutor
Prof. Stefano Fontanesi

Academic Co-Tutor
Prof. Alessandro D'Adamo

PhD Course Coordinator
Prof. Alberto Muscio

Abstract

In the last two decades, the growing environmental concern in many countries worldwide has prompted regulators to introduce increasingly restrictive legislation on pollutant emissions for the automotive sector. This has led to a progressive revision of emission limits and testing procedures.

Under these challenging conditions, although engine combustion optimization is fundamental to lower specific tailpipe emissions, it is not sufficient by itself; very high after-treatment conversion efficiencies from engine startup onwards are needed.

The investigation conducted in this research was a systematic exploration of the potential of active heating devices to improve the performance of exhaust after-treatment systems, especially in engine cold start conditions. This phase is crucial for emissions control, as the efficiency of the after-treatment system is significantly reduced when the engine and exhaust system are cold. The research focused on two main technologies: the electric heater and the fuel burner, both of which were tested and analyzed through a combination of numerical simulations and experimental validations after being integrated into hardware and software systems that guarantee their operation. Respectively, these systems are the Electrically Heated Catalyst System (EHCS) and the Fuel Burner System (FBS).

The definition of the EHCS layout was conducted using both 1D and 3D Computational Fluid Dynamics (CFD) simulations. These simulations were also employed to predict how effectively the EHCS could raise the temperature of the after-treatment system (ATS) to its light-off temperature. The models considered various factors, such as the electrical energy and power input, as well as the heat transfer characteristics of the after-treatment system. Preheating strategies were investigated, analyzing how activating the heater before engine startup affected the overall efficiency of the ATS. In the case of 3D simulations, they also considered the uniformity of the heater temperature distribution and the heat exchange of the heater with the surrounding environment due to radiation.

Besides the simulations, dedicated experimental campaigns took place, using a heater test rig to test a heater prototype, and an engine test bench to test the complete EHCS. The heater prototype was manufactured by an external supplier. The experiments were crucial for two main reasons: they assessed the accuracy of the simulation models and provided real-world data on the performance of the EHCS.

The research demonstrated that the EHCS could enhance the conversion of pollutants during the initial cold start phase, outperforming passive catalyst heating strategies.

In parallel with the EHCS investigations, the research also focused on the FBS. The fuel burner, a device designed to introduce a controlled flame directly into the exhaust line to rapidly increase the after-treatment temperature, was initially assessed through experimental tests conducted on a prototype manufactured by Bosch GmbH. The operation of the fuel burner was optimized to achieve a repeatable startup, stabilize combustion, minimize emissions during burner operation (burner-out emissions), and maximize thermal output. The experimental results were then used as input for simulations to predict how the burner would perform under various conditions and control strategies. These simulations were conducted in both 1D and 3D CFD environments to provide a comprehensive understanding of its operation. The simulations explored how variations in the preheating duration could impact tailpipe emissions. The geometry of the connection between the burner and the exhaust line was also optimized through simulations to ensure efficient heat transfer and minimal heat losses.

To validate these simulations, experimental tests were conducted on the complete FBS, including the burner prototype, at the engine test bench. The results demonstrated that the fuel burner could significantly reduce tailpipe cumulative emissions when compared to passive heating.

The comparative analysis between EHCS and FBS highlighted that both technologies could significantly reduce tailpipe cumulative gaseous emissions during engine cold start. The effectiveness of EHCS and FBS as active

heating technologies is based on the preheating of three-way catalyst (TWC). The duration of the preheating is a critical point for customer acceptance of the active heating technology.

Simulations indicated that a heater powered with 8 kW and a fuel burner could achieve comparable preheating durations for an equivalent reduction in tailpipe emissions. Nonetheless, supplying 8 kW per heater, especially at ambient temperatures below zero, represents a challenge, particularly for a dual-bank engine architecture that requires two heaters. Longer preheating times result from using lower power levels. Most of the computational and experimental activities were focused on using a power of 4 kW.

The fuel burner, by generating pollutant emissions itself, proved to be intrinsically less effective at lowering NOx compared to CO and HC.

From a methodological standpoint, this research has also contributed to the development and validation of simulation tools capable of reproducing complex phenomena, such as radiative heat exchange between the electrical heater and the surroundings, and the application of the Joule effect to any heater geometry. Moreover, the comparison between experimental and computational results has pointed out the necessity to improve the computational models to accurately simulate the phase transition from liquid to vapor of the water present in the exhaust line.

Through the development and optimization of the FBS and EHCS, this research contributes valuable insights into the design and operation of advanced heating systems for automotive applications. By addressing both the technical and environmental challenges associated with cold starts, this research advances the field of automotive engineering towards more sustainable and efficient future technologies.

Summary

1 Introduction

1.1 Emission legislations

Growing environmental concerns in many countries have led to the introduction of increasingly restrictive regulations on pollutants and greenhouse gas emissions from the automotive sector (Figure 1). This has resulted in a gradual update of emission standards and, simultaneously, of the testing protocols.

This regulatory process is expected to continue in the coming years, with automotive emission legislations around the world evolving toward more restrictive scenarios. This includes a significant reduction in the permissible levels of pollutants and the potential introduction of new polluting species (e.g., ammonia). Upcoming regulations are viewed as the culmination of a process that began many years ago to limit pollutant emissions from light-duty vehicles and passenger cars [1, 2, 48].

Non-Methane Hydrocarbons (NMHC), Non-Methane Organic Gases (NMOG), Carbon Monoxide (CO), and Nitrogen Oxides (NOx, consisting of NO and NO2) are regulated pollutants in many countries (Figure 1). Regulatory measures are implemented to control their emissions due to the significant impact on air quality, public health, and the environment. Total Hydrocarbons (THC or HC) are also regulated in several countries (e.g., Europe and China). THC include all hydrocarbons, encompassing methane and NMHC. NMHC specifically exclude methane, focusing on hydrocarbons that contribute more to photochemical smog and ground-level ozone formation. NMOG include not only NMHC but also other volatile organic compounds, capturing a wider spectrum of organic pollutants relevant for air quality. Particle Number (PN) and Particulate Matter (PM) are both regulated. PN refers to the number of solid particles emitted, whereas PM denotes a wide range of substances, not only solid particles but also organic compounds. These organic compounds can originate from incomplete combustion.

Current European and Chinese regulations, specifically the Euro6d and China6b standards, require the conduct of on-road tests known as Real Driving Emission Tests (RDE). The revision of these testing procedures is underway, aiming to make homologation procedures more representative of the actual conditions experienced by vehicles on the road [3].

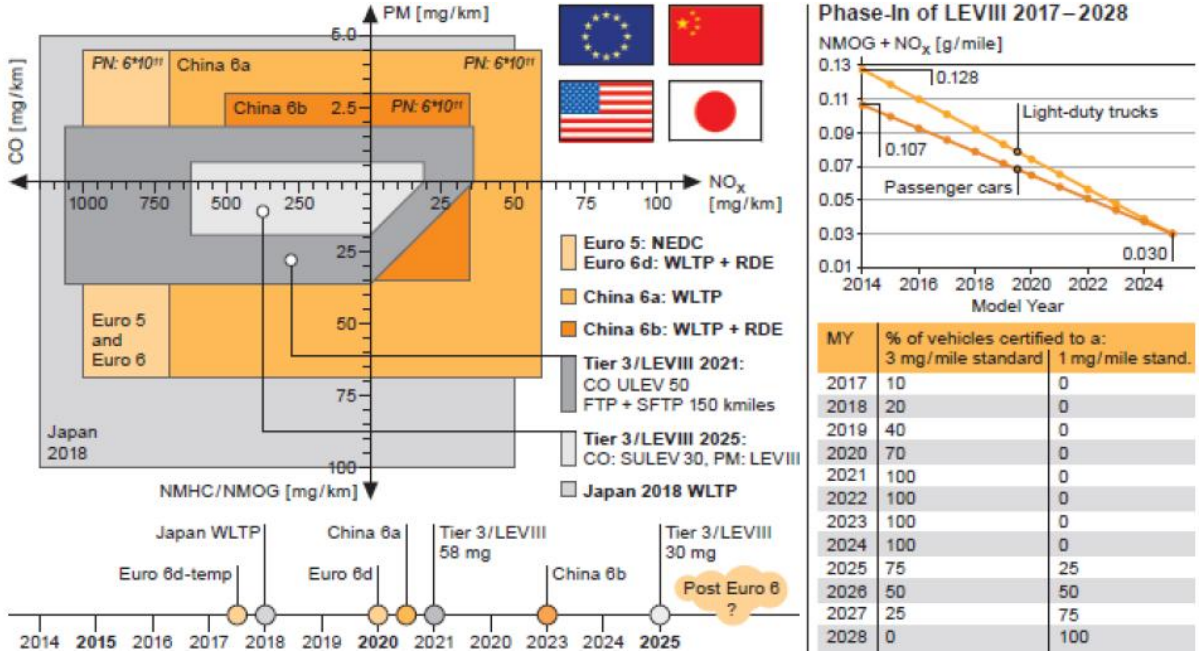

MY	% of vehicles certified to a: 3 mg/mile standard	1 mg/mile stand.
2017	10	0
2018	20	0
2019	40	0
2020	70	0
2021	100	0
2022	100	0
2023	100	0
2024	100	0
2025	75	25
2026	50	50
2027	25	75
2028	0	100

Figure 1 - Emission Limits and Phase-in Timing in the different world regions: Europe, United States, China, Japan. Source: Continental, Worldwide Emission Standards and Related Regulations Passenger Cars / Light and Medium Duty Vehicles, May 2019 [59].

In the context of road testing, numerous factors influence the pollutant emissions, including the driver's behavior, environmental conditions (such as ambient temperature, road slope, and altitude), and road conditions, which also encompass traffic density. Under these complex conditions, achieving very high after-treatment conversion efficiencies right from engine startup is essential, particularly at low ambient temperatures (engine cold start).

Furthermore, current trends in automotive propulsion design, largely driven by the hybridization of power units, pose new challenges for emission control. For instance, the frequent starting and stopping of the engine in hybrid vehicles adversely affects the thermal management of the after-treatment system (ATS). This makes it harder to achieve and maintain the ATS above the minimum temperature thresholds that ensure its proper functioning (e.g., three-way catalyst light-off temperature).

1.2 After-treatment systems for gasoline internal combustion engines

Regarding gasoline spark-ignition internal combustion engines (SI-ICE) operated under stoichiometric conditions, the most common after-treatment setup relies on three-way catalytic converter (TWC) to reduce gaseous pollutant emissions, paired with gasoline particulate filter (GPF) to reduce particulate matter emissions.

TWC works by catalyzing chemical reactions that convert gaseous pollutants generated by engine combustion into harmless substances. GPF captures and stores exhaust particulates generated by the engine (mainly soot). Over time, the GPF heats up and burns off the soot (a process known as GPF regeneration), ensuring efficient operation.

TWC consists of two components (Figure 2): a substrate (typically a ceramic or metallic monolithic honeycomb) and the washcoat applied to the substrate's walls. The washcoat consists primarily of a carrier (γ-Alumina), Cerium-Zirconium Oxides (CeO2-ZrO2), and noble metals as active sites [4].

The substrate geometrical and physical characteristics, particularly the geometric surface area (GSA) in contact with the exhaust gas and the heat capacity, play a crucial role in determining the efficiency of the converter. Indeed, the choice of γ-Alumina is driven by the need to increase the substrate GSA. γ-Alumina is a suitable choice due to its high surface area and good thermal stability under the exhaust hydrothermal conditions.

Cerium-Zirconium Oxides are primarily added as oxygen storage promoters; they enable the storage and release of oxygen under lean and rich conditions, respectively. By exploiting this oxygen buffering effect, TWC can operate at very high conversion efficiencies over a wider range of air/fuel ratios typical of engine transient operation [5, 6].

Noble metals (Platinum (Pt), Palladium (Pd), and Rhodium (Rh)) are the most commonly used catalysts in TWCs and they are dispersed as active sites within the γ-Alumina high surface area. They catalyze the chemical reactions occurring on the coated walls of the substrate.

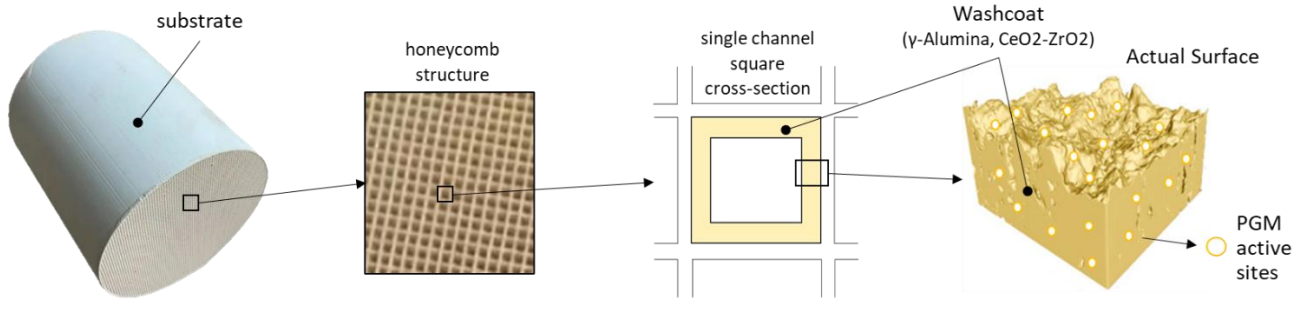

Figure 2 - Three-way catalyst components: substrate and washcoat. Washcoat sub-components: γ-Alumina, Cerium-Zirconium Oxides (CeO2-ZrO2), and noble metals (Platinum Group Metals – PGM)

TWC is effective at relatively high temperatures (light-off temperature of 500-600 K, [7]) and, therefore, does not guarantee sufficient pollutant conversion at engine cold start [8]. Indeed, it is during this phase that most of

tailpipe emissions are produced [9]. Similar conditions affect the ATS performance for vehicles with different levels of hybridization: the successive shutdowns of the ICE and the low-load operations have a negative impact on the exhaust line conversion efficiency, as the catalyst temperature is significantly reduced [10, 11]. To address these critical conditions, much effort is dedicated to improving the thermal management of the catalyst and consequently the ATS performance.

Different strategies have been explored to speed up the catalyst light-off. Engine-based catalyst heating strategies are widely used to heat up TWCs (passive heating strategies). These strategies enable TWC to quickly reach the light-off temperature, though at the expense of increased fuel consumption. In fact, they intentionally reduce engine combustion efficiency to increase the energy content of the exhaust gas.

A low thermal mass TWC facilitates rapid light-off, especially when located close to, or even integrated into, the exhaust manifold (close-coupled TWC). This configuration requires the availability of a thermally stable washcoat to handle the extreme temperatures of engine-out exhaust gases [8].

Highly porous cordierite monoliths have been shown to improve performance of TWCs by increasing the available surface area for washcoat deposition and reducing heat capacity. A lower wall thickness, combined with high cell density, can lead to significant improvements in light-off performance [12, 13].

Nakanishi et al. [14] proposed reducing the heat capacity of the washcoat. The results have revealed that the temperature of the TWC rises quickly and that this could reduce tailpipe emissions by 25% compared to the reference TWC in the FTP driving cycle.

The effect of increasing Pd loading on TWC performance has been investigated under conditions simulating the real exhaust gas composition of gasoline engines. The light-off temperature can be reduced by increasing the Pd loading; however, this positive effect tends to diminish for large amounts of Pd, mainly due to the associated decrease in Pd dispersion [15]. In order to increase the number of active sites, emerging technologies, which are far from industrial production, are targeting atomically dispersed catalysts with single-atom-layer catalysis as the ultimate goal [16].

Located upstream of the TWC, HC adsorbers are used to collect hydrocarbons emitted during cold start. Once the TWC has reached light-off, the trapped HCs are released and converted in the TWC [17, 18, 19]. The performance of HC adsorbers is limited by a lack of thermal stability (exceeding 800-850°C is not allowed) required in gasoline exhaust applications. Kiefer et al. showed good results in using the HC adsorber, but their configuration required additional heating through a downstream electric heater to ensure that the catalytic converter can achieve high conversion efficiencies during the HC desorption phase [20].

Energy sources independent of the ICE can be used to heat up TWC through so-called active heating devices.

1.3 Active heating devices

Active heating devices for heating up a TWC include electric heaters (herein referred to as ‘heaters’ or ‘electrically heated catalysts’), which are integrated directly into the exhaust system to rapidly heat TWC during cold starts by means of Joule effect. Another family of devices is represented by fuel burners (herein referred to as ‘burners’). Burners introduce additional heat into the exhaust stream to heat TWC by burning a small amount of fuel directly in the exhaust line. Active heating devices can heat TWC even before engine start (preheating), resulting in very high pollutant conversion efficiencies from engine startup onwards.

1.3.1 Electric heaters

Going back to the origins, heaters were used in low-volume production in the Alpina B12 and subsequently in the BMW 750i [21, 22]. The implementation of a 12V electrically heated catalyst (EHC) led to more than 90% reduction in CO emissions and approximately 70% in HC emissions, compared with the series system, while maintaining NOx emissions unchanged. This technological improvement was a critical step in complying with stringent emission regulations without major modifications to the vehicle’s battery and alternator. The

production of heaters was relatively low since alternatives, such as engine-based catalyst heating strategies (passive heating), have been sufficient in most cases to comply with regulations.

Over the years several suppliers have presented their own heater concepts. The structures of the heaters differ from one another but can be classified into two well-defined types. The first type involves one (or more) electrically heated thin discs with different internal geometries: honeycomb made of wrapped metallic foils [23], grid of metallic wires [24], or monolithic honeycomb made of metallic alloy [26, 27, 28]. The metallic thin discs are heated by the Joule effect, and then the heat is transferred to the aftertreatment positioned nearby. The second type involves the direct heating of part of the aftertreatment by the Joule effect through electromagnetic induction (e.g., a metallic coil is wrapped around the substrate, which is equipped with inner electrical conductors [25]), or the substrate itself is made of a material that conducts electricity and is subjected to a voltage [29].

Presti et al. [23] developed a heater (heater element in Figure 3), designed as an integral part of the catalyst. The heater was mechanically supported by the downstream catalyst (support catalyst in Figure 3) by means of supporting pins and coated similarly to the support catalyst.

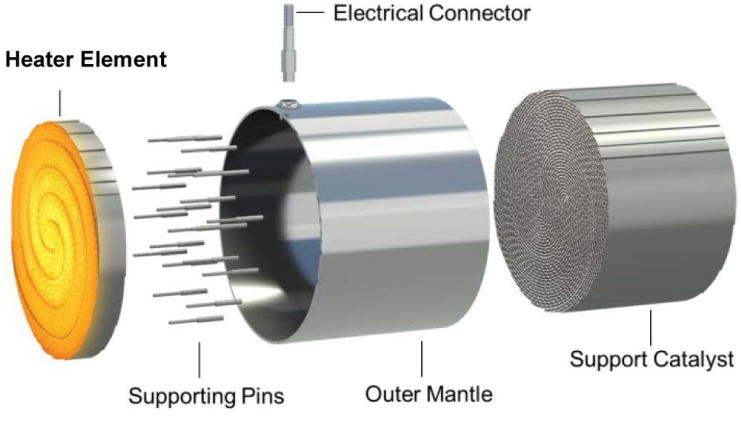

Figure 3 - Design of an integrated electrically heated catalyst (EHC). Source: EMITEC [23].

Faurecia [24] proposed a heater concept made of a TWC sandwiched between two heating metallic grids. This arrangement enabled the TWC to benefit from the heat generated by both sides.

Boger et al. [28] put in evidence the importance of uniform heating of the monolithic honeycomb to ensure that the TWCs positioned immediately downstream could reach their operational temperature as rapidly as possible. The heater structure can originate local hot spots which may be problematic from the mechanical stress point of view. This is especially true for heaters of the second type, where the volume to be heated is notably larger. Sadamitsu et al. [29] introduced a direct heating EHC using ceramic materials. This innovation allowed the catalyst to reach its light-off temperature in approximately 50 seconds before engine start-up (preheating), significantly reducing emissions. By arranging electrodes in a specific pattern and optimizing the electrical resistance of materials, the researchers managed to achieve uniform heating of the substrate's circular cross section.

By lowering the thermal inertia of the heater, its warming up is accelerated (for a given electrical power), consequently, the electrical energy consumption can also be reduced [23, 30-32]. The heater can be coated (with catalytic material); in that case, it is important to evaluate the trade-off between the beneficial presence of catalytic activity directly on the heater and the increase in thermal inertia.

Socha et al [30] demonstrated that preheating the heater, with or without the combined use of air injection upstream the heater (by a secondary air pump), leads to a remarkable reduction in HC and CO emissions. They also highlighted that positioning the heater close to the TWC is key factor in achieving low emissions efficiently.

Laurell et al. [33] emphasized the importance of preheating strategies and the integration of EHC with hybrid powertrains to enhance emission performance. Additionally, they explored preheating while charging the vehicle, showcasing different approaches to maintain or increase the ATS temperature. Hofstetter et al [39] investigated the trade-off between emission reduction and electric energy consumption in hybrid vehicles. Particularly, one of the tested strategies utilized a higher initial State of Charge (SOC) to lessen engine load and reduce NOx emissions. It was found by Sivakumar et al. [40] that preheating the TWC with a heater, led to a reduction in the SOC of the battery, necessitating more frequent engine starts which, in turn, increased the fuel consumption.

1.3.2 Fuel burner

The burner technology, similarly to the heater, was investigated in the early nineties by Hepburn et al. [34] and Polat et al [35]. It was found by Ford that the burner enabled the TWC to reach light-off within 15 seconds, leading to a 60% reduction in HC emissions during engine cold start. Challenges such as safety, durability, and system integration were identified as areas needing further research and development.

In the Polat et al. research as well, the burner provided substantial reductions in emissions. Specifically, the burner system achieved a reduction in cold start emissions exceeding 80% for HC and over 90% for CO. However, at that time, significant production-oriented development programs for gasoline applications were not carried out.

Hepburn et al. also compared burner and heater performances. The burner showed distinct advantages in terms of thermal output, providing up to 20 kW of power compared to the heater 2-3 kW. Tailpipe HC emissions during the first 60 seconds of the FTP cycle were nearly 50% lower with the burner system compared to the heater system.

In 2006, Zu Schweinsberg et al. [36] resumed the development of a burner to replace engine-based catalyst heating strategies. The burner achieved approximately 50% of the EU4 European emission standard without additional fuel consumption due to its operation. Positioned in front of the TWC for quick light-off, it consisted of a combustion chamber, a fuel/air mixing system (burner nozzle), and an ignition device (spark electrode).

A schematic of the complete burner system is shown in Figure 4. The temperature sensor checks whether the burner is operating. A secondary air pump delivers the air, and a check-valve (secondary air shut-off valve) at burner nozzle air inlet prevents backflow when the burner is off. The burner fuel supply consists of two solenoid valves: the fuel shut-off valve close to the burner nozzle and the fuel regulator near the engine's fuel supply. Since the engine fuel pressure can be considered constant (approximately 5 bar), the fuel flow can be controlled by varying the fuel regulator pulse width. A high-power ignition coil is used to generate ignition sparks. By burning fuel in the burner combustion chamber, a heat flux is generated and supplied to the TWC.

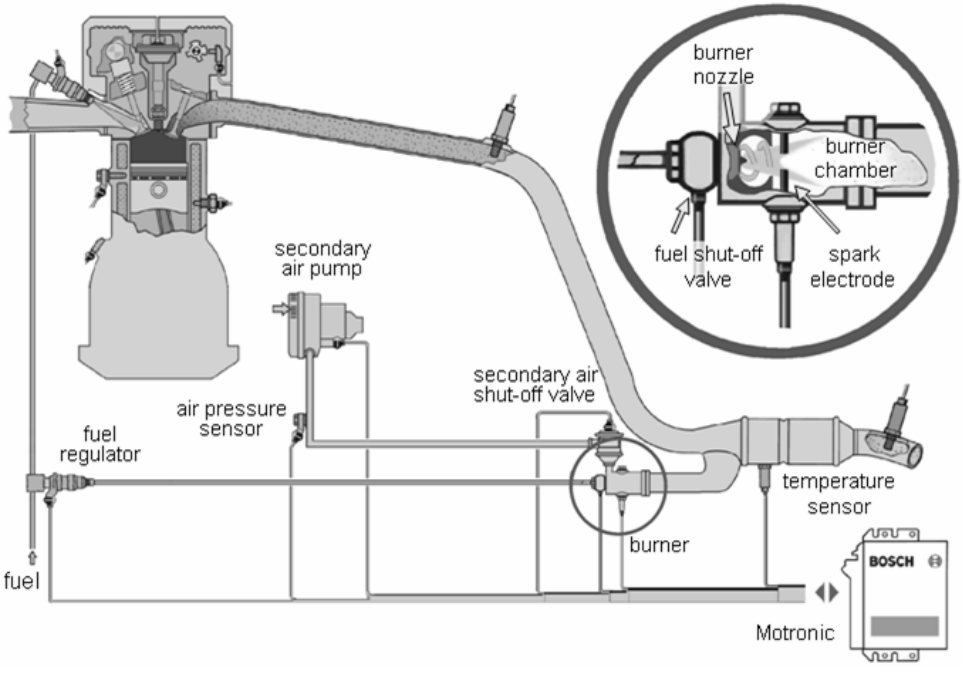

Figure 4 - Schematic view of the complete burner system proposed by Zu Schweinsberg et al. in 2006 [36].

In 2020, burner was again considered by Pauer et al. [37] as a valuable technology to meet very low emissions targets. In this evolution of the burner concept, the fuel injector was directly connected to the combustion chamber (Figure 5). The burner operated independently of the engine and was activated even before engine startup. With an adequate preheating duration, the TWC light-off was achieved before engine startup. Furthermore, burner calibration was less complex than engine-based catalyst heating strategies and significantly more effective. Bosch highlighted the opportunity to apply the burner to keep the catalyst warm and heat up the exhaust gas during the regeneration of the GPF. Emission tests performed at -7°C with a burner preheating time of 3 seconds showed a reduction in gaseous emissions of HC, CO, and NOx by 45-60% in the first 200 seconds.

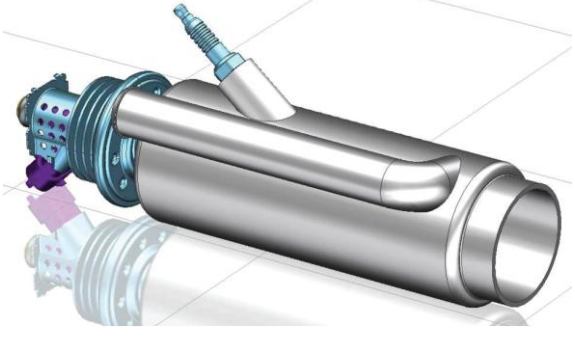

Figure 5 - Burner Model presented by Pauer et al. in 2020 [37].

In recent years, Postrioti et al. [41] and Battistoni et al. [42] developed novel burners for gasoline and diesel applications, respectively. The development was focused on achieving stable and clean combustion by means of a swirled fuel atomizer. Recirculation zones in the burner combustion chamber, facilitated by swirling flows, were crucial for the fuel atomization and stabilization of the flame.

Tenneco Inc. [43] explored the use of a burner to preheat an ATS designed for diesel engines, consisting of a DOC (Diesel Oxidation Catalyst), a DPF (Diesel Particulate Filter), and an SCR (Selective Catalytic Reduction). Testing confirmed that preheating coupled with active burner operation during engine cold start could significantly warm the DOC and DPF, leading to SCR catalyst activation within the first 100 seconds. This approach demonstrated potential for reducing NOx emissions, especially in engines without EGR.

1.4 Research description

In this research project, two active heating devices, the heater and the burner, were investigated. To transition these individual devices into fully operational systems, a comprehensive approach was necessary, involving the integration of auxiliary hardware and software components. These components were designed to work together to meet the objectives of enhanced performance and efficiency. Consequently, the Electrically Heated Catalyst System (EHCS) and the Fuel Burner System (FBS) were defined.

These systems were advantageous in reducing emissions during the critical initial phase of engine operation (engine startup in cold conditions), where TWCs are not yet effective due to low temperatures.

Concerning the EHCS, the focus was on characterizing the heat exchange phenomena among the heater, after-treatment, and the surrounding environment, and on optimizing the parameters that enhance its performance, including the electrical power and energy necessary for its operation.

The FBS underwent detailed analysis to assess its characteristics and operational capabilities. This analysis included evaluating trade-offs among various factors such as burner combustion stability and emissions, the time required for preheating, and the heat flux generated by fuel combustion. Considerations were made to ensure optimal fuel delivery and combustion processes, focusing on achieving rapid heating of the after-treatment system during cold starts.

In-depth investigations were conducted through numerical simulations (1D and 3D CFD environments) and experimental methodologies. Numerical simulations provided a theoretical framework and predictive insights into the systems' behaviors under various conditions, while experimental approaches ground these insights in real-world performance and operational parameters. This dual approach ensured a robust understanding and validation of the FBS and EHCS designs and functionalities.

A comparison between EHCS and FBS, which includes a comprehensive characterization of the heater and burner devices, the definition of their respective system layouts, and the optimization of operating strategies through both numerical and experimental approaches, has no correspondence in the scientific literature. In the literature (Par. 1.3), only some of the aforementioned aspects are addressed, focusing on one of the two technologies, and a direct comparison of the two technologies is almost absent. Hepburn et al. [34] compared burner and heater performances, but only to a limited extent.

1.4.1 Electrically Heated Catalyst System (EHCS) description

Figure 6 illustrates the components of the EHCS. The heater is a thin cylindrical monolithic honeycomb made of metallic alloy with a cell density of 400 cells per square inch (cpsi), it is connected to an outer mantle (welded to the exhaust canning) and electrically isolated from it (Figure 6.c). The heater can be coated with catalytic material, although in this research, an uncoated heater was tested. A dedicated heater Control Unit (HCU) connects the heater to a battery with a nominal voltage of 48V. The HCU modulates the power from the battery following strategies defined in the Engine Control Unit (ECU). Both control units are powered by a 12V battery. In this research, the heating power ranged from 4 to 8.6 kW.

The ATS is composed of two TWCs in a row, TWC1 and TWC2, followed by a GPF. TWC1 is designed to have low thermal inertia allowing for quicker heating. TWC2 is larger in volume compared to TWC1 and, due to its high geometric surface area (GSA), can guarantee high conversion efficiencies even under very high flow rates, where the mass transfer from the exhaust gas to the TWC walls is crucial. The GPF is uncoated, therefore it doesn't support the TWCs in the conversion of gaseous pollutants, but operates solely on particulate trapping.

Along the secondary air path, connected to the exhaust line, several components are present: a check valve, a flow meter, a secondary air pump (SAP), and a filter. The SAP, by generating a predetermined airflow within the exhaust line, supports the heat transfer from the heater to the TWCs positioned downstream. The check valve, when closed, ensures the seal of the exhaust line when secondary air is not required. The filter prevents the intake of impurities

from the engine compartment. The heater can be positioned in two ways: upstream TWC1 or between TWC1 and TWC2 (POS1 and POS2 in Figure 6).

The heater enables the heating of the ATS before the engine start (preheating) with or without the use of secondary airflow (herein referred to as 'airflow'). Indeed, even in the absence of airflow, the heater can reach temperatures high enough to heat the inlet surface of the downstream TWC by radiation. Once the engine is started, if the heater is still powered by electricity, it can contribute to the heating of the after-treatment system (postheating).

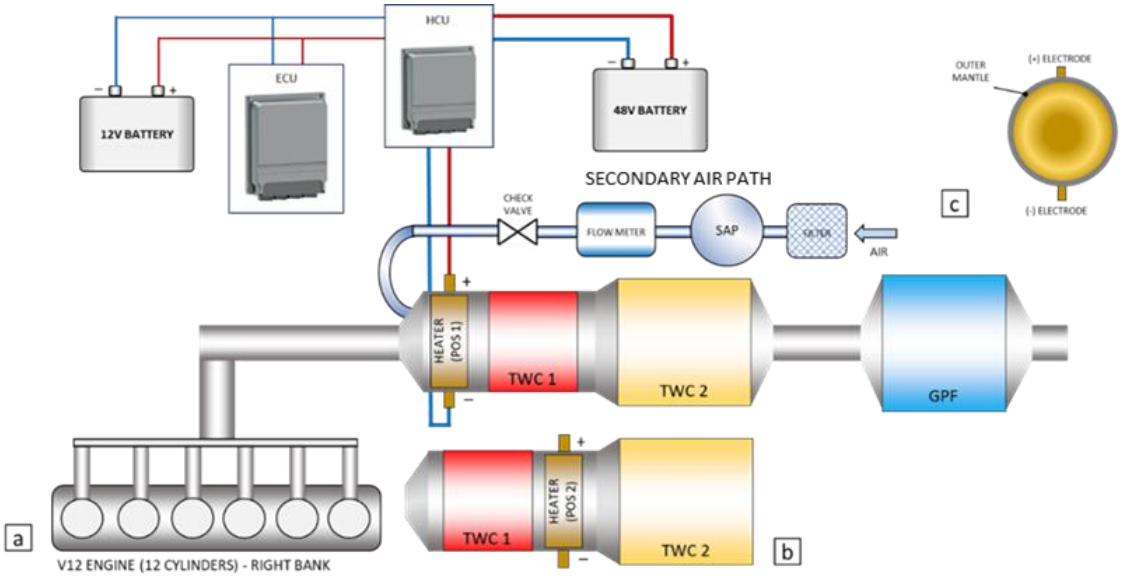

Figure 6 - Schematic view of the Electrically Heated Catalyst System (EHCS) with two possible layouts: (a) heater position upstream of TWC1 (POS1), (b) heater position between TWC1 and TWC2 (POS2), (c) heater front view.

The catalyst heating strategy consists of up to three phases (Figure 7 and Table 1):

1. zero-flow preheating - engine off, no airflow and check valve closed.
2. airflow preheating - engine off, airflow on and check valve open.
3. postheating - engine on, no airflow and check valve closed.

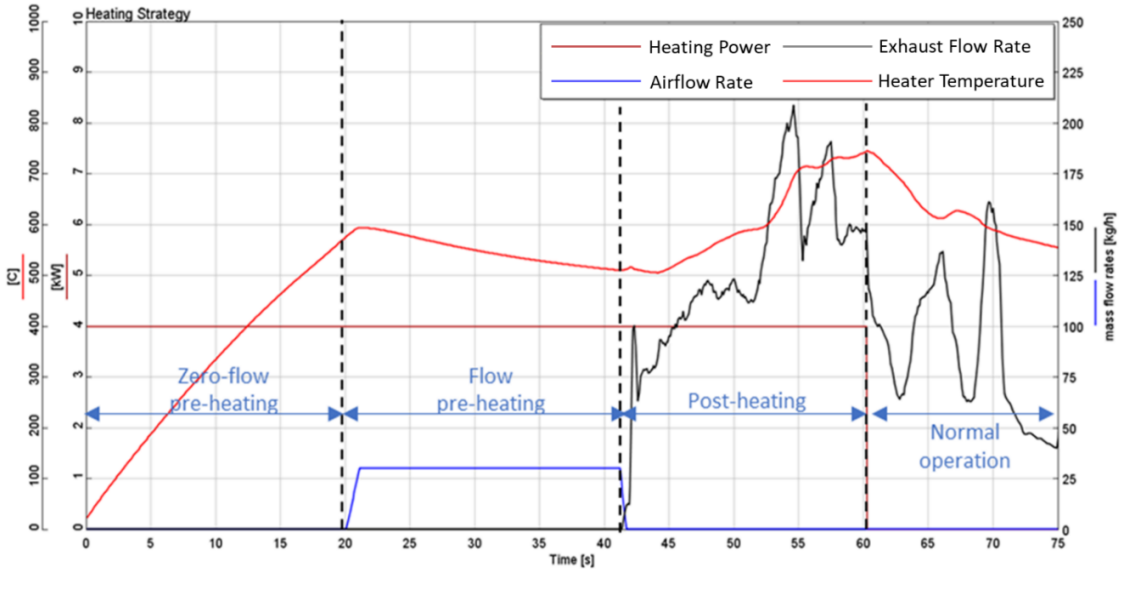

Figure 7 - EHCS catalyst heating strategy example: heating power 4 kW, 20s of zero-flow preheating, 20s of airflow preheating (airflow rate 30 kg/h), 20s of postheating.

Strategy Description				
Phase	**Engine status (ON/OFF)**	**Heater status (ON/OFF)**	**SAP status (ON/OFF)**	**Check Valve status (CLOSED/OPEN)**
Zero-flow pre-heating	OFF	ON	OFF	CLOSED
Flow pre-heating	OFF	ON	ON	OPEN
Post-heating	ON	ON	OFF	CLOSED
Normal operation	ON	OFF	OFF	CLOSED

Table 1 - EHCS catalyst heating phases, main components (engine, heater, SAP, check valve) activation status.

The development of the EHCS required completing several activities using dedicated methodologies (Figure 8 shows the complete development process).

The initial activity focused on determining the placement of the heater in relation to the TWCs (Par. 3.1.1). This task was carried out using 1D CFD simulation tools (Par. 2.1.1).

Subsequently, an assessment of the heating process, analyzing the heat exchange between the heater, TWCs, and the surroundings (Par. 3.1.2), was conducted using 3D CFD tools (Par. 2.1.2).

Then, EHCS heating strategy was optimized through 1D CFD simulations (Par. 2.1.1) in order to find, for a given electrical power, the best combination of preheating and postheating durations, and airflow rate (Par. 3.1.3).

After the completion of the simulation work, a heater prototype, provided by a supplier, was tested. The heating transient and the temperature distribution within the heater were experimentally characterized (Par. 3.1.4) connecting the standalone heater prototype to a battery emulator (Par. 2.1.3).

Eventually, the optimized hardware and heating strategies were tested (Par. 3.1.5) on an engine test bench using a complete system comprising the engine, ATS, and EHCS installed within a climatic test cell (Par. 2.1.4).

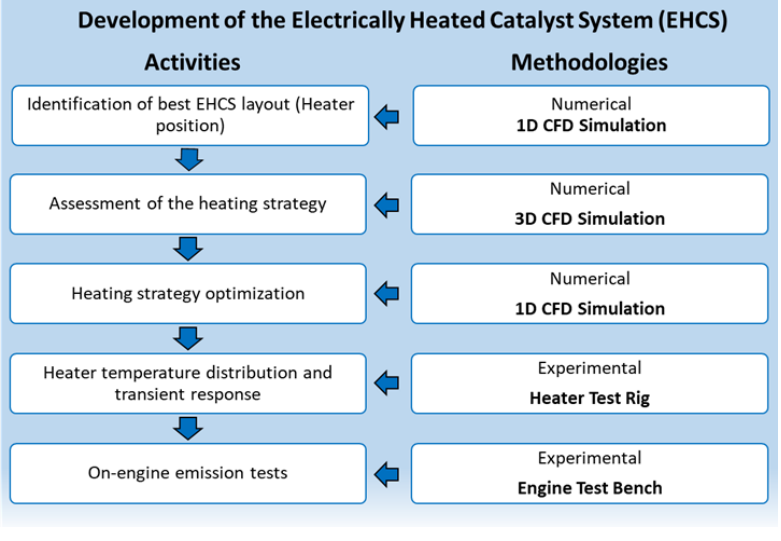

Figure 8 - Development of the Electrically Heated Catalyst System (EHCS): activities conducted, and methodologies employed.

1.4.2 Fuel Burner System (FBS) description

A schematic view of the FBS is displayed in Figure 9. The main component of the FBS is the burner, consisting of a combustion chamber with an integrated air-fuel mixing system, a fuel injector, and an igniter. The burner is powered by low-pressure gasoline (5-7 bar) from the vehicle fuel tank and filtered air from the engine compartment, delivered through a dedicated air path. A SAP supplies the required airflow, measured by a flow meter, and a check-valve located between the SAP and the combustion chamber prevents backflow when the burner is off. The ATS is identical to the EHCS case.

The burner is connected to the exhaust line, upstream of either TWC1 or TWC2 (POS1 or POS2 in Figure 9.a/b) to ensure rapid light-off. Since fuel pressure is assumed to be constant, fuel flow can be regulated by varying the pulse width of the fuel injector opening.

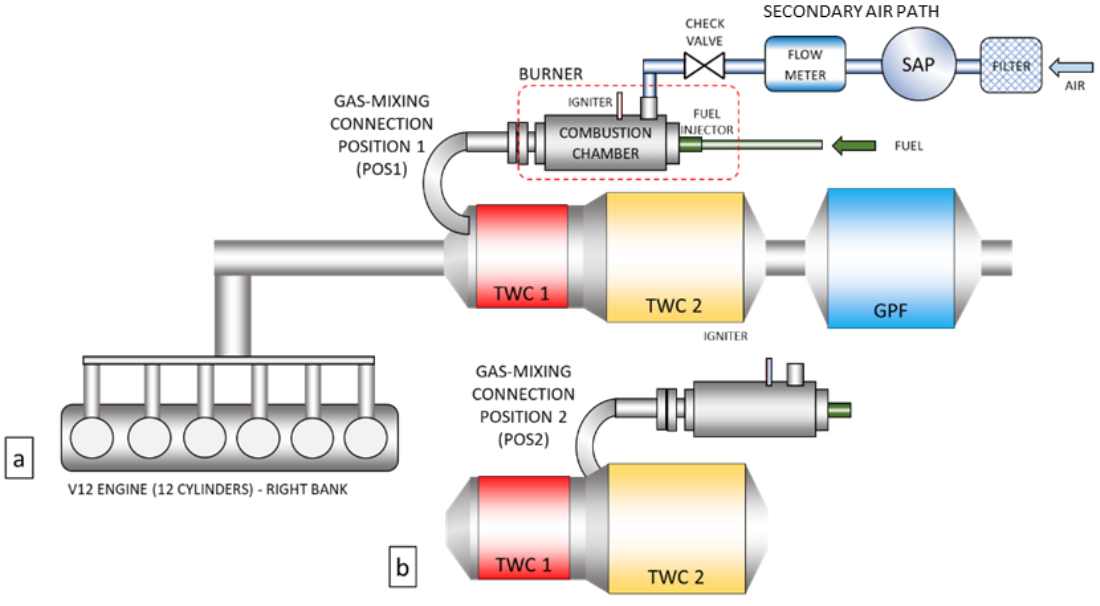

Figure 9 - Schematic view of the Fuel Burner System (FBS) with two possible layouts: a) Burner connected upstream of TWC1 (POS1), b) Burner connected upstream of TWC2 (POS2).

The thermal power, generated by burning fuel in the burner combustion chamber, can reach up to 16kW. The gas temperature at the burner outlet is above 1200°C (Figure 10). This heating power is supplied to the TWC through a specially designed connection to the exhaust line called gas-mixing connection. The burner operates independently of the ICE and can be activated before the engine start (preheating). With adequate preheating, light-off (at least for TWC1) can be achieved even before the engine start.

The catalyst heating strategy consists of up to three phases (Figure 10 and Table 2):

1. SAP ramp-up - engine off, burner off, airflow ramping-up, and check valve open.
2. preheating - engine off, burner on, airflow on, and check valve open.
3. postheating - engine on, burner on, airflow on, and check valve open (not present in Figure 10).

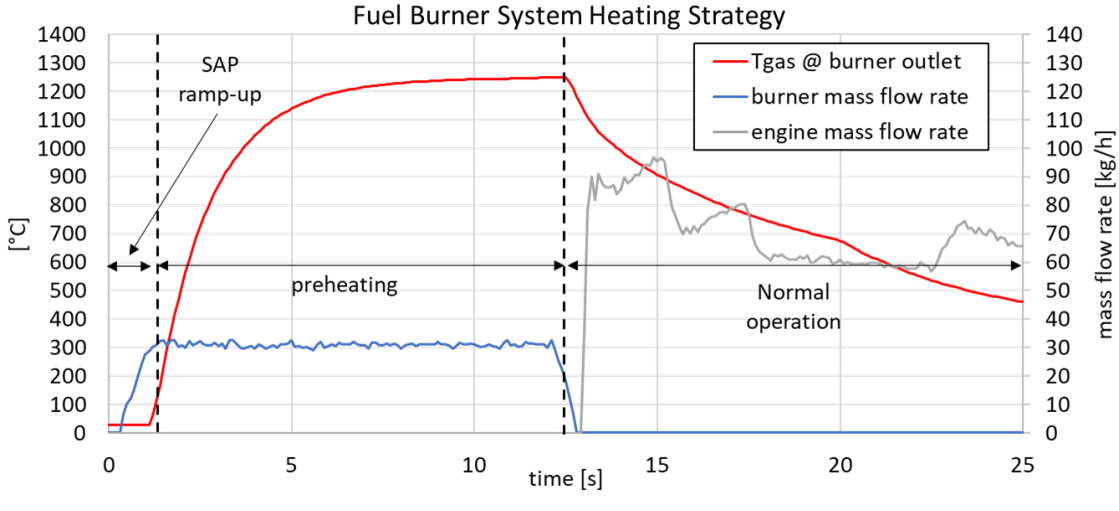

Figure 10 - Fuel burner system (FBS) heating strategy example: 12s of preheating. Gas temperature at burner outlet (red line), burner exhaust gas flow rate (blue line), engine exhaust gas flow rate (grey line).

Strategy Description				
Phase	**Engine status (ON/OFF)**	**Burner status (ON/OFF)**	**SAP status (ON/OFF)**	**Check Valve status (CLOSED/OPEN)**
SAP ramp-up	OFF	OFF	ON	OPEN
Pre-heating	OFF	ON	ON	OPEN
Post-heating	ON	ON	ON	OPEN
Normal operation	ON	OFF	OFF	CLOSED

Table 2 - Fuel burner system (FBS) catalyst heating phases, main components (engine, burner, SAP, check valve) activation status.

Figure 11 shows a CAD model of a burner analyzed with 3D CFD simulations to evaluate key characteristics necessary for its proper operation. The operation of the burner involves several interconnected processes. Initially, air is drawn into the burner through the secondary air inlet and mixed with fuel injected by an automotive-derived fuel injector by means of a swirler. The swirler introduces controlled turbulence into the air-fuel stream entering the combustion chamber.

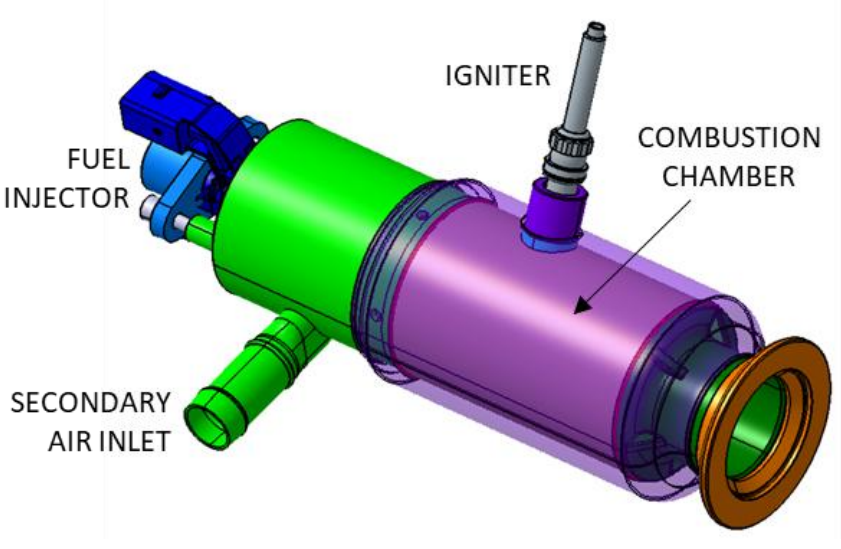

Figure 11 - Burner preliminary design: CAD model of the outer shape.

This swirling motion increases the interaction between air and fuel droplets, leading to a more uniform mixture. Indeed, the swirler creates a central recirculation zone of toroidal shape inside the combustion chamber (Figure 12.a) that supports fuel atomization, increases turbulence, and, once combustion is initiated, promotes flame stabilization by compacting the reaction zone.

To achieve a repeatable startup of the burner, it is necessary to obtain an ignitable mixture near the igniter zone with a composition as close as possible to stoichiometry, thereby minimizing the risk of high unburned HC emissions due to excessive delay in the air-fuel mixture ignition (Figure 12.b). In order to avoid peaks of unburned HC, it is also necessary to minimize, as much as possible, the quantity of liquid fuel on the walls of the combustion chamber at the start of combustion (Figure 12.c).

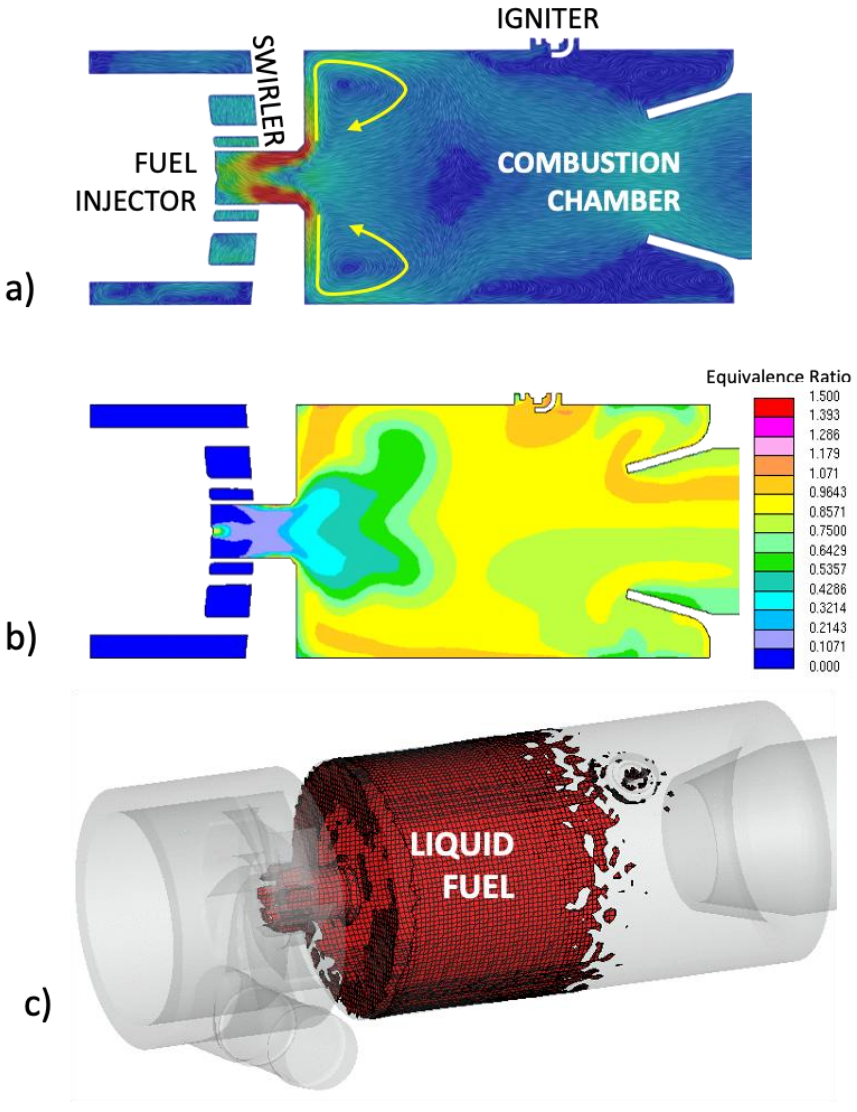

Figure 12 - 3D CFD analysis of the burner combustion chamber: a) flow field, b) equivalence ratio distribution, c) liquid fuel wall wetting.

Similarly to the EHCS, the development of the FBS necessitated the completion of several activities using dedicated methodologies (Figure 13 shows the complete development process).

It was first necessary to experimentally characterize the behavior of the burner to achieve stable combustion with reduced pollutant emissions (Par. 3.2.1). Experimental tests were conducted by connecting the burner to an exhaust line without after-treatment to prevent potential damage of the TWCs (Par. 2.2.1). For this and subsequent experimental activities, a burner prototype manufactured by Robert Bosch GmbH was used.

Subsequently, by means of 1D CFD simulation (Par. 2.2.2), it was possible to identify the best layout among the two initially defined, POS1 and POS2 (Par. 3.2.2).

After the burner position definition, the geometry of the gas-mixing connection was optimized (Par. 3.2.3) using 3D CFD simulation tools (Par. 2.2.3.1) to define the best balance between reducing heat losses (maximizing thermal power transferred to the catalytic converter) and ensuring a high degree of temperature and flow uniformity on the catalytic converter inlet surface (to prevent thermal shock-induced damage). The gas-mixing connection performance was also validated experimentally at the engine test bench (Par. 3.2.3).

After finalizing the geometry of the gas-mixing connection, both 1D and 3D CFD simulations (Par. 2.2.2 and Par.

2.2.3.2) were employed to optimize the FBS heating strategy for reducing exhaust emissions (Par. 3.2.4).

Then, the finalized hardware and optimized strategies were tested (Par. 3.2.5) on an engine test bench using a complete system comprising the engine, ATS, and FBS installed within a climatic test cell (Par. 2.2.4).

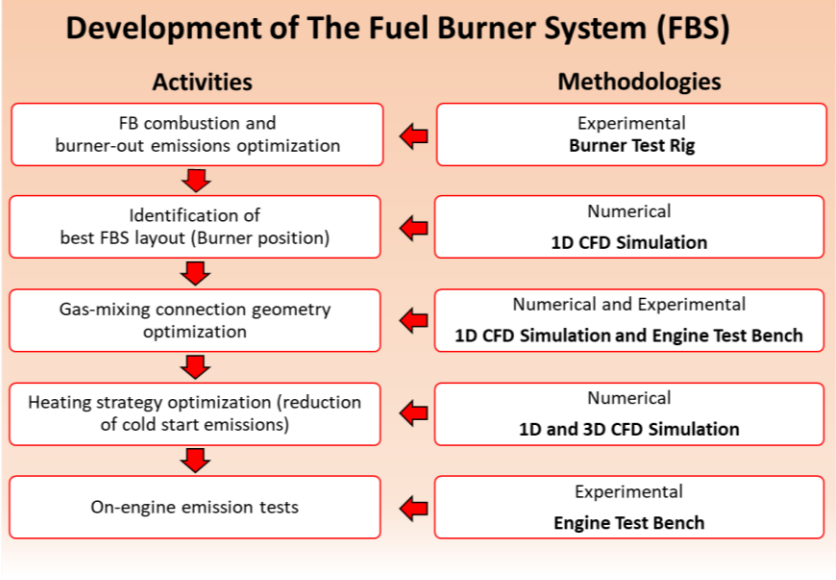

Figure 13 - Development of the Fuel Burner System (FBS): activities conducted, and methodologies employed.

2 Methods

2.1 Electrically Heated Catalyst System (EHCS)

2.1.1 1D CFD Simulation

The identification of the best EHCS layout and a preliminary heating strategy optimization was performed by means of 1D CFD simulations. The modeling was performed with GT-Power V2018; a commercial tool licensed by Gamma Technologies. This tool employs a quasi-steady state approach to simulate the exhaust line. Special attention was paid to the modeling of the heater and TWCs characteristics (e.g., substrate geometry and material, insulating material, washcoat and PGM loadings).

The heater was modelled as a metallic monolithic honeycomb with a cell density of 400 cpsi. The heating power was uniformly distributed throughout the entire heater volume; three-dimensional effects due to the geometry of the heater electric resistance were not considered. TWC1 and TWC2 were modeled as honeycomb ceramic substrates with respective cell densities of 800 and 900 cpsi.

A visual representation of the 1D CFD models is shown in Figure 14 for the two possible EHCS layouts (POS1 and POS2). The simulation focused solely on gaseous emissions, excluding particulate matter. For this reason, the GPF was not included in the model.

A previously developed kinetic scheme of the TWC (based on the Ramanathan & Sharma work, [50]) was integrated in the model. This model replicates the chemical properties of the TWC, its washcoat composition, and its aging status using Arrhenius reaction kinetics, as described in Eq. 1:

(1) $Rate = k[A]^a[B]^b$

Where A and B are reactants, 'a' and 'b' are their respective stoichiometric coefficients, and 'k' is a constant, as defined in Eq. 2:

(2) $k = Fe^{\frac{-E_{act}}{RT}}$

Where F is the frequency factor (also known as the pre-exponential multiplier), E_{act} represents the activation energy in units of joules per mole (J/mol), R is the universal gas constant in units of J/mol/K, and T denotes the temperature in kelvin (K). The term E_{act}/R is also known as the activation temperature, expressed in kelvin.

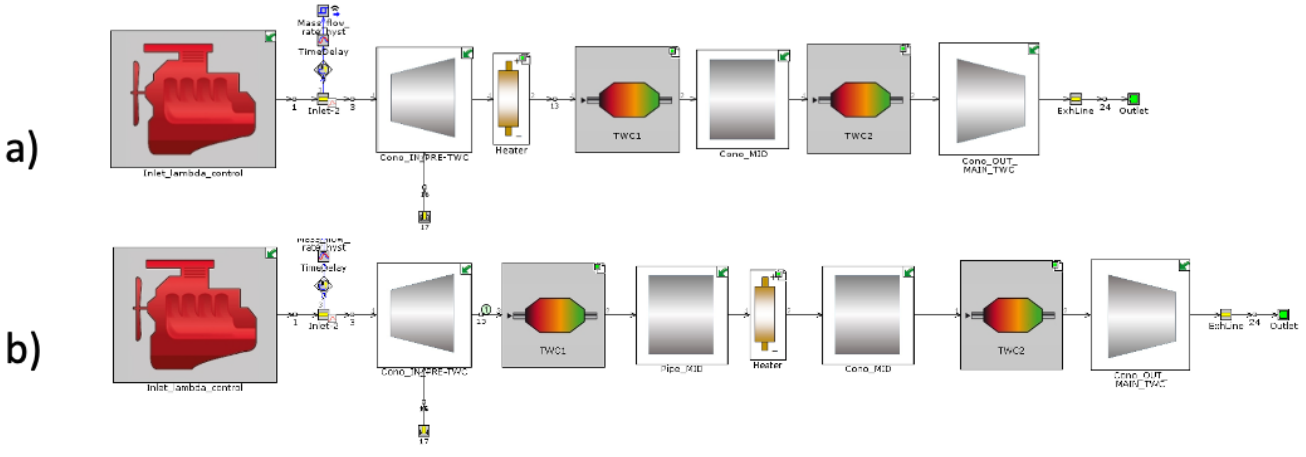

Figure 14 - GT-Power model of the EHCS: a) heater upstream TWC1 (POS1), b) heater between TWC1 and TWC2 (POS2).

The implemented kinetic scheme also included oxygen storage reactions to reproduce the oxygen storage capacity (OSC) of the TWCs, differentiating between slower cerium reactions occurring at higher temperatures, and fast-cerium reactions, which are quicker and occur at lower temperatures. For further details about the OSC model and how to calibrate it, refer to Della Torre et al. [57].

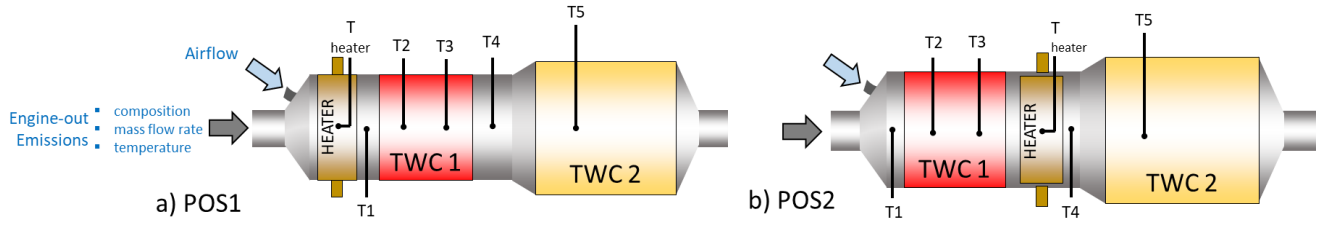

Figure 15 - Simulation input data, schematic representation of the virtual temperature sensors, two layouts considered: (a) heater upstream TWC1 (POS1), (b) heater between TWC1 and TWC2 (POS2).

Simulation inputs (blue labels in Figure 15) were obtained by conducting (at an ambient temperature of 23°C) an experimental RDE test with a vehicle (refer to Table 3 for engine specifications) equipped with an emission sampling probe positioned before the ATS to measure engine-out emissions. Gaseous emission concentrations were measured using an exhaust gas analyzer (HORIBA MEXA 7170). This analyzer is capable of measuring various pollutant concentrations such as HC, CO, CO2, NOx (NO and NO2). Exhaust gas temperature at the ATS inlet was measured with a type-K thermocouple featuring an external shield of 1.5 mm. The engine exhaust gas flow rate was acquired from the ECU.

The exhaust gas temperatures along the exhaust line and the wall temperatures of TWC1 and TWC2 substrates were estimated by the simulation model. Several virtual temperature sensors were positioned in the exhaust line:

- T_{heater} - heater temperature.
- T1 - gas temperature upstream TWC1.
- T2 - TWC1 wall temperature at 1/4 of its axial length.
- T3 - TWC1 wall temperature at 3/4 of its axial length.
- T4 - gas temperature upstream TWC2.
- T5 - TWC2 wall temperature at 1/4 of its axial length.

These temperatures, along with the estimated tailpipe emissions, allowed to evaluate the EHCS effectiveness to improve the ATS performance.

Engine configuration	V-Engine
Cylinders	12
Displaced volume	6496 cc
Stroke	78 mm
Bore	94 mm
Compression ratio	13.64:1
Power	588kW @8500 rpm

Table 3 - V12 Engine specifications

To evaluate the combined effect of the parameters characterizing the EHCS heating strategy on the reduction of tailpipe emissions, a Design of Experiments (DOE) analysis was conducted using a dedicated tool integrated into GT-Power environment. The chosen parameters (DOE factors) were durations of zero-flow and airflow preheating, airflow rate, and duration of postheating. The DOE factors were varied, assuming the values in Table 4, resulting in a total of 270 combinations. For each combination of factors, a simulation was conducted. The simulation covered the initial 50 seconds after engine startup of the RDE test previously described.

Zero-flow pre-heating duration	s	0	5	10	15	20	25
Pre-heating with flow duration	s	0	7.5	15	22.5	30	
post-heating duration	s	0	10	20			
Secondary air mass flow rate	kg/h	10	30	45			

Table 4 - DOE factors and corresponding values.

To assess the performance of the EHCS at temperatures below zero - a condition already considered by current emission regulations - another DOE analysis was conducted. This analysis replaced the previous RDE test input data with RDE data obtained at an ambient temperature of -7°C. Under these conditions, engine-out emissions significantly increase. Typically, HC and CO emissions rise due to reduced combustion efficiency and poor homogenization of the air-fuel mixture in the combustion chamber (Figure 16).

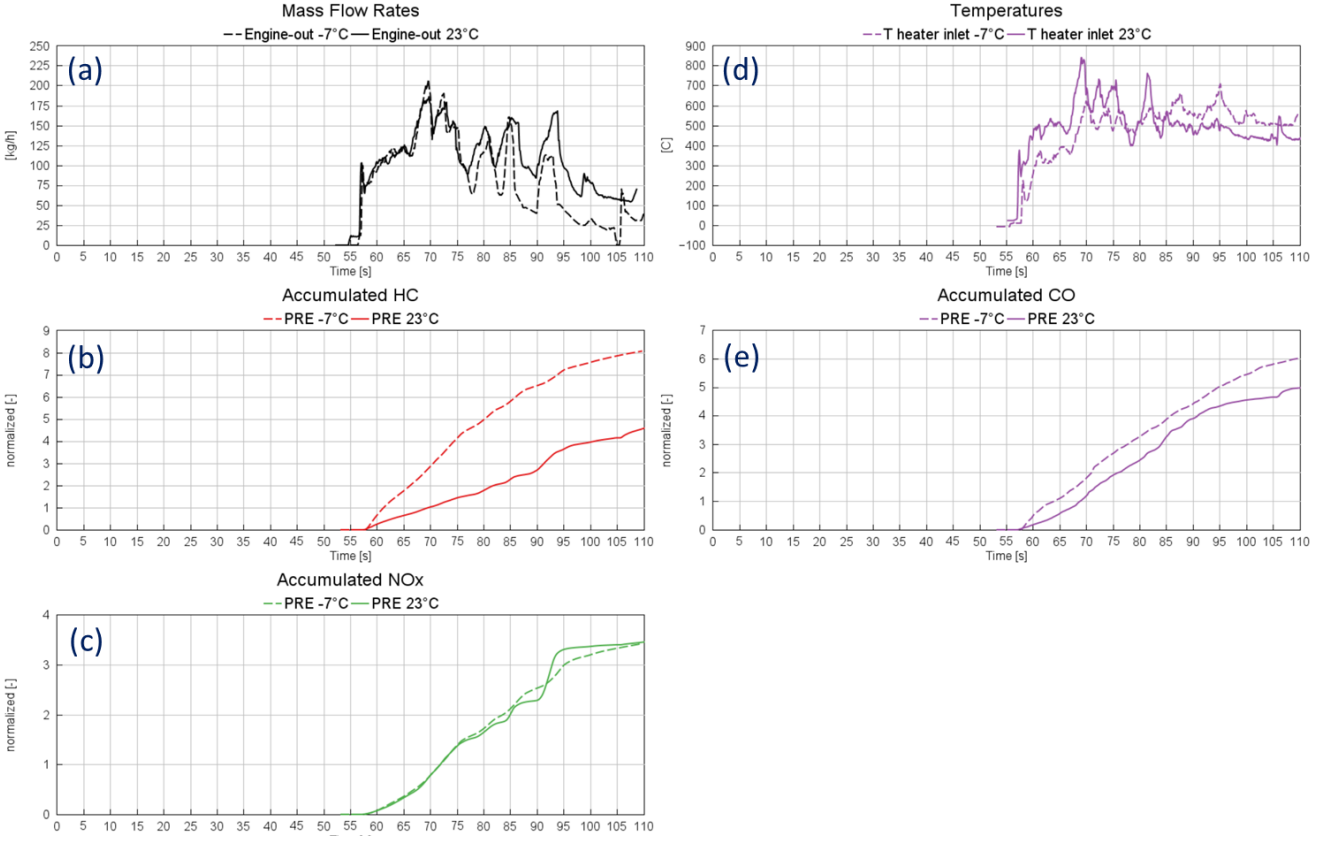

Figure 16 – RDE test input data obtained at ambient temperatures of -7°C (dashed lines) and 23°C (solid lines). (a) Engine mass flow rates, (d) after-treatment inlet temperatures (T_{heater_inlet}), (b, c, e) normalized engine-out accumulated HC, CO, NOx emissions. Normalization was performed with respect to the accumulated tailpipe emissions of the configuration tested at an ambient temperature of 23°C with the heater disabled (passive heating).

2.1.2 3D CFD Simulation

The heater geometry could lead to the presence of local hot spots, thereby limiting the achievable average temperature of the component. In fact, the operation of the heater depends on the maximum allowable temperature of its base material; thus, local hot spots could influence the heating strategy being considered. The radiative heat transfer from the heater to its surroundings is expected to be significant throughout the entire thermal transient of the exhaust line.

A comprehensive 3D CFD model provided a reliable description of the heater thermal transient, thanks to the implementation of the Joule effect and a dedicated radiative heat transfer methodology. The modeling was

based on the Conjugate Heat Transfer (CHT) multi-region approach developed in the open-source CFD code OpenFOAM.

The CHT multi-region approach is a computational method used to simulate the heat transfer that occurs between solid and fluid regions with differing thermal properties. The CFD code, developed by Della Torre et al. [44-47], includes specific libraries for the handling of the interaction between exhaust gas and after-treatment devices.

Figure 17 depicts the modeled exhaust line equipped with a heater. The fluid domain describes the exhaust gas flow through the line, the substrate domain describes the catalyzed porous medium, the EHC domain refers to the heater (modeled as a porous substrate), and the solid domain represents the solid walls of the metal pipes and canning.

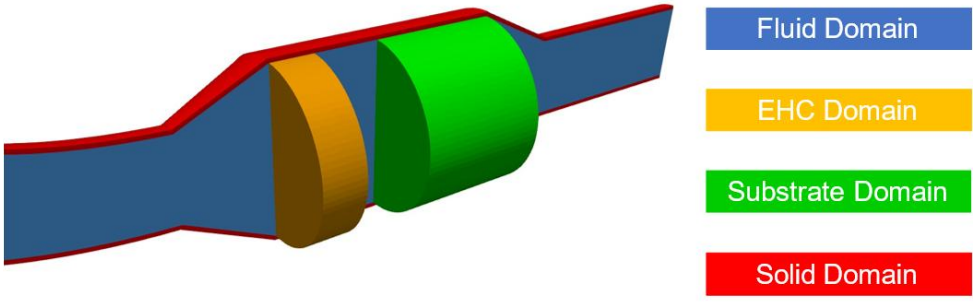

Figure 17 - After-treatment system equipped with a heater: multi-region framework.

The computational meshes can be either adjacent or overlapping: the former typically applies to the solid metallic walls bounding the fluid domain, while the latter is necessary for describing porous substrates, where the fluid and solid phases coexist in the same zone. This multi-region framework enables accurate depiction of the thermal transient of the system during engine cold start and its effect on the light-off of the catalytic reactions.

The multi-region problem involves solving different governing equations for each domain and establishing coupling models to describe their interactions, as illustrated in Figure 18. For the fluid domain, the model includes conservation equations for chemical species, momentum, and energy. Source terms include $S_{Yi,g}$ for gas-phase homogeneous reaction rates, $\mathcal{R}_g$ for flow resistance due to the permeability of the porous domain, and $S_{E,g}$ for heat effects from chemical reactions. In EHC, substrate, and solid domains, energy conservation equations determine temperatures, incorporating $S_{E,s}$ for external heating effects, such as electrical heating. Additionally, the EHC (in the case of coated heater) and substrate domains solve a balance equation for chemical species on the washcoat surface, with $S_{Yi,w}$ representing catalytic surface reaction rates. A surface reaction model is employed to describe the catalyzed chemical reactions occurring in the washcoat. The competition of the chemical species on the active sites is represented through the Langmuir-Hinshelwood type reaction model [52].

Specific coupling models are required to describe the physical interactions between the regions. These can be based on boundary conditions if the coupling occurs between adjacent regions (fluid to solid, substrate to solid), or on source terms if the coupling is between overlapping regions (fluid to substrate). Source terms are applied to describe the inter-phase heat and mass transfers ($\mathcal{Q}^{w\to g}$, $\mathcal{J}_i^{w\to g}$) occurring in porous substrates (EHC and substrate domains) between the fluid and the washcoat.

As previously mentioned, the CHT multi-region methodology was expanded to include electrical heating modeling (Joule effect). The employed methodology enabled solving the electrical circuit of the EHC domain and achieving the subsequent power distribution. The non-uniformity of heat was intrinsically obtained through the resolution of the heater electrical circuit. The electrical potential equation was incorporated into the characteristic equations of the EHC domain, enabling the calculation of the heating power per unit volume, $\mathcal{Q}_{\text{jH}}$ (Figure 18.b).

The radiation model was also included to account for the radiative heat transfer that occurs at high temperatures between solid and porous components. The radiative heat transfer coupling was achieved through the addition of a radiative source term at the interface between the heater (EHC domain) and the fluid flow (Figure 18.b).

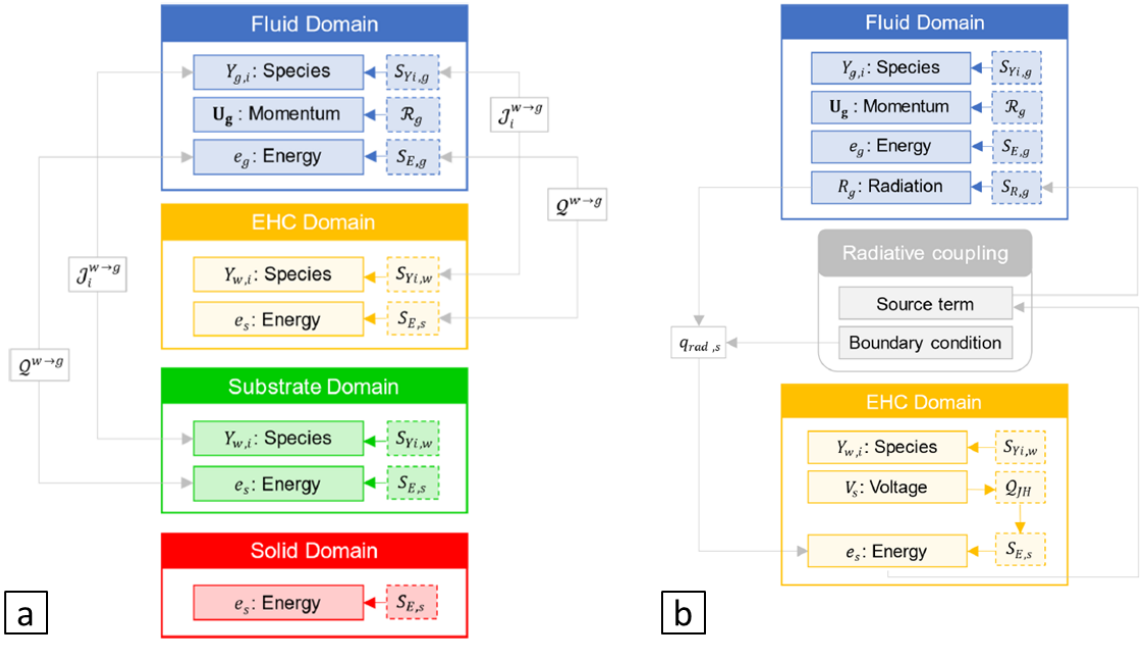

Figure 18 - Conjugate Heat Transfer (CHT) multi-region methodology: a) Overview of the governing equations solved for each domain and of the coupling terms for describing their interaction, b) radiative coupling procedure.

The heater radiative emission was calculated (radiative source term $S_{R,g}$), and its corresponding contribution was incorporated into the fluid domain radiation equation. This approach allowed the emitted radiation to propagate through the fluid domain and contribute to the overall heat transfer [45, 61].

Simulated Conditions	
Electrical Power [kW]	4.0
Phase 1) EHC Active, No Air Flow [s]	20.0
Phase 2) EHC Active, Air Flow [s]	22.0
Phase 3) EHC Not Active, Cold start [s]	30.0
Total Simulated Time [s]	72.0
Air Mass Flow Rate [kg/h]	45.0

a

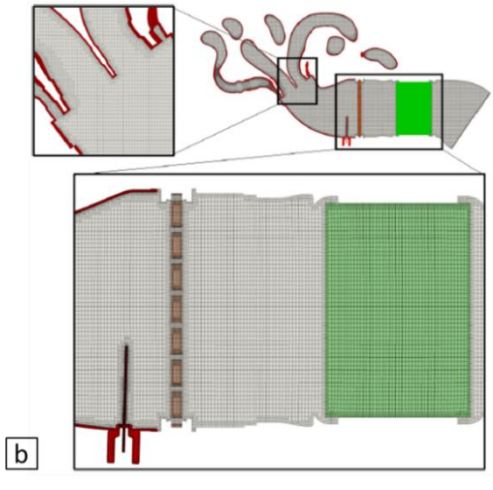

Figure 19 – a) simulated condition b) exhaust line mesh details.

An exhaust line, composed of the exhaust manifold, the heater, and TWC1, was studied to assess the benefits of adopting a heater for engine cold start conditions. The evaluation involved comparing the results of the following strategies:

- heater activated for 44 seconds of preheating (electrical power of 4kW, further details in Figure 19.a).
- heater disabled.

The computational mesh was generated through snappyHexMesh, an automatic mesh generator in the OpenFOAM environment. The obtained grid consisted of mainly hexahedral cells. The standard k - ω SST model was employed to address the description of turbulence. Figure 19.b shows some details of the obtained computational grid.

Simulation inputs, representative of a V12 engine cold start in idling conditions, were imposed at the inlet of the exhaust manifold and to the heater electrodes. These inputs included airflow and exhaust gas flow rates, engine-out temperatures and emissions, and battery voltage.

2.1.3 Heater test rig

The heater prototype was tested powered by a battery emulator (AVL eStorage LV, [53]). The heater was equipped with two thermocouples: the first positioned in the center, the second in a peripheral position (T_{heater_center}, T_{heater_outer} as shown in Figure 20). The goal was to evaluate the temperature transient response and the uniformity of the temperature distribution across the heater. Additionally, the test rig allowed a visual assessment of the temperature distribution (Figure 20.c). The heater prototype was tested by powering it with two levels of electrical power (4.5 kW and 7.5 kW), both with and without the use of secondary airflow. The airflow was supplied by the workshop's compressed air system.

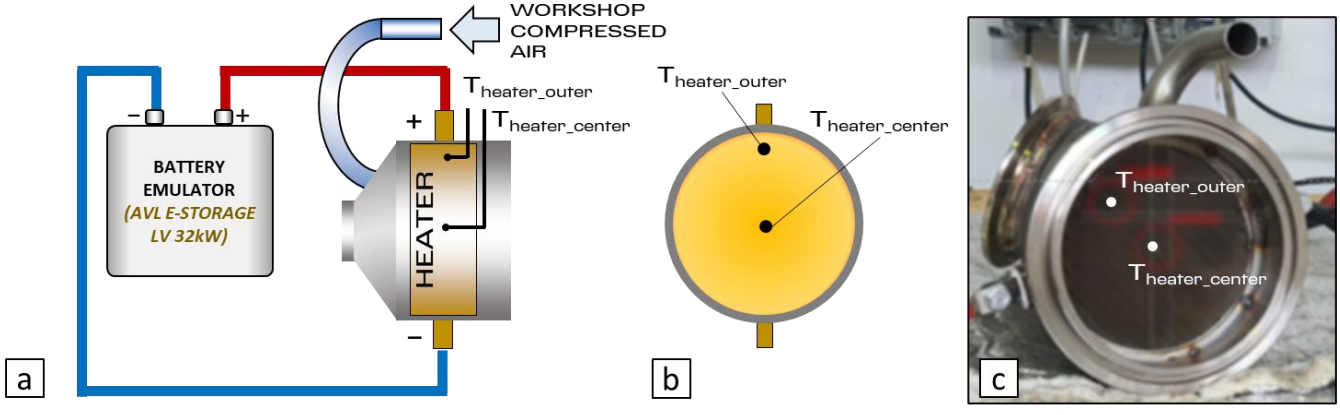

Figure 20 - heater test rig: a) schematic of the test rig, b) thermocouple positions, c) heater outlet view

The battery emulator could deliver a maximum power of 32kW, with a voltage range from 0 to 60V and a current range of 0 to 385 A. The required power output was delivered by adapting the voltage to match the heater electrical resistance, which varied with the temperature.

2.1.4 Engine test bench

The heater prototype was connected to the exhaust manifold and the ATS through flanged connections, as shown in Figure 21.a/b. The use of flanged connections with clamps allowed for easy installation and removal of the heater, enabling the use of different devices (e.g., the burner in replacement of the heater) without the need for welding. The secondary air path was connected to the exhaust line through ducts integrated in the cylinder head near the exhaust manifold flange (Figure 21.c). This type of connection ensured high airflow homogeneity at the heater inlet, thereby limiting the formation of hot spots on the heater. The original secondary air connection on the heater's inlet cone was sealed.

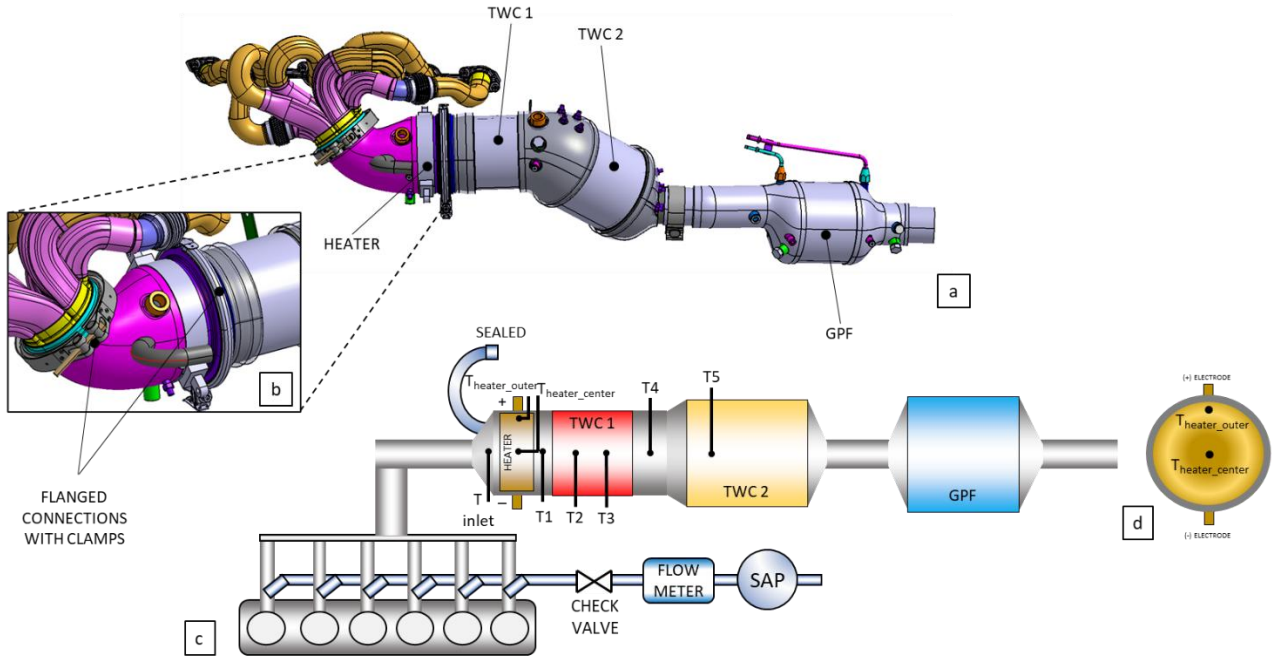

Figure 21 - CAD model of the ATS, Schematics of the EHCS.

Several type-K thermocouples with an external 1.5 mm diameter shield were mounted in the exhaust line (Figure 21.c/d) in the following position:

- T_{inlet} - upstream the heater in center flow position.
- T_{heater_center} and T_{heater_outer} - inside the heater in center and peripheral flow positions, respectively.
- T1 - upstream TWC1 in center flow position.
- T2 - inside TWC1 at 1/4 of its axial length in center flow position.
- T3 - inside TWC1 at 3/4 of its axial length in center flow position.
- T4 - upstream TWC2 in center flow position.
- T5 - inside TWC2 at 1/4 of its axial length in center flow position.

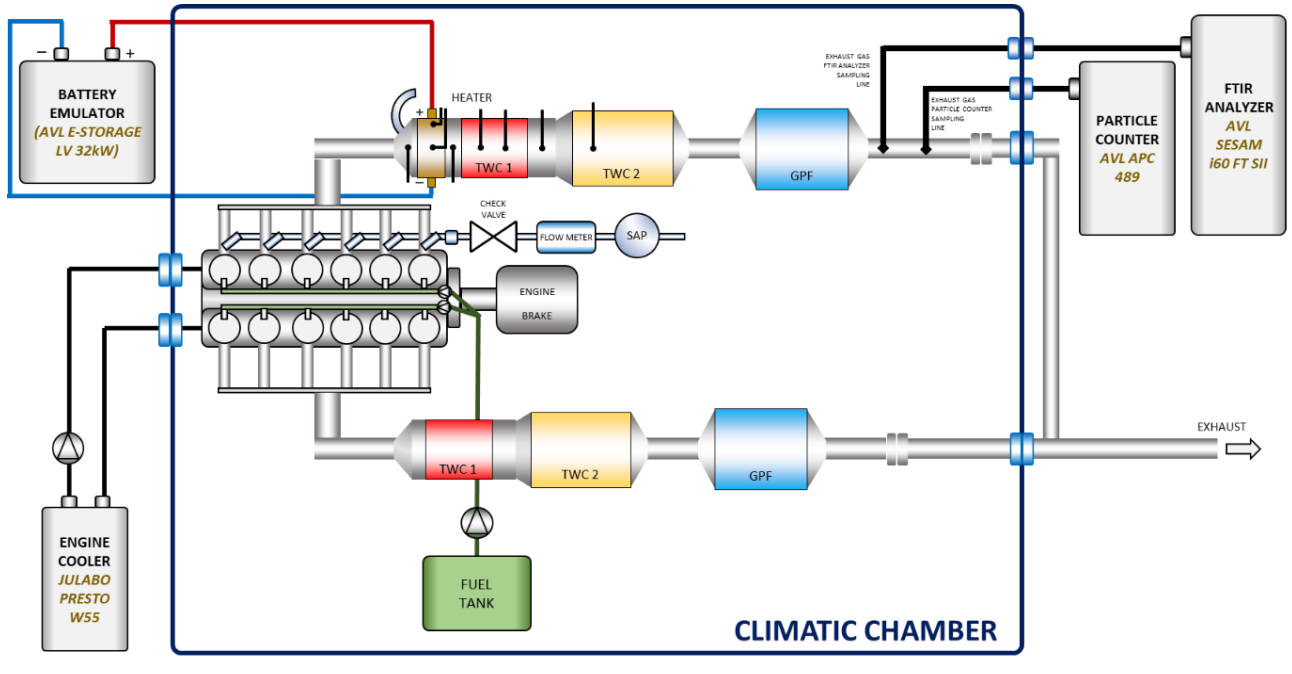

Figure 22 - Schematic of the climatic test cell layout.

The heater was powered by a battery emulator (AVL eStorageLV). Gaseous and solid emissions were measured, respectively, with an FTIR spectrometer (AVL SESAM FTIR, [54] - refer to Par. 2.1.4.1 for more details) and a particle counter (AVL APC Plus [55] – refer to Par. 2.1.4.2 for more details) positioned at the tailpipe. The engine brake, the engine, EHCS, ATS and the fuel tank were placed inside a climatic test cell to reproduce ambient conditions with temperatures even below 0°C. To increase the frequency of tests, the engine was connected to a cooler (JULABO PRESTO W50, [56]), capable of accelerating the cooling of the engine coolant and lubricant. The same ATS without the heater was mounted on the left bank. The entire system is illustrated in Figure 22.

Four test sessions were conducted (parameter variations shown in Table 5):

- Session 1 - The climatic test cell temperature was set to 23°C. Preheating was performed at various heating power levels without airflow (zero-flow) until the heater reached a temperature of approximately 800°C (as recommended by the supplier of the heater prototype). There was no engine startup. The purpose of this test session was to confirm the results of similar tests conducted on the heater test rig using different power levels.
- Session 2 - The climatic test cell temperature was set to 23°C. Zero-flow preheating was performed with various heating power levels until the heater reached a temperature of approximately 800°C. Subsequently, the airflow was activated for 45 seconds while maintaining the heating power at the same level. There was no engine startup. The purpose was to assess the heater's effectiveness in warming up TWC1 and TWC2 through a preheating strategy, with and without the presence of airflow.
- Session 3 - The climatic test cell temperature was set to 23°C. Preheating was performed with various power levels without airflow for 22 seconds. Subsequently, the airflow was activated while maintaining the heating power at the same level for different durations. Then, the engine was started under idle conditions, with the heater remaining active for specific durations. The purpose was to evaluate the effectiveness of the heater in reducing pollutant emissions generated during engine startup at 23°C.
- Session 4 - Partial repetition of session 3, but with the climatic test cell temperature set to -7°C, which represented more challenging conditions in terms of emissions produced by the engine.

On-engine Emission Tests		Test sessions			
		1	2	3	4
		Zero-flow pre-heating	Zero-flow + Heating with flow	Engine cold start	
parameter	unit	Ambient temperature: 20°C	Ambient temperature: 20°C	Ambient temperature: 20°C	Ambient temperature: -7°C
		values	values	values	values
Heating power	kW	2-4-4.3-5.5-6.5-7.5-8.6	4-4.3-5.5-6.5-7.5-8.6	4	4
Zero-flow pre-heating duration	s	required to reach approximately 800°C	required to reach approximately 800°C	22	22
Pre-heating with flow duration	s	n/a	45	0-5-10-20-30	0-30
Post-heating duration	s	n/a	n/a	0-10-15	0-10
Secondary air flow rate	kg/h	n/a	10-15-29-30-40-45	10-30-45	45

Table 5 - On-engine emission tests. EHCS heating strategy parameter variations for each test session.

2.1.4.1 Fourier transform infrared (FTIR) spectrometer

The FTIR Spectrometer can measure several exhaust gas components (Table 6) with a frequency of 5Hz. The total hydrocarbon concentration (THC or HC), usually regulated in emission standards, can be calculated from the measured hydrocarbon species.

Measured Gas Components			
CO - Carbon monoxide	CH_4 - Methane	C_2H_5OH - Ethanol	NC_5 - n-Pentane
CO_2 - Carbon dioxide	C_2H_2 - Acetylene	CH_3OH - Methanol	NC_8 - n-Octane
H_2O - Water	C_2H_4 - Ethene	CH_3CHO - Acetaldehyde	HNCO - Isocyanic acid
NO - Nitrogen monoxide	C_2H_6 - Ethane	HCHO - Formaldehyde	HCN - Hydrogen cyanide
NO_2 - Nitrogen dioxide	C_3H_6 - Propylene	HCOOH - Formic acid	COS - Carbonyl sulfide
N_2O - Nitrous oxide	C_3H_8 - Propane	SO_2 - Sulfur dioxide	AHC - Aromatic HC
NH_3 - Ammonia	C_4H_6 - Butadiene	IC_5 - iso-Pentane	

Table 6 - FTIR spectrometer measured gas components.

The exhaust gas is transferred from the sampling point to the measuring system via a heated sample line (to prevent exhaust gas condensation). Special stainless steel exhaust gas probes are used for the sample extraction; probes are not installed at the bottom of pipelines to prevent the entering of condensate.

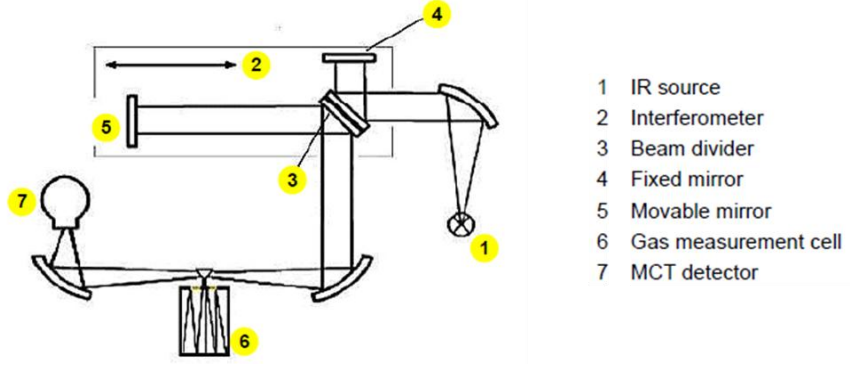

Figure 23 - FTIR spectrometer functional scheme. Source: AVL [54].

The FTIR spectrometer operates on the following principle (Figure 23). A broad spectrum of infrared radiation (in the mid-infrared range between 2.5-25 µm wavelength) is generated using an infrared source and directed into the Michelson interferometer optics through deflection mirrors. A Michelson interferometer is used to split the light into two paths using a beam splitter. One path is reflected from a fixed mirror, while the other is reflected from a movable mirror. When the light paths recombine, they create an interference pattern containing all spectral information with time resolution.

The combined light then passes through the sample to be analysed in the gas measurement cell. Different molecules in the sample absorb specific wavelengths of infrared light, altering the interference pattern. In fact, different functional groups within a molecule have characteristic vibration modes that absorb infrared light at particular wavelengths.

After passing through the sample, the light reaches a highly sensitive MCT (Mercury-Cadmium-Telluride) detector. The MCT detector generates an electrical current proportional to the IR intensity. The electrical signal is then converted into an infrared absorption spectrum through a Fourier Transform process. The resulting spectrum displays various peaks, corresponding to different molecular vibrations. By analysing these peaks, it is possible to identify the chemical composition of the sample.

2.1.4.2 Particle counter (PC)

The AVL APC Plus Particle Counter (PC), in accordance with the ECE R83 legislation, measures the number concentration of all non-volatile particles directly from the raw exhaust sampling (Figure 24 shows a diagram of a PC system). The counting of particles with a condensation particle counter requires a conditioning system, known as the Volatile Particle Remover (VPR), which consists of two dilution stages (providing a high and stable dilution, minimizing particle losses) and an evaporation tube to remove all the volatile particles. Following the volatile removal process, the particle number counter (PNC) measures the number of non-volatile particles. This counter has a specific cut-point diameter of 23 nm, as required by European legislation.

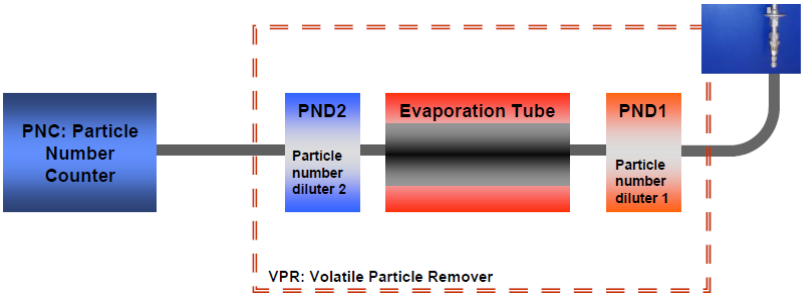

Figure 24 - Particle counter (PC) diagram: gas sampling probe, Volatile Particle remover (VPR) composed of two dilution stages (PND1 and PND2) and an evaporation tube, Particle Number Counter (PNC). Source: AVL [55].

In a PNC, n-butanol serves as the working fluid. The operating principle of the CPC involves enlarging the particles to make them more easily detectable. When the diluted exhaust gas, containing particles, passes through the PNC, these particles act as condensation nuclei for the previously vaporized n-butanol. The particles essentially become butanol droplets with the original particle at their core. These enlarged particles then pass through a laser beam within the PNC, scattering the light. The number of particles is typically proportional to the intensity of the scattered light.

2.2 Fuel Burner System (FBS)

2.2.1 Burner test rig

A burner prototype designed and manufactured by Robert Bosch GmbH was tested on a test rig inside a climatic test cell (Figure 25). The burner utilizes a dedicated injector and igniter to deliver and ignite the necessary amount of fuel for operation; further details about the inner geometry of the air-fuel mixer and combustion chamber cannot be disclosed due to confidentiality reasons.

A schematic view of the test rig is shown in Figure 25. A secondary air pressure sensor, referred to as SAP pressure sensor in Figure 25, was mounted downstream of the SAP to measure the pressure in the secondary air path. A hot film air mass meter was used to measure and control the air mass flow provided by the SAP in a closed-loop control system. A type-K thermocouple with a 0.5 mm external shield diameter was mounted downstream the burner outlet. A pressure sensor and a wideband lambda sensor, referred to as UEGO lambda sensor in Figure 25, were mounted downstream of the burner. Finally, FTIR spectrometer (AVL Sesam i60 FT SII) and PC (AVL APC Plus) sampling lines were positioned at the end of the exhaust line to measure gaseous and solid emissions from the burner.

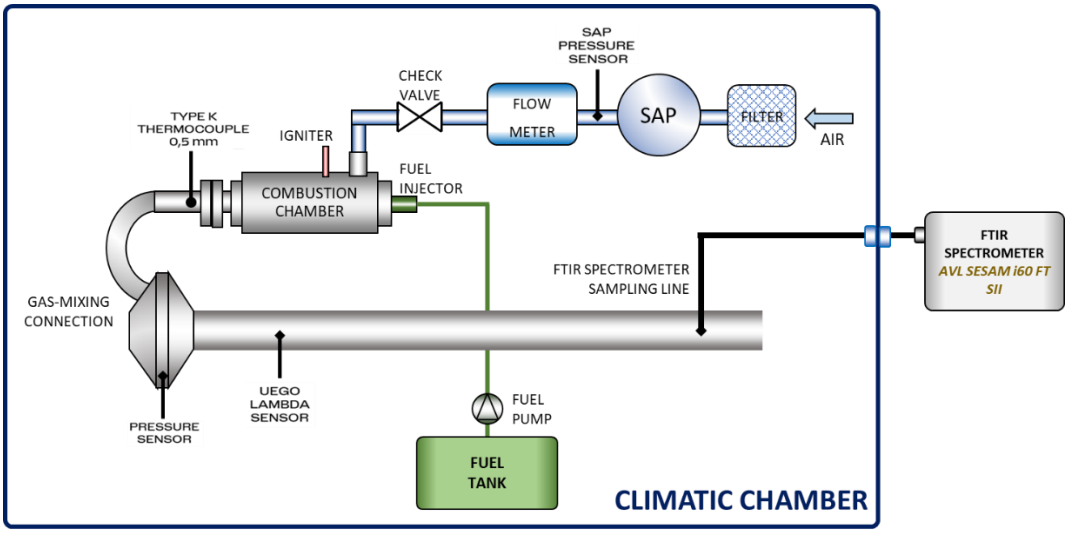

Figure 25 - Schematic view of the burner test rig.

Burner startability tests aimed to calibrate the burner startup in order to minimize startup time (delay between injection release and combustion start) and pollutants generation, while ensuring robust repeatability. The tests were conducted at different ambient temperatures. As an example, Figure 26 shows the representative parameters of the burner operation. In particular, the start of combustion was identified by both the rise of the 0.5 mm thermocouple signal and the peak measured by SAP pressure sensor. Indeed, the pressure wave generated by the start of combustion was identified as the fastest response for the start of combustion, with the rise in temperature, although exhibiting slower dynamics, confirming it.

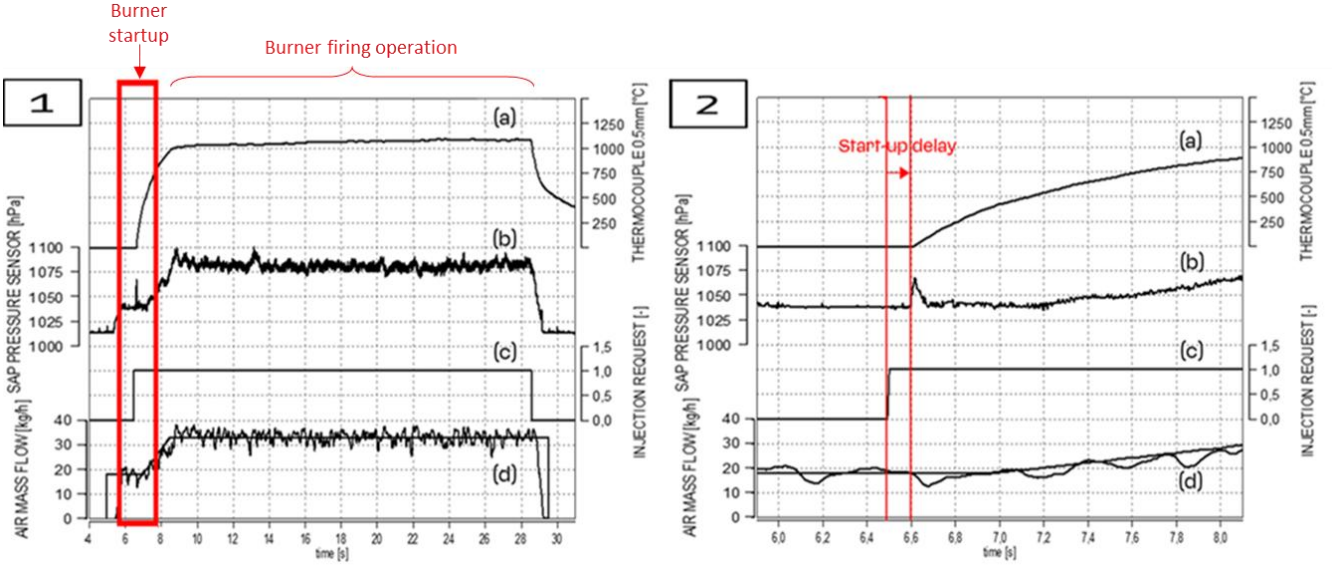

Figure 26 – [1] burner startup and firing test showing in (a) the sensed value of the 0.5 mm thermocouple; in (b) the sensed value of the sensor referred to as SAP pressure sensor in Figure 25; in (c) the bit defining the injection request release; in (d) target and sensed value by the HFM of airflow. [2] Zoom on the startup phase (red box in [1]).

The influence of lambda, as measured by the UEGO lambda sensor, on the startup time and pollutant emissions during burner startup was assessed by conducting a lambda sweep ranging from 0.96 to 1.12. An additional lambda sweep was then performed to optimize burner pollutant emissions and enthalpy flow during firing operation (steady-state operation after the burner startup).

2.2.2 1D CFD Simulation

To define the optimal position for the gas-mixing connection, which minimizes cumulative emissions during an engine cold start, two different configurations were assessed using 1D CFD simulation tools. The modeling was performed with GT-Power V2018. Two different positions for the burner were evaluated, as illustrated in Figure 27: upstream of TWC1 (POS1), and between TWC1 and TWC2 (POS2).

The exhaust line was modeled in a manner similar to the EHCS case, with the burner not included in the model but replaced by input data for the burner (gas-mixing) connection inlet. The experimental activities conducted on the burner test rig provided the following input data: burner-out emissions, exhaust gas temperature and flow rate. Engine-out input data were collected at the engine test bench performing an engine cold start in idling. Along the exhaust line, several virtual temperature sensors were positioned (Figure 28) following the same nomenclature as the EHCS model (Par. 2.1.1). The simulation results are presented in Par. 3.2.2.

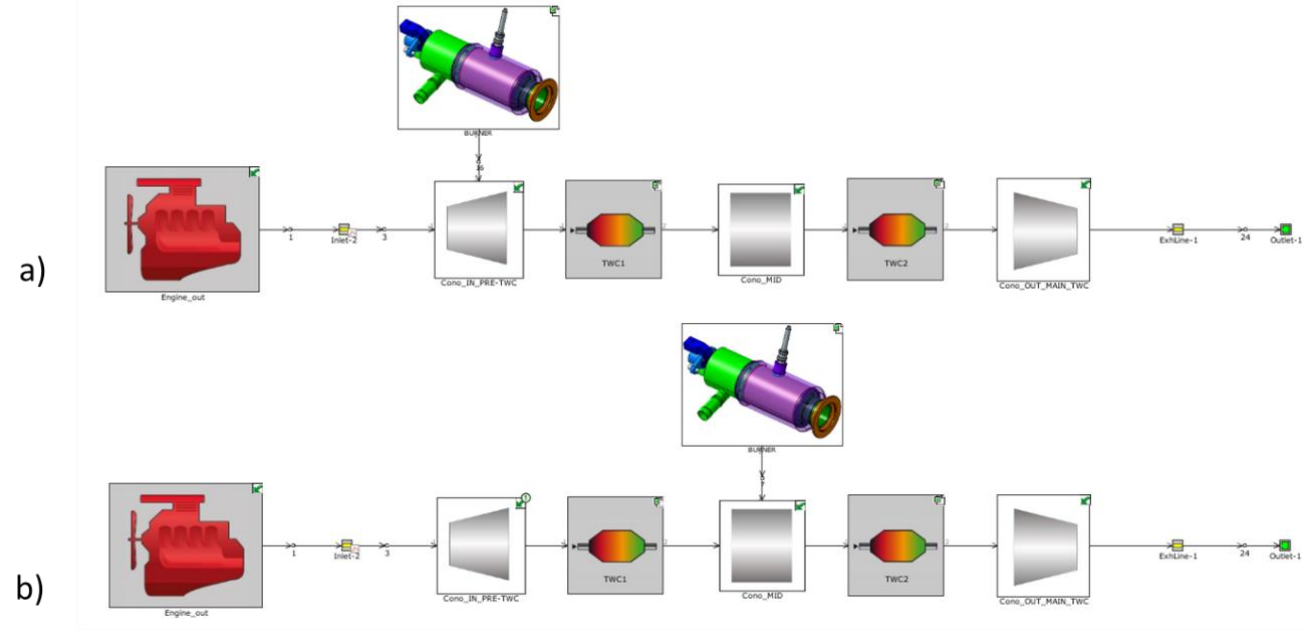

Figure 27 - GT-Power models of the exhaust line including the burner: a) burner connected upstream TWC1 (POS1), b) burner connected between TWC1 and TWC2 (POS2).

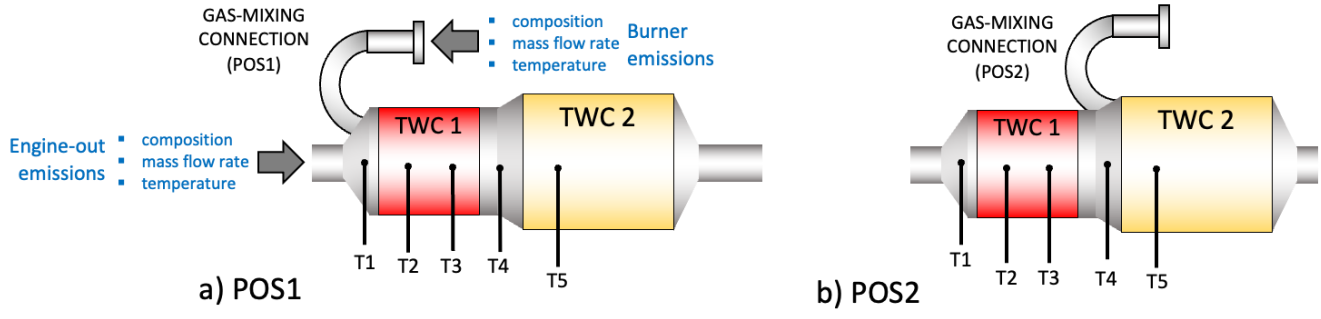

Figure 28 - Schematic representation of the virtual temperature sensor positions for both POS1 and POS2 configurations. The temperature names follow the same nomenclature used for the EHCS model. Simulation input data in blue.

2.2.3 3D CFD Simulation

2.2.3.1 Gas-mixing Connection Design

Connecting the burner to the exhaust line is a crucial aspect of the system performance. Several requirements, such as packaging, reliability, and efficiency, must be met. The space available around the exhaust line is constrained by the vehicle assembly components. Thus, strict limits on the overall dimensions of the gas-mixing connection define the design space. The gas-mixing connection must ensure mechanical resistance to extremely high temperatures. Moreover, it is essential to maintain strict control over the uniformity of temperature and flow velocity on the TWC's front surface to prevent damage to the catalyst during burner operation. Additionally, minimizing heat losses through the gas-mixing connection is essential: this leads to reduced preheating time and emissions. A 3D CFD approach is the most suitable for designing a component that meets these requirements.

The commercial software ANSYS FLUENT, licensed by ANSYS, was utilized. A structured mesh comprising approximately 1 million cells and a high-Reynolds wall treatment was applied. A 2nd order solver on the k-ω SST scheme was used for the calculations. Several loops of 3D CFD simulations were conducted to test various design concepts. The following boundary conditions were applied:

- Burner-out exhaust gas with constant mass flow rate and temperature.

- Steady-state calculation, faster than the CHT approach, yet sufficiently accurate for guiding design exploration (the model described in Par. 2.2.3.2, based on the CHT multi-region approach developed in the OpenFOAM environment, was also at a preliminary stage of development at this phase of the research).
- Wall temperature set to -7°C.
- Preheating only (excluding engine exhaust gas flow).

Temperature uniformity was monitored in all configurations. The uniformity index was defined as follows:

(3) $\gamma = 1 - \frac{\int_S |u-U| \cdot dS}{2U \cdot S}$

Where:
$u = u(x, y)$, velocity magnitude for the coordinate x, y.
U, average velocity on the control section.
S, surface of the control section (in this case the front surface of TWC1).

2.2.3.2 Tailpipe Emission Estimation

The goal of the investigation was to simulate the operation of the FBS during an engine cold start. The model was based on the CHT multi-region approach developed in the OpenFOAM environment. The CFD code, developed by Della Torre et al. [45], was strictly related to the one used in the heater assessment (Par. 2.1.2).

The model was validated using a simplified exhaust line, excluding the exhaust manifold and the TWC, to avoid potential damage to the engine and catalytic converter in case of burner malfunction (the burner was at the beginning of the experimental development), which could lead to extremely high gas temperatures. The validation focused on measuring the gas and wall temperatures at various positions along the exhaust line (Figure 29.a). The model was configured according to a multi-region framework, comprising three distinct domains: one fluid region describing the exhaust gas flow, and two solid regions representing the metallic walls of the exhaust piping and the thermocouples (Figure 29.b). The detailed description of the thermocouples, in terms of their geometrical and thermal properties, enabled accurate reproduction of their thermal inertia and the associated heat transfer phenomena. These phenomena include convection and radiation with the surrounding flow field, and conduction along the thermocouple.

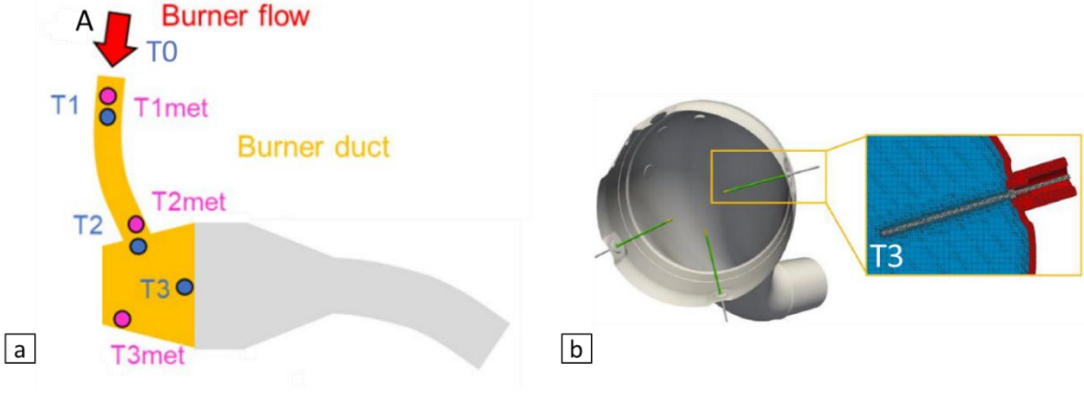

Figure 29 – (a) Schematic of the simplified exhaust line (without exhaust manifold and TWC1) including thermocouple positions (gas temperatures T1, T2, T3 and metallic wall temperatures T1met, T2met, T3met), (b) Detail of the multi-region mesh including thermocouple discretization: fluid domain (blue), metal walls solid domain (red), thermocouple solid domain (gray).

Boundary and initial conditions were imposed on the basis of the experimental measurements used for the model validation. In particular, at the inlet of the burner duct (Figure 29, section A) time varying conditions of mass flow, gas temperature (T0) and chemical composition were imposed. Chemical reactions were not taken

into account at this stage since the catalyst was not included in the configuration. The comparison between calculated and measured temperatures was considered satisfactory (Figure 30).

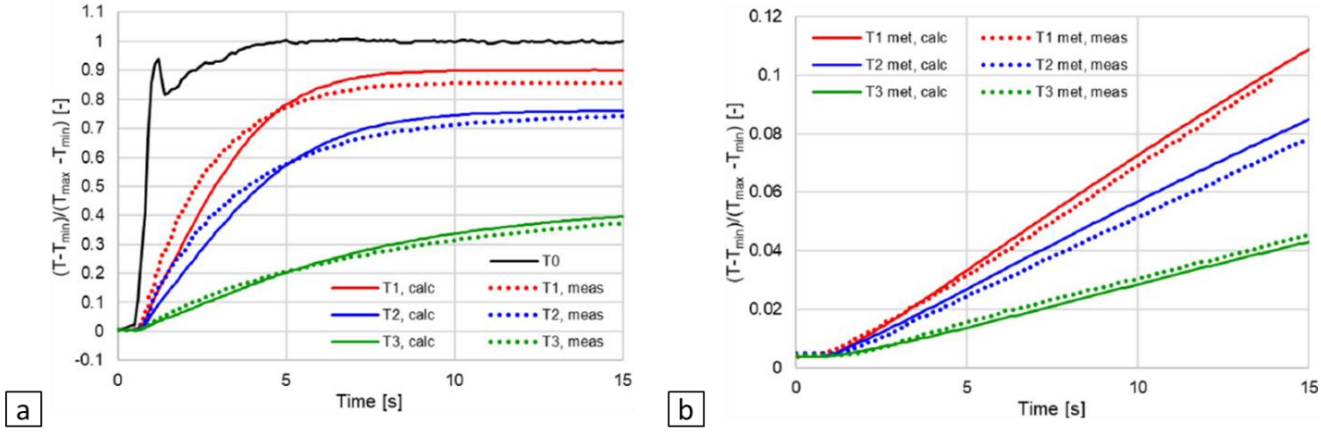

Figure 30 – Comparison between calculated (solid lines) and measured (dotted lines) temperatures at different positions as specified in Figure 29: (a) exhaust gas, (b) metallic walls. Temperatures are normalized with respect to the minimum and maximum T0 values.

After the validation phase the analysis focused on a single bank exhaust system of a V12 engine, including the exhaust manifold, the burner connection, and the TWC1 (Figure 31.a).

The computational grid (Figure 31.b) was generated according to the multi-region framework, including the overlapped substrate region needed for the modeling of the catalyst. The resulting mesh counted $6.6 \cdot 10^6$ cells for the fluid region, $3.1 \cdot 10^6$ for the metal walls and $2.4 \cdot 10^5$ for the substrate (TWC1).

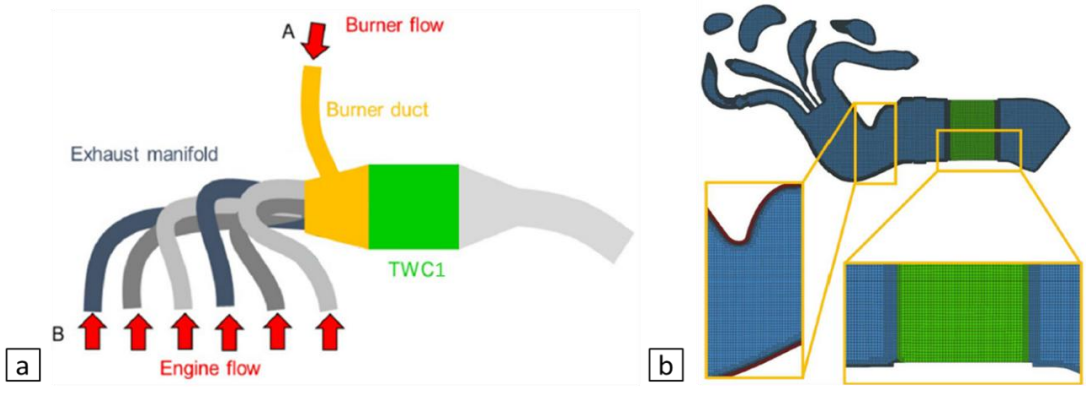

Figure 31 - (a) Schematic of the exhaust system including the burner gas-mixing connection (burner duct), the exhaust manifold, and TWC1, (b) detail of the multi-region mesh including substrate discretization: fluid domain (blue), metal walls solid domain (red), overlapped substrate domain (green).

The Burner was activated for 20 seconds of preheating, followed by engine startup. Experimentally derived mass flow rates, temperatures, and pollutant concentrations were imposed at the inlet of the burner duct (Figure 31.a - section A) and at the manifold (Figure 31.a - section B). For the simulation results, see Par. 3.2.4.

2.2.4 Engine test bench

Similarly to the EHCS experimental configuration, the burner prototype was connected to the exhaust manifold and the ATS through flanged connections with clamps. The use of flanged connections not only enabled the attachment of different devices without the need for welding but also allowed the use of the same ATS as in the EHCS investigations. Adopting the same ATS helped in carrying out a fair comparison between FBS and EHCS, eliminating the potential deviation in the results that could arise from using a different ATS, even one with the same nominal characteristics.

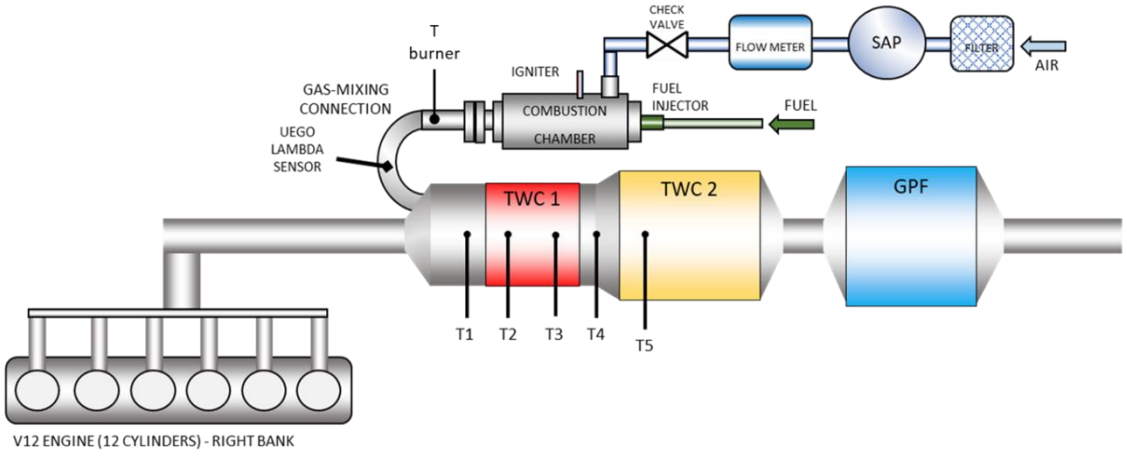

Figure 32 – Schematic view of the Fuel Burner System (FBS) including ATS thermocouple positions.

A schematic view of the experimental apparatus is shown in Figure 32. A dedicated wideband UEGO lambda sensor positioned in the gas-mixing connection downstream the burner was used for the lambda control of the burner. A type-K thermocouple with a 0.5 mm external shield diameter was mounted downstream the burner outlet (T_{burner}). Several type-K thermocouples with an external 1.5mm diameter shield were mounted in the exhaust line in the same positions used in the EHCS layout. The thermocouples followed the same nomenclature (Par. 2.1.4).

Gaseous and solid emissions were measured, respectively, with an FTIR spectrometer (AVL SESAM FTIR) and a particle counter (AVL APC Plus) positioned at the tailpipe. The same climatic test cell used in the EHCS case research was used to reproduce ambient conditions with temperatures below 0°C. The entire system is illustrated in Figure 33. The burner was used for preheating for 20 seconds with optimized calibrations; subsequently, the engine was started and idled in a catalyst-heating strategy for 50 seconds under stoichiometric conditions.

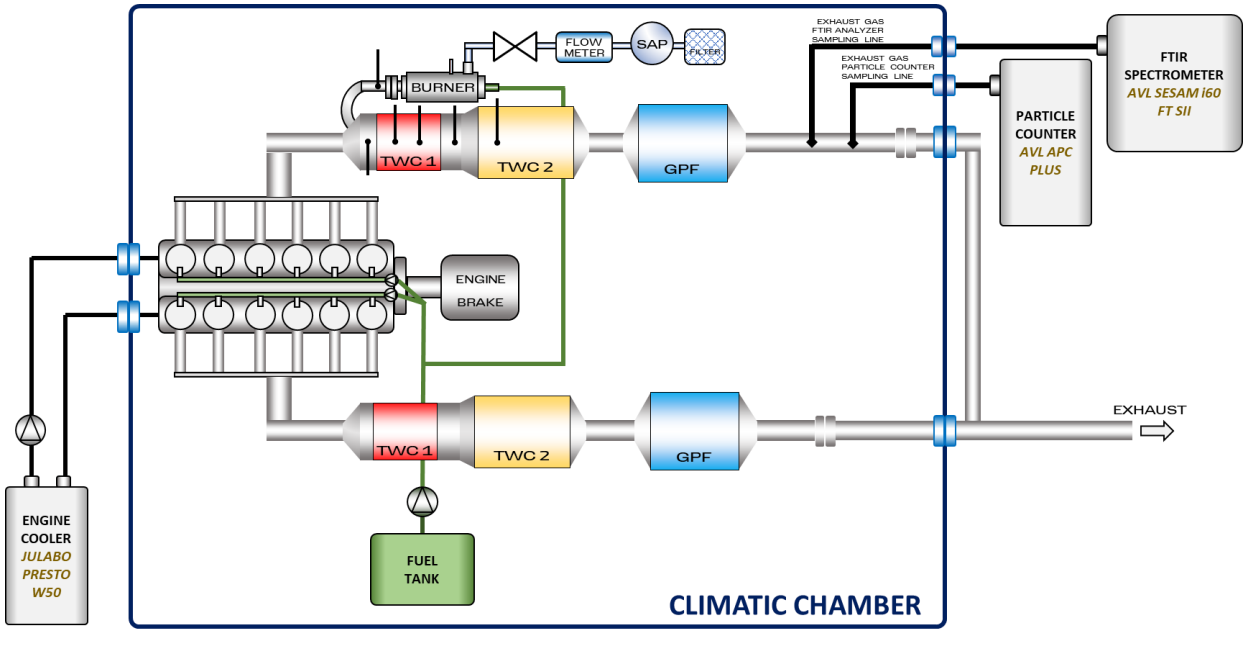

Figure 33 – Fuel Burner System (FBS) on-engine emission tests: schematic view of the experimental apparatus (climatic test cell).

3 Results

3.1 Electrically Heated Catalyst System (EHCS)

3.1.1 Identification of the best layout (heater position)

The initial phase of the EHCS development involved identifying the heater optimal location between POS1 and POS2 layouts (Figure 15). This activity was carried out through calculations utilizing 1D CFD simulation tools, as described in Par. 2.1.1.

Figure 34 shows the results of the comparison between POS1 and POS2 for the following heating strategy conducted at an ambient temperature of 23°C:

- heating power of 4 kW.
- 15 seconds of zero-flow preheating.
- 15 seconds of preheating with an airflow rate of 10 kg/h.
- 20 seconds of postheating.

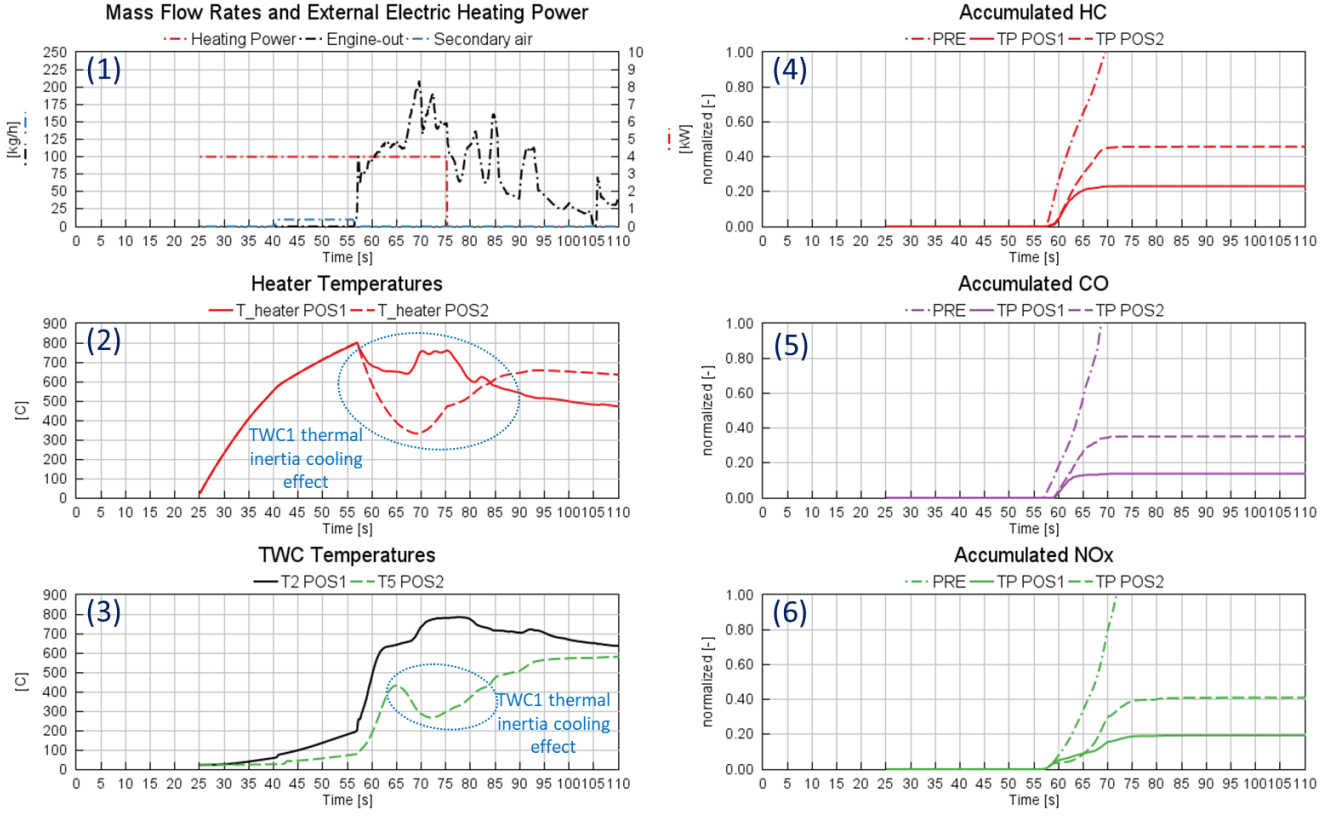

Figure 34 - Comparison between heater POS1 (solid lines) and POS2 (dashed lines) in the exhaust line for a given heating strategy performed at an ambient temperature of 23°C. Engine and secondary air flow rates, heating power, and engine-out emissions (the same for both configurations) are indicated with dash-dot lines. Heating strategy: heating power of 4 kW, 15 seconds of zero-flow preheating,15 seconds of preheating with an airflow rate of 10 kg/h, 20 seconds of postheating. (1) Engine and secondary air flow rates, heating power, (2) heater temperatures, (3) TWC T2 POS1 and T5 POS2 temperatures, (4) accumulated HC emissions, (5) accumulated CO emissions, (6) accumulated NOx emissions. Accumulated emissions are normalized with respect to the passive heating accumulated emissions 50 seconds after engine startup (heater disabled).

The tailpipe cumulative emissions of HC, CO, and NOx (normalized with respect to the passive heating strategy with heater disabled) 50 seconds after engine startup clearly indicate an advantage for POS1 configuration (Figure 34.4/5/6). Comparing T_{heater} in both cases (red solid line for POS1, red dashed line for POS2 as shown in Figure 34.2), from engine startup onwards, a visible cooling of the heater is observed for POS2 layout. Indeed, in POS2 configuration, right after engine startup, exhaust gas is cooled down as it passes through TWC1 before

reaching the heater. The drop in temperature of the heater negatively influences the heating of TWC2, as indicated by the behavior of T5 (green dashed line in Figure 34.3). On the contrary, in POS1 configuration, right after engine startup, exhaust gas, passing through the heater, gains temperature as highlighted by T2 (black solid line in Figure 34.3).

Many other strategies were tested, leading to the same outcome. TWC1 thermal inertia, cooling down the exhaust gas before reaching the heater, negatively affected POS2 layout performance. In conclusion, POS1 configuration was found to be more effective than POS2 in reducing tailpipe emissions. The subsequent development focused on optimizing the heating strategy with heater in POS1.

3.1.2 Assessment of the heating strategy

Once the POS1 configuration was chosen, the preheating strategy described in Figure 19.a, was used to analyze, through a 3D CFD model developed in the OpenFOAM environment (described in Par. 2.1.2), the temperature trends along the exhaust line and the differences in pollutant conversion efficiencies compared to the passive heating strategy. The thermal transient of TWC1 was evaluated through the analysis of TWC1 average temperature at four different cross-sections. The temperature profiles are presented in Figure 35 (normalized with respect to a reference temperature).

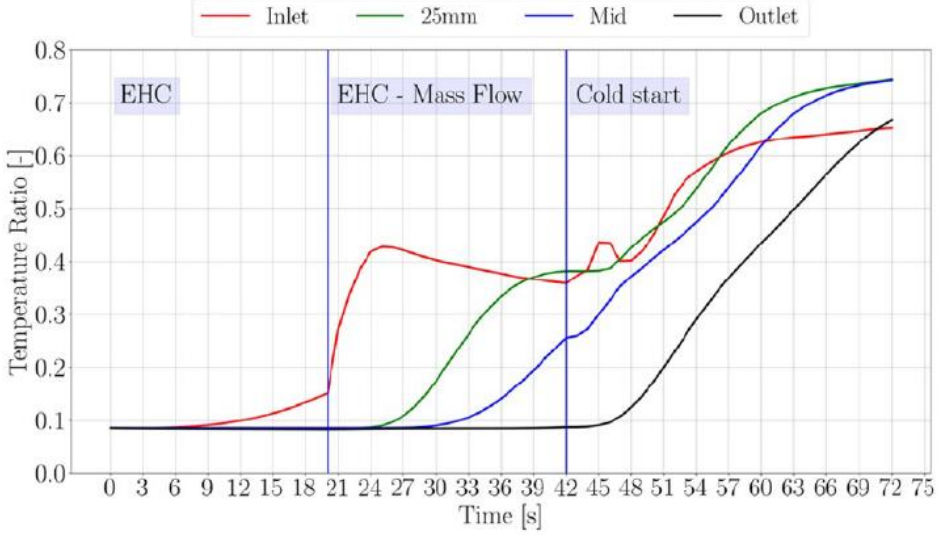

Figure 35 - TWC1 thermal transient, TWC1 average temperature at four different cross-sections: inlet, 25 mm downstream of the inlet, 1/2 of the axial length, outlet.

The implemented radiation model enabled the assessment of the heater's radiative emission and its contribution to heating the front zone of TWC1. In fact, as consequence of radiation, TWC1 inlet temperature rises during zero-flow preheating. Once the airflow is enabled, the subsequent heat transfer from the heater to TWC1 is responsible for a significant increase in TWC1 temperature. At engine startup, more than half of TWC1 is at least partially heated. Also, after engine startup, the energy stored in the heater significantly influences the TWC1 temperature distribution: even though the electrical energy supply is interrupted (no postheating), and despite the engine exhaust gas is still cold due to heat exchange with the exhaust manifold, the temperature of TWC1 continues to rise.

Figure 36 shows a comparison of the TWC1 thermal transient with and without heater activation. The effect of the heater activation is apparent.

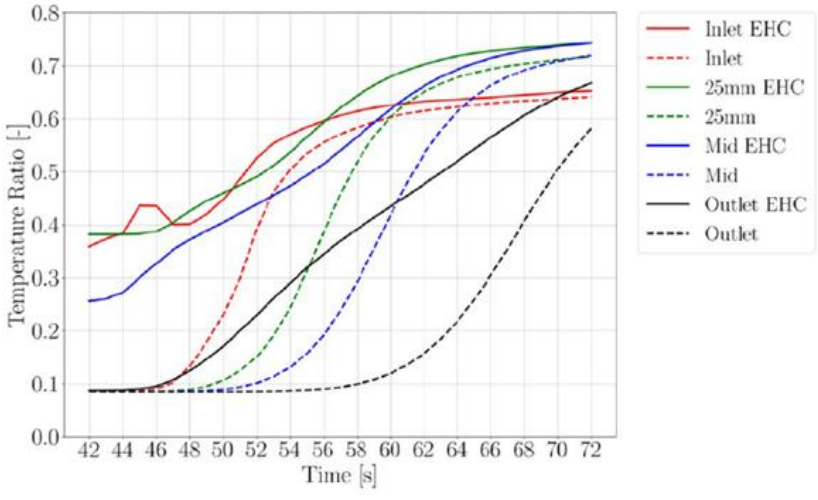

Figure 36 - TWC1 temperature distribution with and without heater activation. Temperatures normalized with respect to a reference temperature

A visualization of the fluid temperature field in the exhaust line is presented in Figure 37. This figure shows the temperature distribution at engine startup (time: 42 seconds) and ten seconds later (time: 52 seconds). As expected, at engine startup with the heater enabled, half of TWC1 is warmed up, whereas with the heater disabled, it remains completely inactive. Ten seconds later, TWC1 remains cold except for a thin front area.

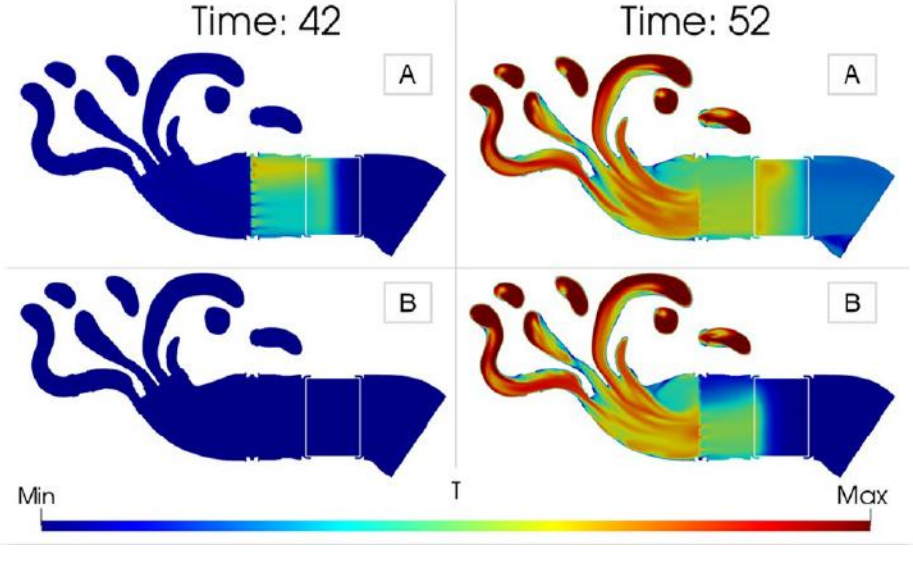

Figure 37 - Fluid temperature distributions with heater enabled (A) and disabled (B). Engine startup (Time:42), 10 seconds after engine startup (Time: 52).

Figure 38 displays the distribution of CO, NO, and HC concentrations along the exhaust line 10 seconds after engine startup for both heating strategies (heater enabled or disabled). In the case where the heater is enabled, TWC1 is well above the light-off temperature, and the conversion of pollutants is very high. When the heater is disabled, an uneven temperature distribution prevents TWC1 from achieving high conversion efficiencies, the upper part of TWC1 is almost completely inactive.

If the heater is enabled, 30 seconds after engine startup, the cumulative emissions of CO and NO are 93% lower compared to the case with passive heating, while HC cumulated emissions show a reduction of 54%.

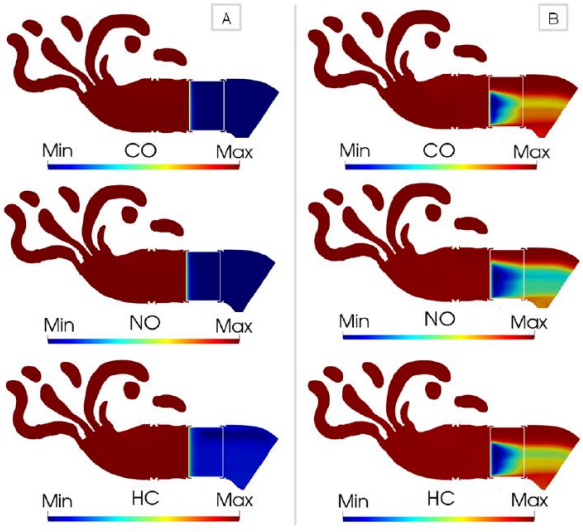

Figure 38 - Pollutant concentration distributions with heater enabled (A) and disabled (B), 10 seconds after engine startup.

3.1.3 Heating strategy optimization

To determine the best EHCS heating strategy, a Design of Experiments (DOE) analysis was conducted, as described in Par. 2.1.1. The DOE factors included the durations of zero-flow and airflow preheating, the airflow rate, and the duration of postheating. The heating power was kept constant at 4kW. The DOE factors were varied, with their values specified in Table 4. The simulation covered the initial 50 seconds after engine startup of an RDE test carried out at an ambient temperature of 23°C in a vehicle equipped with a V12 engine (refer to Table 3 for engine specifications).

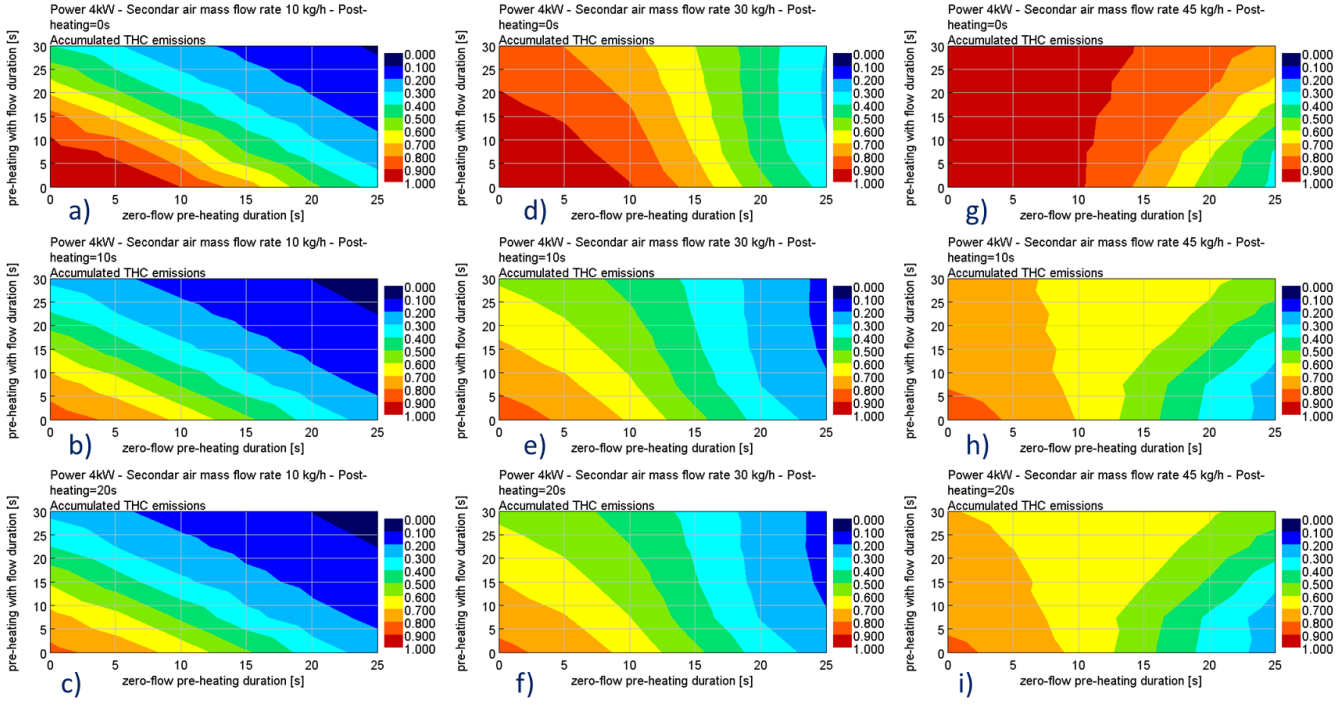

Figure 39 – DOE results at ambient temperature of 23°C: HC cumulative emissions 50 seconds after engine startup for respectively 0, 10, and 20 seconds of postheating, as a function of zero-flow preheating and airflow preheating durations. (a, b, c) airflow rate 10 kg/h, post heating of 0, 10, and 20 seconds, respectively. (d, e, f) airflow rate 30 kg/h, post heating of 0, 10, and 20 seconds, respectively. (g, h, i) airflow rate 45 kg/h, post heating of 0, 10, and 20 seconds, respectively. Accumulated emissions are normalized with respect to the passive heating results 50 seconds after engine startup.

The DOE results for normalized HC tailpipe emissions are summarized in Figure 39. Each graph shows the cumulative HC tailpipe emissions 50 seconds after engine startup, as a function of zero-flow preheating (x-axis) and airflow preheating (y-axis) durations. Plots in the same column show the influence of the postheating duration (0, 10, and 20 seconds, respectively). Plots in the same row show the influence of the airflow (10, 30, and 45 kg/h, respectively).

The CO and NOx tailpipe emissions exhibit the same trends of HC (refer to Figures 87-88 in the Appendix), it is therefore possible to analyze only the HC behavior without compromising the generality of the results. From the outcome of the DOE not only is it possible to identify the best strategy, i.e., the one that minimizes cumulative HC emissions, but also to evaluate the sensitivity of emissions to the variation of the aforementioned DOE factors.

The best strategy is characterized by the maximum duration of preheating (allowed by the DOE constraints) and the lower rate of the airflow (10 kg/h). In summary, the best strategy that complies with the DOE constraints is the following:

- 25 seconds of zero-flow preheating.
- 30 seconds of airflow preheating with an airflow rate of 10 kg/h.
- 20 seconds of postheating.

The results obtained using the best strategy can be compared with the passive heating (Figure 40). The passive heating results are used for the normalization of the tailpipe cumulative emissions. The best strategy enables a remarkable reduction in pollutant emissions: HC by 93%, CO by 95%, and NOx by 92% with respect to passive heating. T2 right after the completion of preheating (engine startup), is 480°C, therefore above the TWC1 light-off temperature (Figure 40.4). The front zone of TWC1 is catalytically active and TWC1 is capable of reducing most of the engine-out emissions.

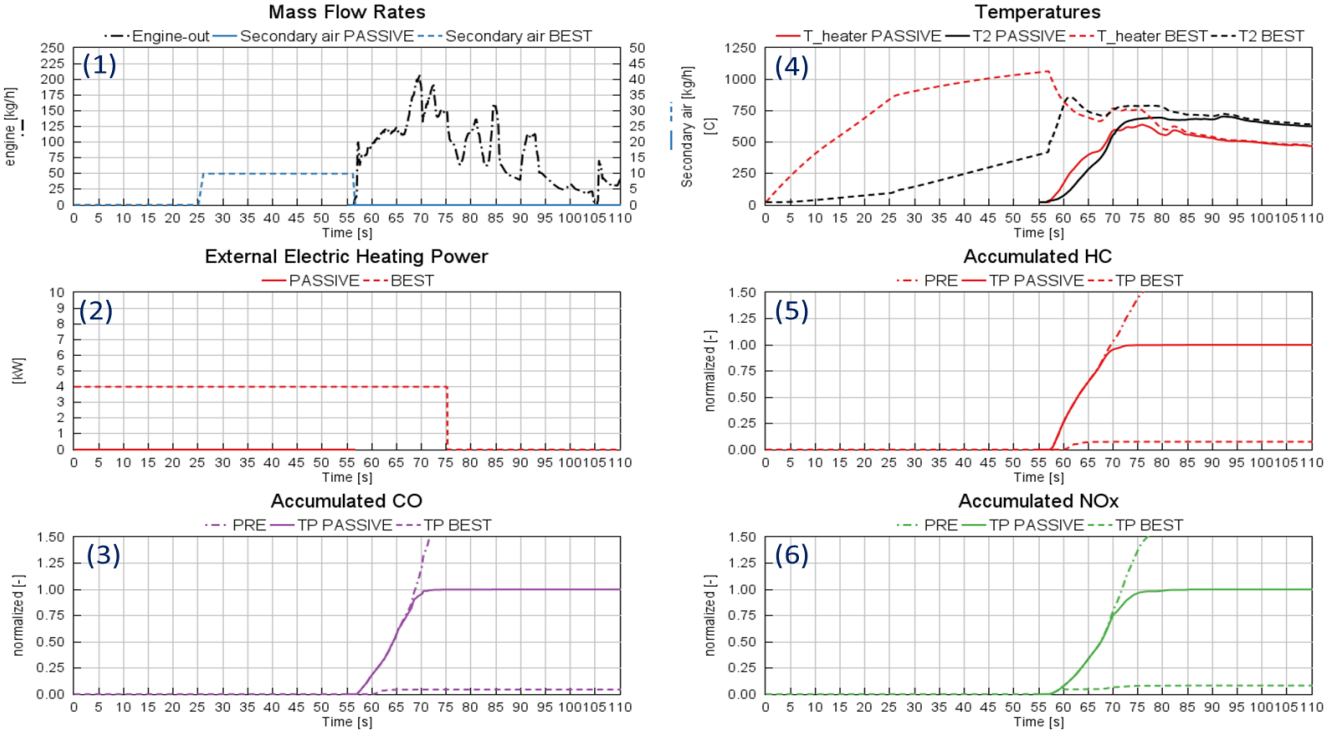

Figure 40 - Comparison between the passive (solid lines) and the best (dashed lines) heating strategies. Engine flow rate and accumulated engine-out emissions (the same for both strategies) are indicated with dash-dot lines. (1) Engine and secondary air flow rates, (2) electrical powers, (3) accumulated engine-out (PRE) and tailpipe (TP) CO emissions, (4) heater and TWC1 T2 temperatures, (5) accumulated engine-out (PRE) and tailpipe (TP) HC emissions, (6) accumulated engine-out (PRE) and tailpipe (TP) NOx emissions. Accumulated emissions are normalized with respect to the passive heating accumulated emissions 50 seconds after engine startup.

Analyzing the DOE results in Figure 39, it is evident that the presence of postheating reduces tailpipe cumulative emissions; however, the effect becomes less noticeable as postheating duration is extended. For instance, Figure 41 shows the comparison between three heating strategies: passive heating, two postheating strategies with durations of respectively 10 and 20 seconds. While 10 seconds of postheating visibly reduce tailpipe cumulative emissions (HC by 13%, CO by 27%, NOx by 15% with respect passive heating), extending it further to 20 seconds has a marginal effect (HC by 16%, CO by 30%, NOx by 21% with respect to passive heating). The comparison of T2 temperatures for the three cases shown in Figure 41.4 provides the explanation. 10 seconds after engine startup (65 seconds on the x-axis), the T2 in the two cases of postheating is about 100°C higher than in the case of passive heating (400°C and 300°C, respectively). This difference in temperature justifies the effectiveness of the postheating strategies in reducing pollutants. The prolonged postheating, although it further increases T2, does not significantly improve tailpipe emissions because the front zone of TWC1 is already active. The tailpipe cumulative emissions are practically flat after 15 seconds from engine startup, demonstrating that the conversion efficiency of TWC1 is very close to 100%. Overall, the effect of pure postheating strategies on tailpipe emissions is limited. This is an unfavorable outcome since these strategies are preferable from the driver's perspective, who does not have to wait time before driving the car due to the presence of preheating.

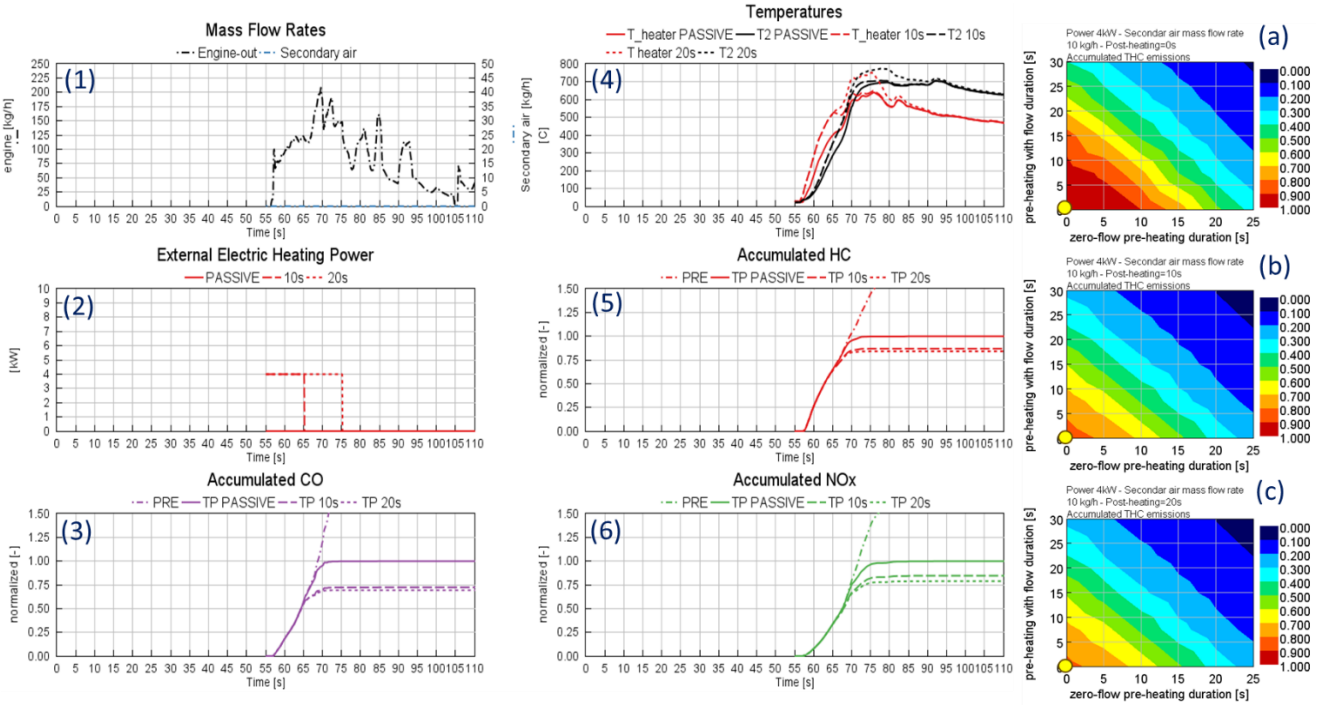

Figure 41 - Comparison between the passive (solid lines) and two pure postheating strategies (dash and dotted lines, 10 and 20 seconds of postheating, respectively). Engine flow rate, secondary air, and accumulated engine-out emissions (the same for all strategies) are indicated with dash-dot lines. (1) engine flow rate, (2) electrical powers, (3) accumulated engine-out (PRE) and tailpipe (TP) CO emissions, (4) heater and TWC1 T2 temperatures, (5) accumulated engine-out (PRE) and tailpipe (TP) HC emissions, (6) accumulated engine-out (PRE) and tailpipe (TP) NOx emissions. (a, b, c) DOE results: HC cumulative emissions 50 seconds after engine startup for respectively 0, 10, and 20 seconds of postheating, as a function of zero-flow preheating and airflow preheating durations. The yellow dots represent the three strategies analysed. Accumulated emissions are normalized with respect to the passive heating accumulated emissions 50 seconds after engine startup.

Figure 42 illustrates the tailpipe cumulative HC emissions in relation to the electrical energy spent for each strategy considered by the DOE. Each color represents one of the three postheating durations considered (no postheating, 10 and 20 seconds of postheating). As expected, the most effective strategies are those that use more energy (longer preheating durations). If we consider the most effective configuration for each postheating duration (refer to red circles in Figure 42), it is apparent that the contribution of postheating to tailpipe cumulative HC reduction is very limited. As in the case of pure postheating, for long preheating periods, the benefit of extending the postheating duration on tailpipe emissions is marginal.

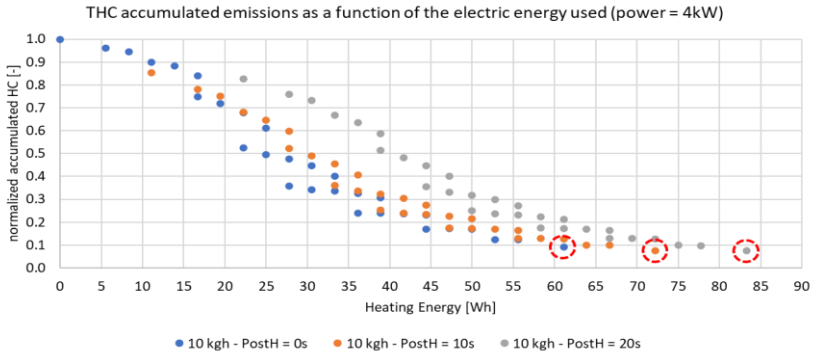

Figure 42 - Tailpipe cumulative HC emissions in relation to the electrical energy (heating energy) for each strategy considered by the DOE. Each color represents one of the three postheating durations considered (no postheating, 10 and 20 seconds of postheating). The most effective configuration for each postheating duration is highlighted by a red circle.

In Figure 43 zero-flow and airflow preheating strategies are compared, preheating duration is 25 seconds for both strategies. Even if at engine startup, T2 is higher for the airflow preheating, in the zero-flow case T2 rises more rapidly due to a higher heater temperature. Higher temperatures in the front zone of TWC1 result in lower cumulative emissions. It should be noted that, in the zero-flow case, despite the absence of airflow, T2 increases significantly, reaching 100°C at engine startup. The estimation for T2 is inaccurate because it depends on the simulation code, which does not accept a zero value for the airflow rate. The minimum value allowed by the model (0.2 kg/h) still results in a significant increase in T2. Therefore, the model overestimates the effectiveness of zero-flow preheating. This topic is analyzed in detail in Par. 4.1.1.

In summary, for a given preheating duration, zero-flow preheating is more effective in reducing emissions than airflow preheating. The advantage of zero-flow preheating increases as the airflow rate increases.

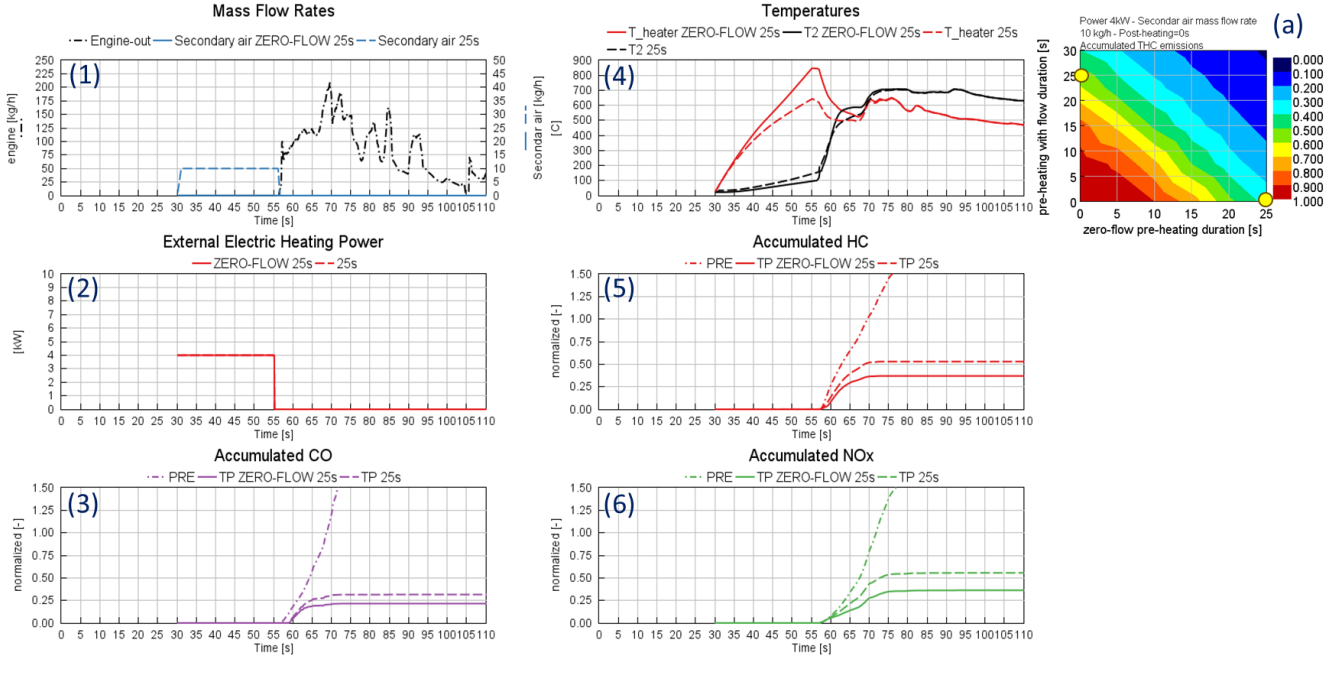

Figure 43 – Comparison between zero-flow preheating (solid lines) and airflow preheating (dashed lines) strategies with the same duration of 25 seconds. Engine flow rate and accumulated engine-out emissions (the same for all strategies) are indicated with dash-dot lines. (1) Engine and secondary air flow rates, (2) electrical powers, (3) accumulated engine-out (PRE) and tailpipe (TP) CO emissions, (4) heater and TWC1 T2 temperatures, (5) accumulated engine-out (PRE) and tailpipe (TP) HC emissions, (6) accumulated engine-out (PRE) and tailpipe (TP) NOx emissions. (a) DOE results: HC cumulative emissions 50 seconds after engine startup for 0 seconds of postheating (no postheating), as a function of zero-flow preheating and airflow preheating durations. The yellow dots represent the two strategies analysed. Accumulated emissions are normalized with respect to the passive heating accumulated emissions 50 seconds after engine

startup.

Comparing the DOE results in Figure 39.a/d/g, the dependence of the tailpipe cumulative HC emissions on the airflow preheating time as a function of the airflow rate can be analyzed. In the case of an airflow rate of 10 kg/h, emissions decrease as the airflow preheating time is extended (Figure 39.a). Moving to the case of 30 kg/h, as the zero-flow preheating time increases, HC emissions become less sensitive to the airflow preheating time (Figure 39.d). In the case of 45 kg/h, the trend related to the extension of airflow preheating reverses; the tailpipe cumulative HC emissions increase as the airflow preheating time is extended (Figure 39.g). The same behavior is also present in the DOE cases where postheating is present.

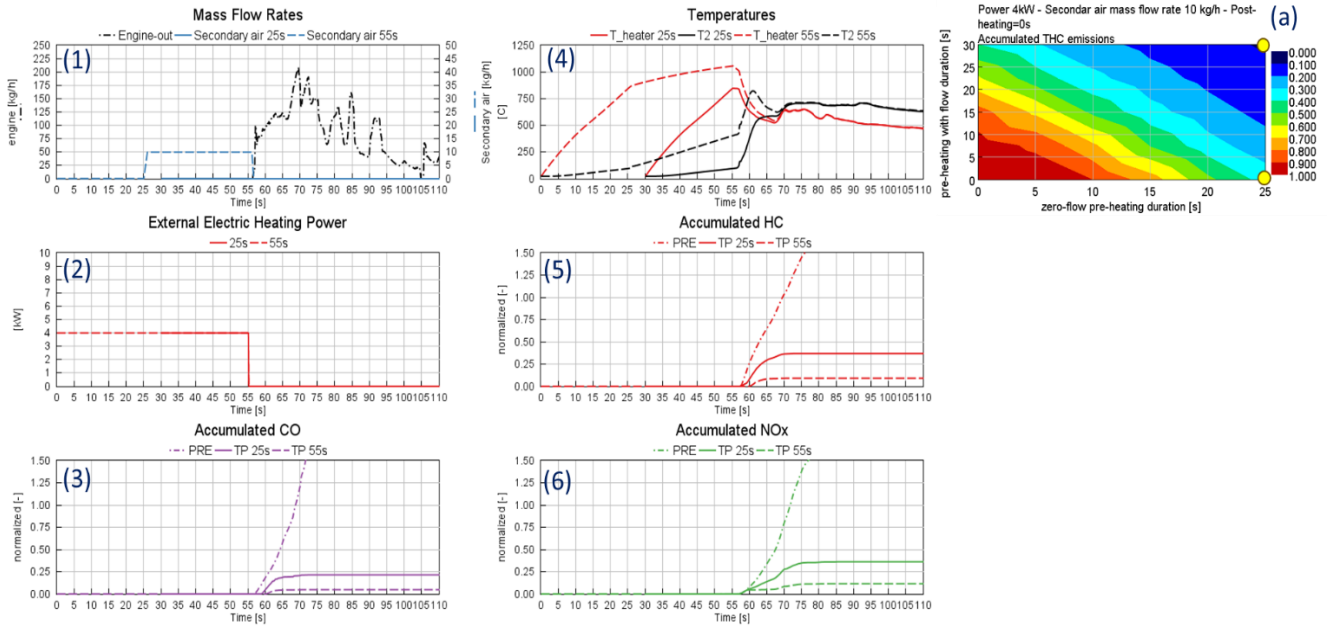

Figure 44 - Comparison between "strategy 1" (solid lines) and "strategy 2" (dashed lines) with an airflow of 10 kg/h. Engine flow rate and accumulated engine-out emissions (the same for all strategies) are indicated with dash-dot lines. (1) Engine and secondary air flow rates, (2) electrical powers, (3) accumulated engine-out (PRE) and tailpipe (TP) CO emissions, (4) heater and TWC1 T2 temperatures, (5) accumulated engine-out (PRE) and tailpipe (TP) HC emissions, (6) accumulated engine-out (PRE) and tailpipe (TP) NOx emissions. (a) DOE results: tailpipe cumulative emissions of HC 50 seconds after engine startup for 0 seconds of postheating (no postheating), as a function of zero-flow preheating and airflow preheating durations. The yellow dots represent the two strategies analyzed. Accumulated emissions are normalized with respect to the passive heating accumulated emissions 50 seconds after engine startup.

The aforementioned behaviors are explained in Figures 44-46 by analyzing the following two preheating strategies in combination with the airflow rates considered by the DOE (10, 30, and 45 kg/h, respectively):

1. "strategy 1" - 25 seconds of zero-flow preheating (solid lines).
2. "strategy 2" - 25 seconds of zero-flow followed by 30 seconds of airflow preheating (dashed lines).

In the case of an airflow rate of 10 kg/h (Figure 44), at engine startup and for the immediately following time period, "strategy 2" T2 (dashed black line) is higher than "strategy 1" T2 (solid black line) due to the longer preheating and the presence of airflow (Figure 44.4); as a consequence, tailpipe cumulative HC emissions are lower. In the case of an airflow rate of 30 kg/h (Figure 45), the cumulative HC emissions are comparable. At engine startup, "strategy 2" T2 is much higher than "strategy 1" T2 (500°C instead of 100°C), but just a few seconds later, T2 reverses. This behavior depends on the heater temperature, which is much higher for "strategy 1" due to the absence of heat exchange with the airflow (neglecting the minimum flow required by the simulation code). After engine startup, the heater's internal energy is transferred to TWC1. As a result, "strategy 1" T2 rises more rapidly than "strategy 2" T2. The two behaviors of T2 have similar consequences on the conversion efficiency of TWC1, leading to the same HC emission levels.

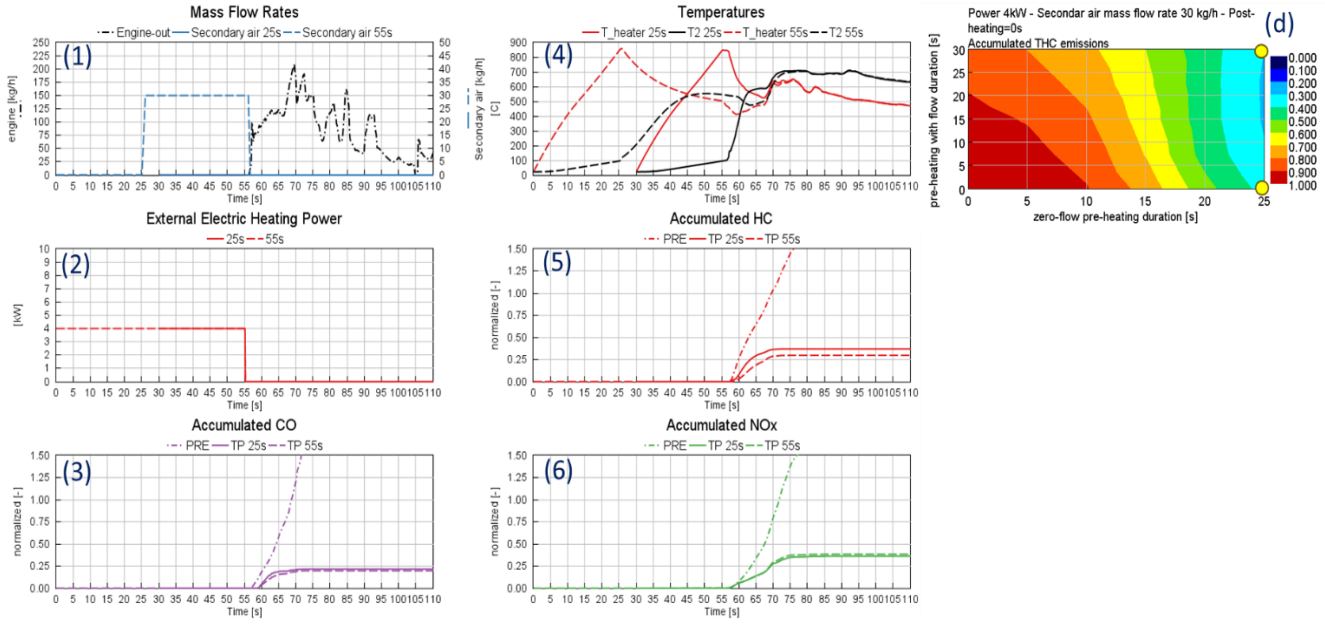

Figure 45 - Comparison between "strategy 1" (solid lines) and "strategy 2" (dashed lines) with an airflow of 30 kg/h. Engine flow rate and accumulated engine-out emissions (the same for all strategies) are indicated with dash-dot lines. (1) Engine and secondary air flow rates, (2) electrical powers, (3) accumulated engine-out (PRE) and tailpipe (TP) CO emissions, (4) heater and TWC1 T2 temperatures, (5) accumulated engine-out (PRE) and tailpipe (TP) HC emissions, (6) accumulated engine-out (PRE) and tailpipe (TP) NOx emissions. (d) DOE results: tailpipe cumulative emissions of HC 50 seconds after engine startup for 0 seconds of postheating (no postheating), as a function of zero-flow preheating and airflow preheating durations. The yellow dots represent the two strategies analyzed. Accumulated emissions are normalized with respect to the passive heating accumulated emissions 50 seconds after engine startup.

Figure 46 shows that at engine startup, for an airflow rate of 45 kg/h, "strategy 1" T_{heater} (solid red line) is significantly higher than "strategy 2" T_{heater} (dashed red line). As in the previous case, "strategy 2" T2 rapidly increases right after the start, surpassing "strategy 1" T2. The increase in "strategy 1" T2 is more pronounced compared to the previous case, which is why "strategy 1" is more effective than "strategy 2".

In summary, "strategy 2" is extremely effective at low airflow rates because it allows the heater to reach high temperatures. When the engine starts, the energy transfer from the heater to TWC1 occurs in a very short time, enabling the front zone of TWC1 (identified by T2) to activate very quickly. Increasing the airflow rate leads to lower heater temperatures at engine startup, especially for extended airflow preheating time, which penalizes "strategy 2".

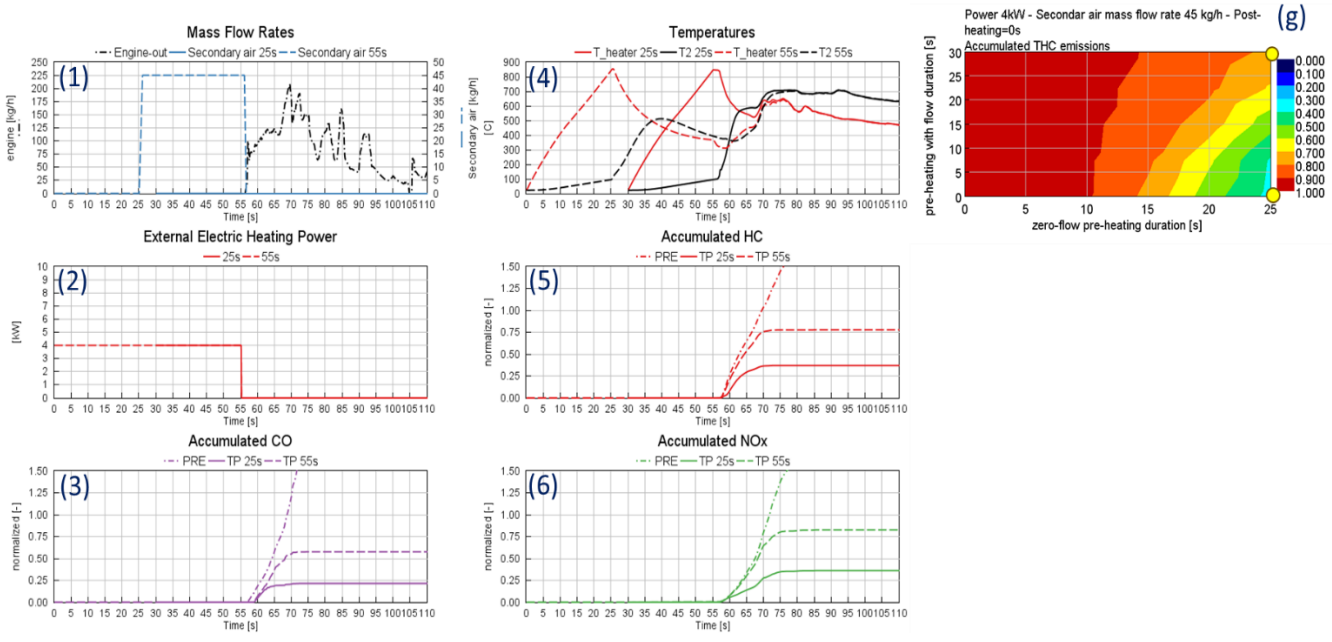

Figure 46 - Comparison between "strategy 1" (solid lines) and "strategy 2" (dashed lines) with an airflow of 45 kg/h. Engine flow rate and accumulated engine-out emissions (the same for all strategies) are indicated with dash-dot lines. (1) Engine and secondary air flow rates, (2) electrical powers, (3) accumulated engine-out (PRE) and tailpipe (TP) CO emissions, (4) heater and TWC1 T2 temperatures, (5) accumulated engine-out (PRE) and tailpipe (TP) HC emissions, (6) accumulated engine-out (PRE) and tailpipe (TP) NOx emissions. (g) DOE results: tailpipe cumulative emissions of HC 50 seconds after engine startup for 0 seconds of postheating (no postheating), as a function of zero-flow preheating and airflow preheating durations. The yellow dots represent the two strategies analyzed. Accumulated emissions are normalized with respect to the passive heating accumulated emissions 50 seconds after engine startup.

The DOE conducted at an ambient temperature of -7°C confirmed the trends observed at 23°C. Figure 47 displays the results for normalized tailpipe cumulative HC emissions 50 seconds after the engine start. The reference strategy for normalization considers the heater disabled and an ambient temperature of -7°C (refer to Figure 16 for a comparison between the -7°C and 23°C engine-out emissions). The trends for CO and NOx emissions are very similar to those for HC, as in the case of a 23°C ambient temperature (refer to Figures 89-90 in the Appendix).

All simulations conducted so far have used an electrical power of 4kW. Therefore, for a two-bank engine architecture, the required power would be 8 kW. This is a significant demand for power from a 48V battery at temperatures below zero (as the operating temperature decreases, the power output from the battery decreases significantly). Higher power levels could be more easily provided by high-voltage batteries. However, in this case, using a DC/DC converter would be necessary to reduce the voltage from the high voltage battery to the nominal 48V required by the heater.

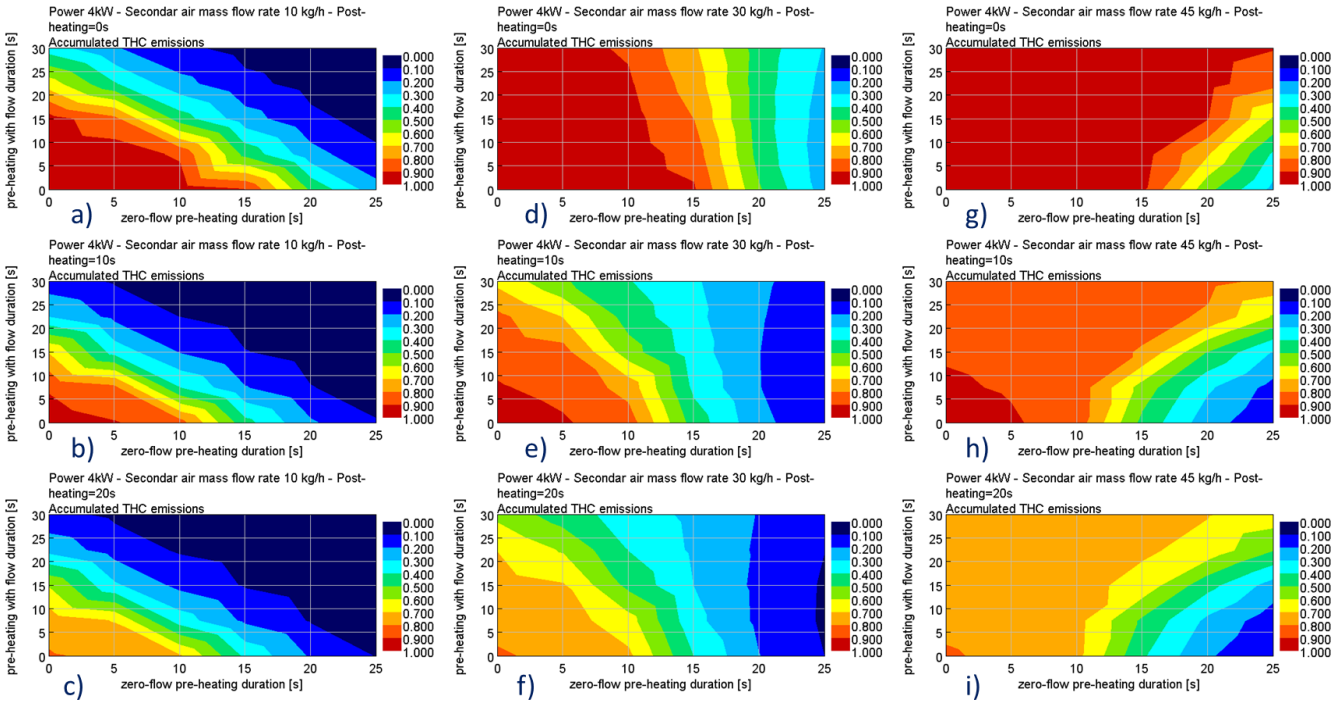

Figure 47 – DOE results at ambient temperature of -7°C: HC cumulative emissions 50 seconds after engine startup for respectively 0, 10, and 20 seconds of postheating, as a function of zero-flow preheating and airflow preheating durations. (a, b, c) airflow rate 10 kg/h, post heating of 0, 10, and 20 seconds, respectively. (d, e, f) airflow rate 30 kg/h, post heating of 0, 10, and 20 seconds, respectively. (g, h, i) airflow rate 45 kg/h, post heating of 0, 10, and 20 seconds, respectively. Accumulated emissions are normalized with respect to the passive heating results 50 seconds after engine startup.

A sensitivity analysis was carried out by varying the electric power from 4 kW to 8.6 kW. The electrical resistance of the heater was adjusted according to the required electric power. In fact, the voltage of the 48V battery (where 48V is the nominal voltage) varies depending on the state of charge (SOC) of the battery. The minimum battery voltage must be taken into account when defining the heater's electrical resistance (for example, at -7°C and low SOC levels, the voltage can drop to 35-36V). Geometrically, the electrical resistance depends on the thickness of the heater. The electric resistance is inversely proportional to the thickness, which represents the cross-sectional area of the electric conductor (Figure 48 illustrates the resistance-thickness correlation for the heater prototype). As the electric power increases for a given voltage, the electrical resistance decreases and therefore the thickness, and consequently the thermal inertia of the heater, increase.

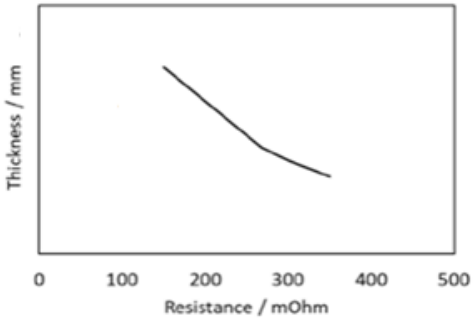

Figure 48 - Heater thickness as a function of electrical resistance. Thickness values removed for confidentiality reasons.

By setting the maximum temperature that the heater prototype can safely reach to prevent damage, the duration of the zero-flow preheating appears to be almost constant despite changes in the electric power request. This is because the variations in the heater's thermal inertia counterbalance those of the electric power

(Figure 49 shows the maximum allowed preheating time as a function of power). Therefore, in zero-flow conditions, increasing the power doesn't lead to better performances. The advantage of higher power lies in the subsequent phase of airflow preheating. In this phase, for high electric power levels, it is possible to increase the airflow rate without excessively cooling down the heater. The result is a faster heating of TWC1. The airflow rates used for the following simulations are shown in Figure 49. Nine preheating strategies were simulated limiting the maximum zero-flow preheating time to 25 seconds (in some cases slightly above the values showed in Figure 49) to avoid heater overheating (Figure 50.d)

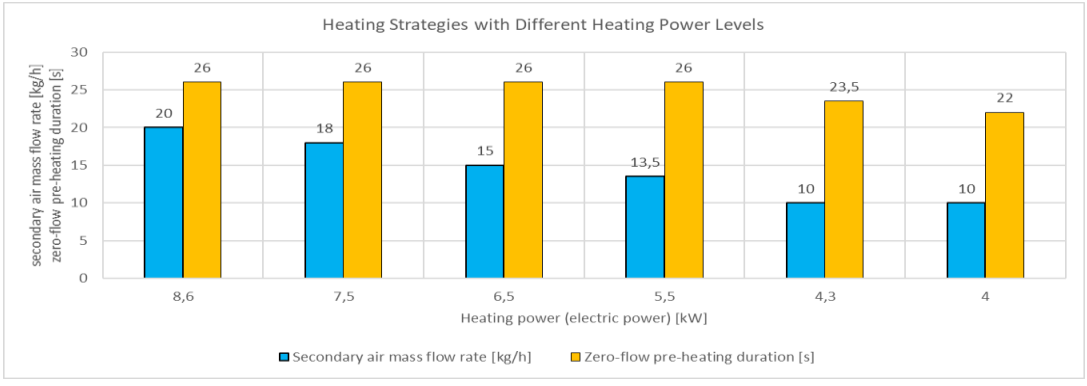

Figure 49 - Electric power sweep from 4 kW to 8.6 kW: airflow rates (blue) and maximum allowed zero-flow preheating durations (orange).

Figure 50 shows the estimated tailpipe cumulative emissions at an ambient temperature of 23°C as a function of total preheating duration. As expected, the best results are obtained with the highest power. However, for given targets of tailpipe cumulative HC, CO, and NOx emissions the differences in preheating time are not substantial between 4 and 8.6kW. They tend to become more pronounced as the considered emission targets decrease.

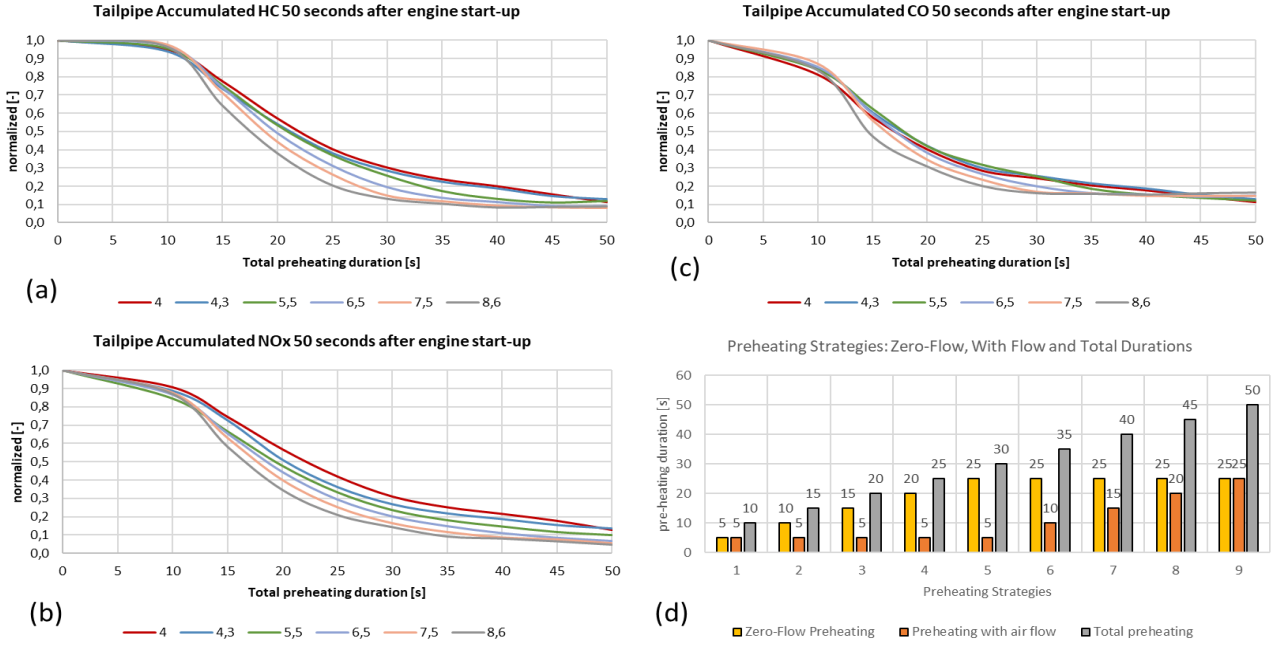

Figure 50 – Tailpipe cumulative HC, CO, NOx (50 seconds after engine start up) sensitivity to the heater electric power from 4 kW to 8.6 kW. Ambient temperature of 23°C. (a) cumulative HC, (b) cumulative CO, (c) cumulative NOx, (d) preheating strategies simulated, zero-flow and with airflow preheating durations. Emissions normalized with respect to the passive heating case (heater disabled).

3.1.4 Heater temperature distribution and transient response

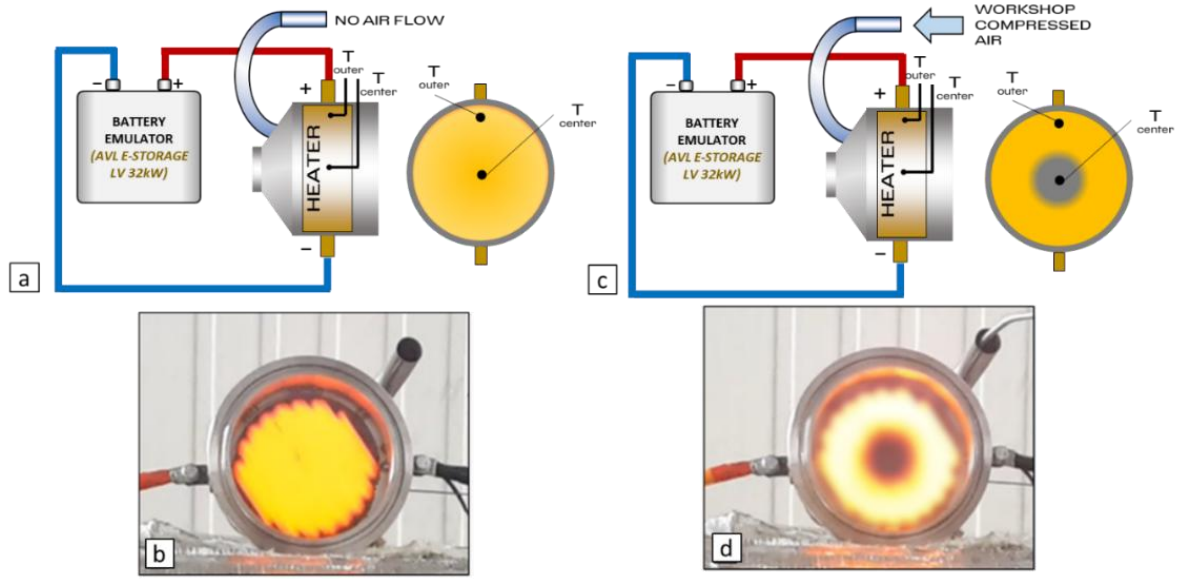

Figure 51 – (a, b) 7.5 kW 48V zero-flow heating, (c, d) 7.5 kW heating with airflow (compressed air from the workshop). The pictures are intentionally blurred for the purpose of confidentiality.

Once the heater prototype was available, the first experimental activity assessed the uniformity of the heater temperature distribution. As mentioned in Par. 2.1.3, uniform heating allows for reaching higher heater temperatures without the limitation of potential hot spots that could damage the heater.

The assessment was based on two thermocouples positioned in central and peripheral locations within the heater (refer to Par. 2.1.3 for more details). In the absence of airflow (zero-flow), the heater's center reached 800°C in 12 seconds with a heating power of 7.5 kW (T_{center} in Figure 52.b), while the peripheral area took 2 seconds longer (T_{outer} in Figure 52.b). Overall, the two thermocouples didn't deviate from each other by more than 80°C. With a heating power of 4.5 kW, the temperature transient of the heater was slower, but even in this case, the temperature uniformity was acceptable. Visual analysis also confirmed the satisfactory distribution of heater temperature (refer to Figure 51.b for the 7.5 kW case).

In the case of heating with airflow at the same power levels, the thermocouples clearly showed significant temperature inhomogeneities. When compressed air reached the heater, the central temperature (T_{center}) suddenly decreased, while the peripheral temperature (T_{outer}) continued to rise following the same pattern as in the previous test. Figure 51.d visually confirms that the airflow connection directs air solely to the central area of the heater, leading to a significant temperature difference between the center and the periphery of the heater.

These findings led to the decision to redesign the secondary air connection. The new connection was integrated into the cylinder head by connecting the secondary air circuit to the primary runners of the exhaust manifold. By moving the secondary air connection so far upstream of the heater, maximum flow uniformity at the heater's inlet was ensured (Figure 53 shows the new secondary air connection schematic).

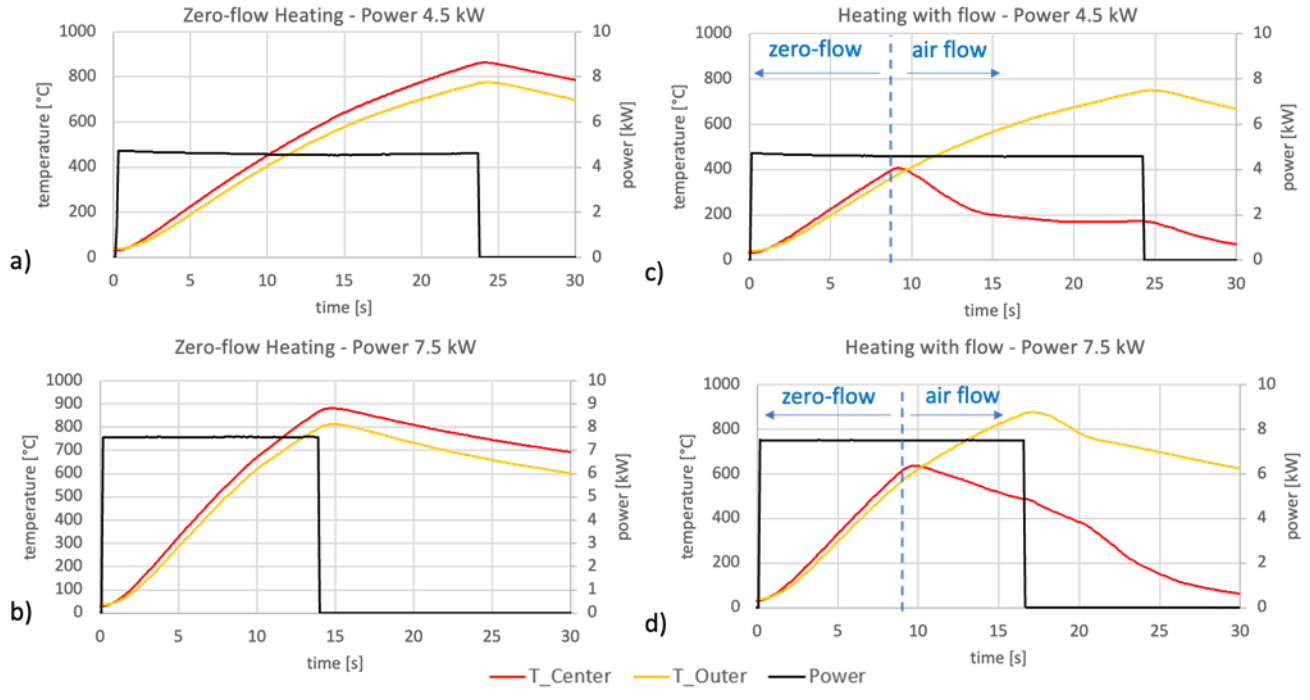

Figure 52 – heater test rig, heater temperatures in central and peripheral positions (T_Center and T_Outer): (a) power 4.5 kW, no airflow, (b) power 7.5 kW, no airflow, (c) power 4.5 kW with airflow after 8 seconds after heating started d) power 7.5 kW with airflow after 9 second after heating started.

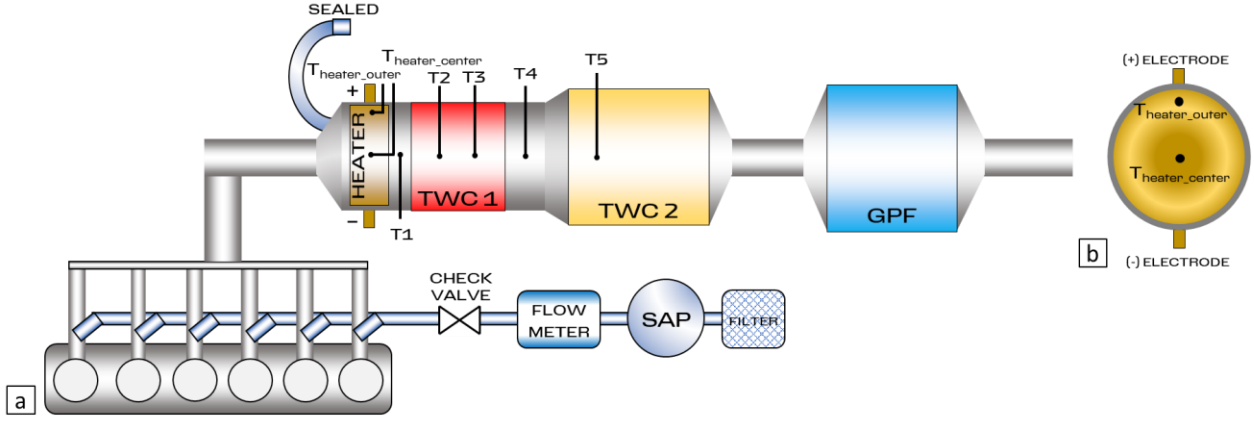

Figure 53 – Schematic of the exhaust line. Secondary air circuit connected to the exhaust manifold's primary runners (one connection per cylinder)

3.1.5 On-engine emission tests

Initially, the EHCS was tested at an ambient temperature of 23°C with the engine turned off. Subsequently, the engine was also turned on at ambient temperatures of 23°C and -7°C. The advantage of the EHCS on the tailpipe cumulative emissions of HC, CO, and NOx with various heating strategies was evaluated.

3.1.5.1 Heating with engine off

Based on the testing setup described in Par. 2.1.4, the initial activity assessed the heater temperature distribution. A strategy consisting of 15-20 seconds of zero-flow followed by 40-45 seconds of airflow heating was utilized to evaluate the functionality of the new secondary air connection. Two heating powers were used: 4 kW and 6.5 kW.

Figure 54 and Figure 55 display the results for 4 kW and 6.5 kW, respectively. For each heating power, various airflow rates were tested: 10, 20, 30, and 40 kg/h for 4 kW, and 20, 30, and 40 kg/h for 6.5 kW. The flow rate of 10 kg/h was not suitable for the 6.5 kW case as it would have led to excessively high heater temperatures.

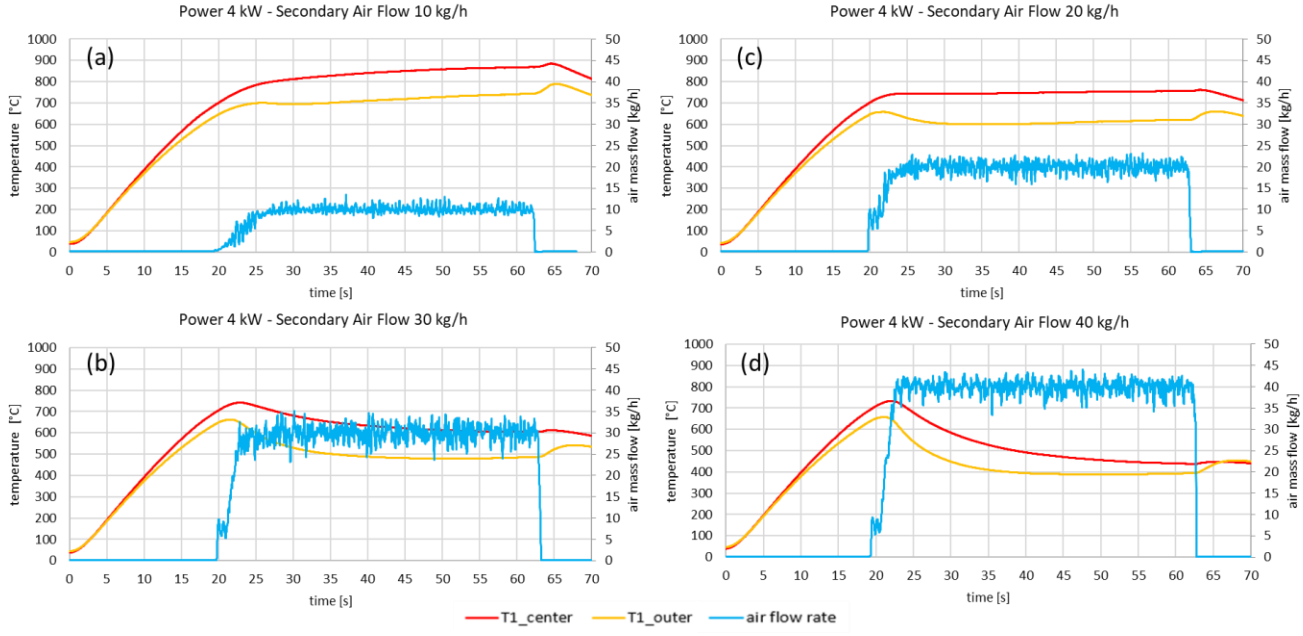

Figure 54 – Preheating strategies: 20 seconds of zero-flow heating followed by approximately 45 seconds of airflow heating. Heating Power 4 kW. (a) airflow rate 10 kg/h, (b) airflow rate 30 kg/h, (c) airflow rate 20 kg/h, (d) airflow rate 40 kg/h.

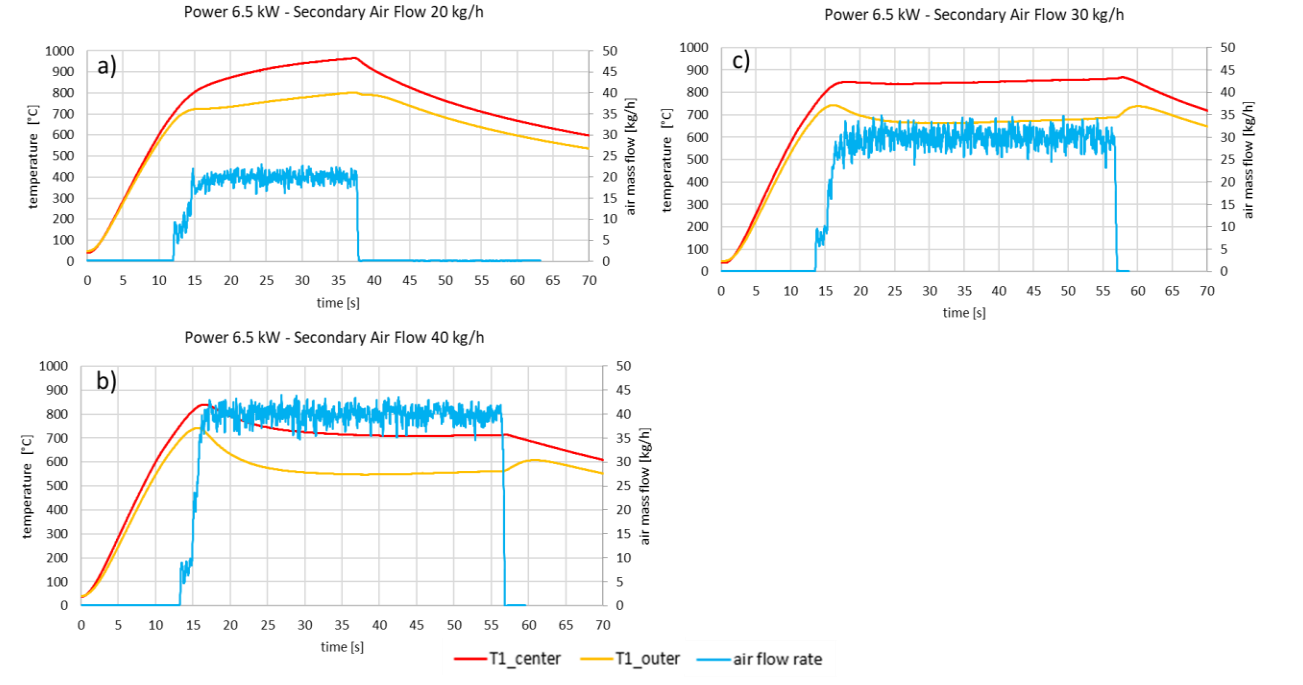

Figure 55 - Preheating strategies: 15 seconds of zero-flow heating followed by approximately 40 seconds of airflow heating. Heating Power 6.5 kW. (a) airflow rate 20 kg/h, (b) airflow rate 40 kg/h, (c) airflow rate 30 kg/h.

The results confirmed the efficient operation of the new secondary air connection. The two thermocouples placed in the heater, in central and peripheral positions (T_{center} and T_{outer}), from the moment of SAP activation, showed reasonable differences between them (approximately 100-150°C), confirming the acceptable uniformity of the heater temperature distribution. It was not possible to visually assess the temperature distribution of the heater since it was integrated into the exhaust line.

3.1.5.2 Engine cold start at 23°C

After verifying the correct operation of the heater, the EHCS was tested with the engine running at ambient temperature of 23°C. After startup the engine was operated in idling. Various durations of airflow preheating and postheating were tested (Table 7 shows the variants tested). Heating power, zero-flow preheating time, and airflow rate were set to 4kW, 22 seconds, and 45 kg/h, respectively. The tailpipe cumulative emissions 50 seconds after engine startup were normalized with respect to the passive heating strategy.

Parameter	unit	EHCS OFF	EHCS ON Zero-flow Pre-heating + Post-heating	EHCS ON Zero-flow Pre-heating + Pre-heating with flow				EHCS ON Zero-flow Pre-heating + Pre-heating with flow + Post-heating
Electrical Heating Power [kW]	[kW]	-	4	4	4	4	4	4
Secondary air flow rate [kg/h]	[kgh]	-	0	45	45	45	45	45
Zero-flow pre-heating duration	[s]	-	22	22	22	22	22	22
Pre-heating with flow duration	[s]	-	0	5	10	20	30	10
Total pre-heating duration	[s]	-	22	27	32	42	52	32
Post-heating duration	[s]	-	15	0	0	0	0	10
Heating electrical energy	[Wh]	-	41	30	36	47	58	47
Accumulated CO TP (norm.)	[-]	1.000	0.358	0.143	0.094	0.064	0.039	0.078
Accumulated HC TP (norm.)	[-]	1.000	0.545	0.244	0.218	0.185	0.163	0.209
Accumulated NOx TP (norm.)	[-]	1.000	0.870	0.961	1.013	0.961	1.013	1.000

Table 7 – Heating strategy variants tested. Heating power, duration of the zero-flow preheating, and airflow fixed at 4kW, 22 seconds, and 45 kg/h, respectively. Variations in the duration of airflow preheating: 0, 5, 10, 20, and 30 seconds. Two variants of postheating duration tested: 10 and 15 seconds. Tailpipe cumulative emissions 50 seconds after engine startup normalized with respect to the passive heating strategy (EHCS OFF).

Figure 56 illustrates the main results. NOx emissions were found to be almost insensitive to the heating strategy. This behavior depends on the engine lambda slightly shifted towards lean mixtures to enhance the effectiveness of the TWC in the conversion of HC and CO at the expense of NOx. Cumulative HC and CO emissions exhibited similar trends.

The zero-flow preheating followed by 15 seconds of postheating allowed for a considerable reduction in emissions. This strategy does not require the presence of the secondary air circuit, with evident advantages in terms of costs, space, and weight.

Then, postheating was disabled, and the duration of the airflow preheating was varied, assuming values of 5, 10, 20, and 30 seconds, respectively. Tailpipe emissions, already very low for a short preheating of 5 seconds, decreased further with longer durations. This outcome contradicts the simulation results (the deviation between simulation and experimental results is discussed in Par. 4.1.1).

As predicted by simulation, adding 10 seconds of postheating to the preheating strategy (22 seconds of zero-flow followed by 10 seconds of airflow preheating) had a limited effect on reducing emissions.

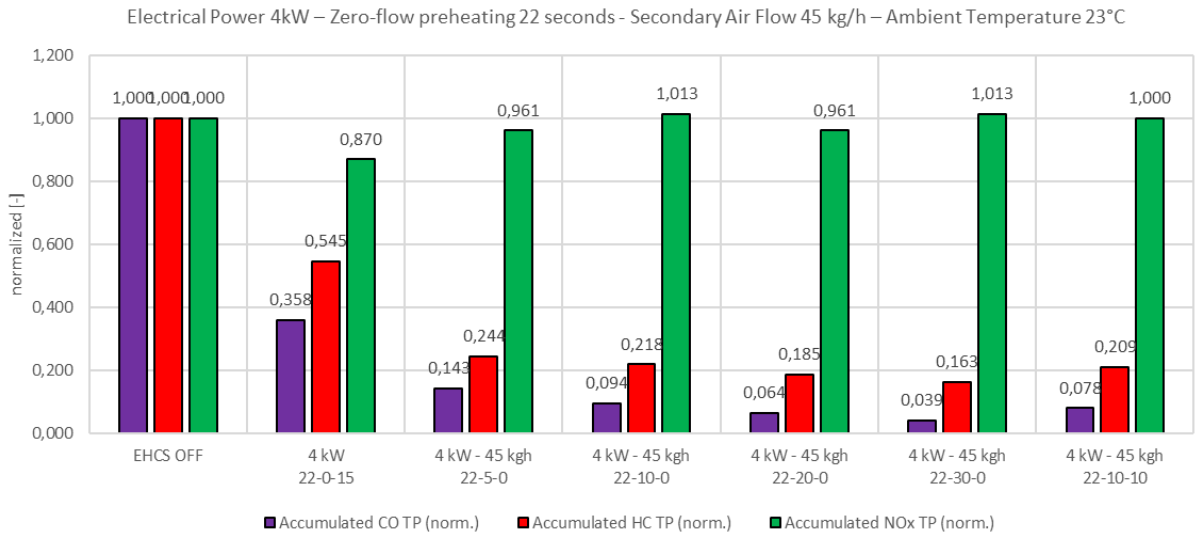

Figure 56 – Heating strategy variants tested. Heating power, duration of the zero-flow preheating, and airflow fixed at 4kW, 22 seconds, and 45 kg/h, respectively. The durations of zero-flow preheating, airflow preheating, and postheating are represented in the figure as three values separated by a dash (e.g., 22-10-10 stands for 22 seconds of zero-flow preheating, 10 seconds of airflow preheating, 10 seconds of postheating). Tailpipe cumulative emissions 50 seconds after engine startup normalized with respect to the passive heating strategy (EHCS OFF).

The experimental results can be explained by examining the TWC1 temperatures. Below is a comparison between the two heating strategies with airflow preheating of respectively 10 and 30 seconds.

In the case of 10 seconds of airflow preheating, at engine startup (55 seconds in Figure 57), T2 is 200°C and reaches approximately 500°C in about 5 seconds. The front zone of TWC1, through the exchange of energy with the heater, tends to reach the same temperature as the heater. In fact, approximately 500°C is also the average heater temperature (average between T_{center} and T_{outer}).

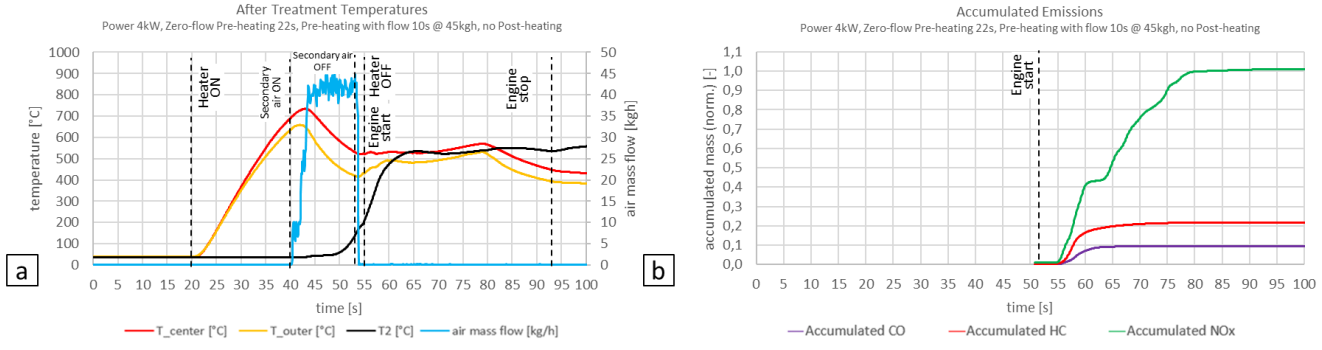

Figure 57 – (a) heater and TWC1 (T2) temperatures, (b) normalized tailpipe cumulative emissions. Heating strategy: heating power 4kW, duration of the zero-flow preheating 22s, duration of airflow preheating 10s, and airflow rate 45 kg/h. Tailpipe cumulative emissions 50 seconds after engine startup normalized with respect to the passive heating strategy (EHCS OFF).

In the case of 30 seconds of airflow preheating, at engine startup (55 seconds in Figure 58), T2 is 450°C and does not rise further in the following 5 seconds because it is already in the same temperature range as the heater.

In summary, with an airflow rate of 45 kg/h, the heater temperature during the airflow preheating drops from 700°C (at the end of the zero-flow preheating) to a value in the 400-500°C range, depending on the duration of the airflow preheating. The front zone of TWC1 reaches a temperature very close to that of the heater right after engine startup.

Tailpipe emissions slightly decrease with the 30-second airflow preheating strategy. The difference compared to the 10-second case is marginal because, as previously mentioned, TWC1 heats up very quickly right after engine startup. When comparing CO and HC, the reduction in CO is more pronounced because the catalyzed oxidation reactions of CO have lower activation temperatures, and consequently, CO is more sensitive than HC to the TWC1 temperature at engine startup.

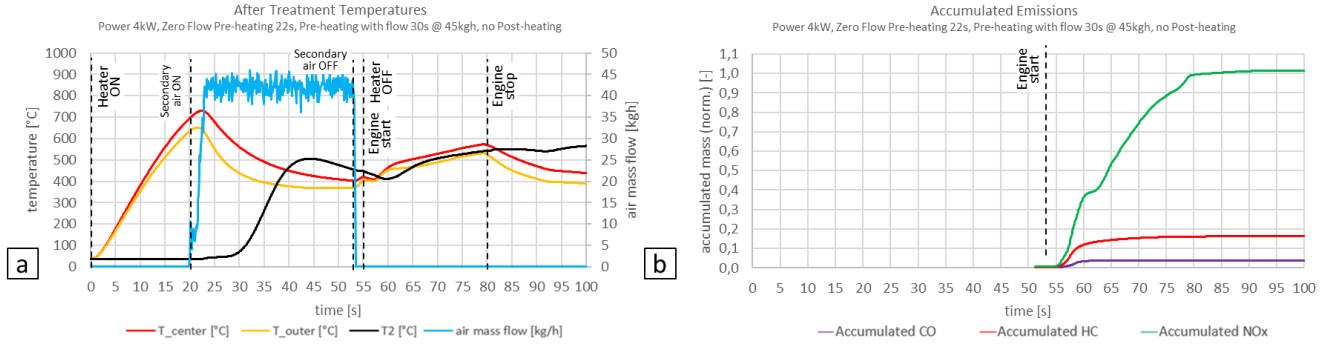

Figure 58 – (a) heater and TWC1 (T2) temperatures, (b) normalized tailpipe cumulative emissions. Heating strategy: heating power 4kW, duration of the zero-flow preheating 22s, duration of airflow preheating 30s, and airflow rate 45 kg/h. Tailpipe cumulative emissions 50 seconds after engine startup normalized with respect to the passive heating strategy (EHCS OFF).

The same variations were carried out with an airflow rate of 30 kg/h (Table 8). As in the 45 kg/h case, heating power and duration of the zero-flow preheating were set to 4kW and 22 seconds, respectively.

Parameter	unit	EHCS OFF	EHCS ON Zero-flow Pre-heating + Post-heating	EHCS ON Zero-flow Pre-heating + Pre-heating with flow				EHCS ON Zero-flow Pre-heating + Pre-heating with flow + Post-heating
Electrical Heating Power [kW]	[kW]	-	4	4	4	4	4	4
Secondary air flow rate [kg/h]	[kgh]	-	0	30	30	30	30	30
Zero-flow pre-heating duration	[s]	-	22	22	22	22	22	22
Pre-heating with flow duration	[s]	-	0	5	10	20	30	10
Total pre-heating duration	[s]	-	22	27	32	42	52	32
Post-heating duration	[s]	-	15	0	0	0	0	10
Heating electrical energy	[Wh]	-	41	30	36	47	58	47
Accumulated CO TP (norm.)	[-]	1.000	0.358	0.179	0.139	0.061	0.035	0.099
Accumulated HC TP (norm.)	[-]	1.000	0.545	0.362	0.348	0.161	0.165	0.243
Accumulated NOx TP (norm.)	[-]	1.000	0.870	0.844	0.805	1.117	1.039	1.000

Table 8 - Heating strategy variants tested. Heating power, duration of the zero-flow preheating, and airflow rate fixed at 4kW, 22 seconds, and 30 kg/h, respectively. Variations in the duration of airflow preheating: 0, 5, 10, 20, and 30 seconds. Two variants of postheating duration tested: 10 and 15 seconds. Tailpipe cumulative emissions 50 seconds after engine startup normalized with respect to the passive heating strategy (EHCS OFF).

Figure 59 illustrates the main results. As in the 10 kg/h case, NOx emissions were found to be almost insensitive to the heating strategy for the same reason. HC and CO emissions also exhibited similar trends, confirming the increased effectiveness of the EHCS as the airflow preheating was extended.

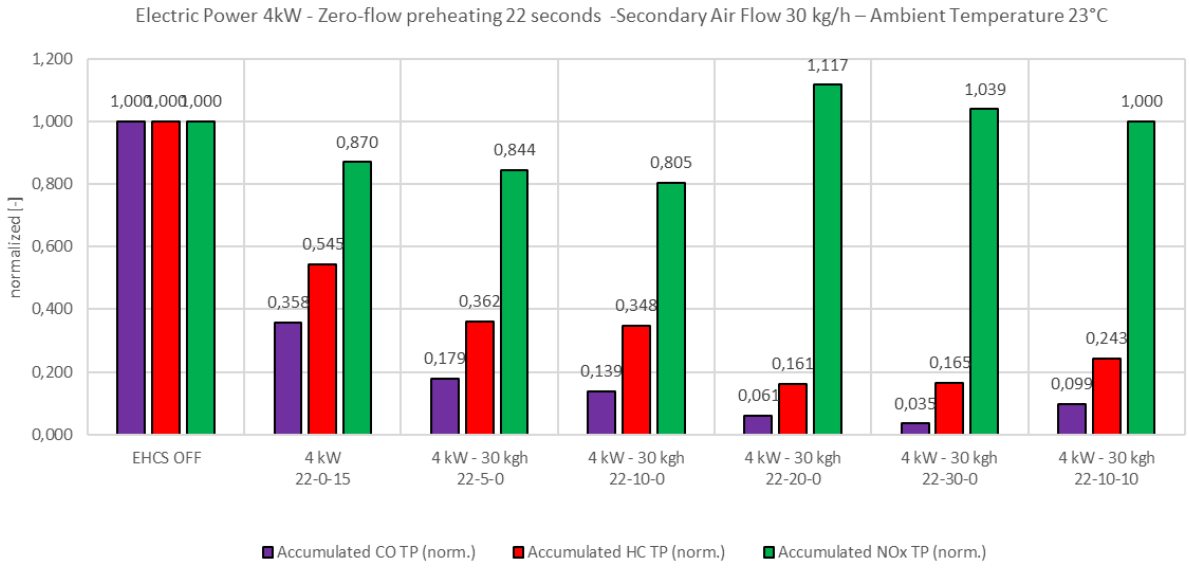

Figure 59 - Heating strategy variants tested. Heating power, duration of the zero-flow preheating, and airflow rate fixed at 4kW, 22 seconds, and 30 kg/h, respectively. The durations of zero-flow preheating, airflow preheating, and postheating are represented in the figure as three values separated by a dash (e.g. 22-10-10 stands for 22 seconds of zero-flow preheating, 10 seconds of airflow preheating, 10 seconds of postheating). Tailpipe cumulative emissions 50 seconds after engine startup normalized with respect to the passive heating strategy (EHCS OFF).

Due to lower airflow rate (Figures 60-61), 30 kg/h instead of 45 kg/h, the heater is hotter at engine startup (close to 600°C). While confirming the behavior observed in the 45 kg/h case, the greater difference in T2 at engine startup between 10 and 30 seconds of airflow preheating makes the influence of extended preheating on tailpipe emissions more pronounced.

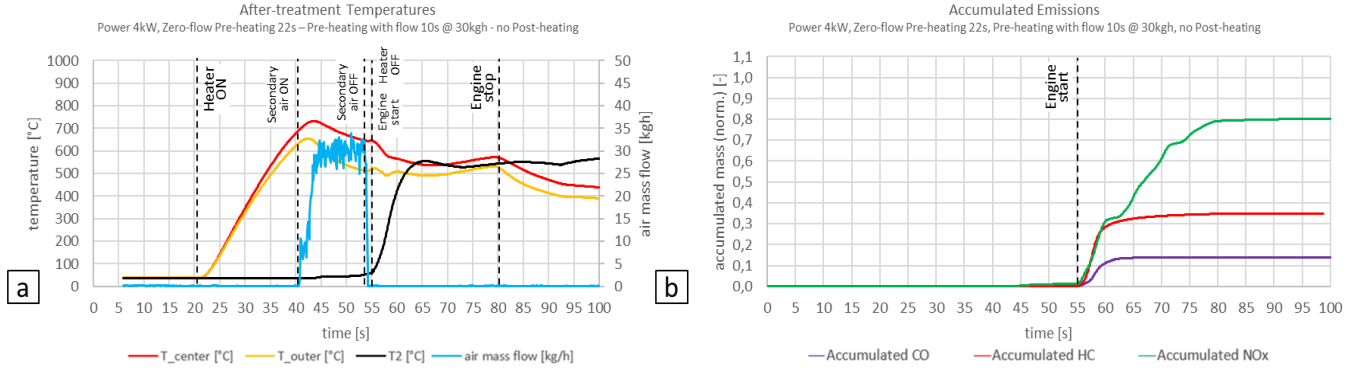

Figure 60 - (a) heater and TWC1 (T2) temperatures, (b) normalized tailpipe cumulative emissions. Heating strategy: heating power 4kW, duration of the zero-flow preheating 22s, duration of airflow preheating 10s, and airflow rate 30 kg/h. Tailpipe cumulative emissions 50 seconds after engine startup normalized with respect to the passive heating strategy (EHCS OFF).

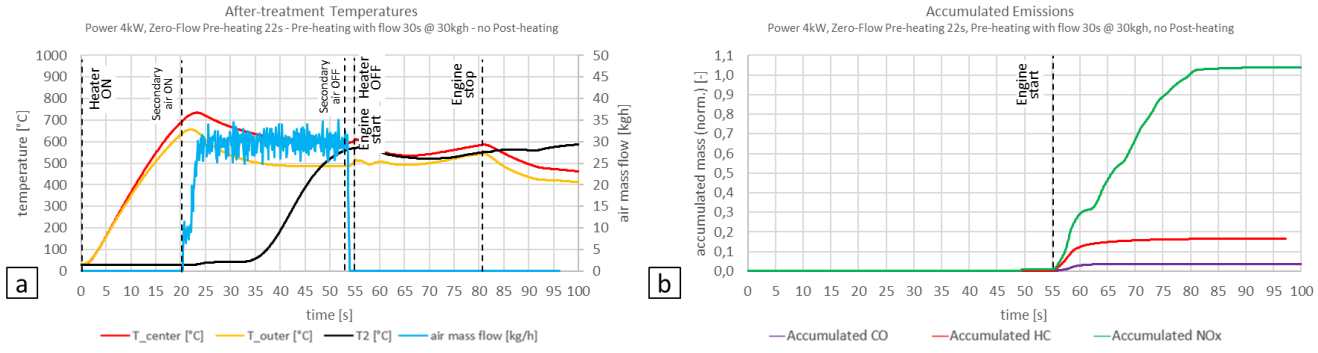

Figure 61 - (a) heater and TWC1 (T2) temperatures, (b) normalized tailpipe cumulative emissions. Heating strategy: heating power 4kW, duration of the zero-flow preheating 22s, duration of airflow preheating 30s, and airflow rate 30 kg/h. Tailpipe cumulative emissions 50 seconds after engine startup normalized with respect to the passive heating strategy (EHCS OFF).

The same variations were carried out with an airflow rate of 10 kg/h (Table 9). Figure 62 illustrates the main results. As in the 45 and 30 kg/h cases, heating power and duration of the zero-flow preheating were kept fixed at 4kW, 22 seconds, respectively.

Parameter	unit	EHCS OFF	EHCS ON Zero-flow Pre-heating + Post-heating	EHCS ON Zero-flow Pre-heating + Pre-heating with flow				EHCS ON Zero-flow Pre-heating + Pre-heating with flow + Post-heating
Electrical Heating Power [kW]	[kW]	-	4	4	4	4	4	4
Secondary air flow rate [kg/h]	[kgh]	-	0	10	10	10	10	10
Zero-flow pre-heating duration	[s]	-	22	22	22	22	22	22
Pre-heating with flow duration	[s]	-	0	5	10	20	30	10
Total pre-heating duration	[s]	-	22	27	32	42	52	32
Post-heating duration	[s]	-	15	0	0	0	0	10
Heating electrical energy	[Wh]	-	41	30	36	47	58	47
Accumulated CO TP (norm.)	[-]	1.000	0.358	0.243	0.191	0.104	0.071	0.194
Accumulated HC TP (norm.)	[-]	1.000	0.545	0.368	0.336	0.178	0.152	0.440
Accumulated NOx TP (norm.)	[-]	1.000	0.870	1.000	1.052	1.104	1.091	0.909

Table 9 - Heating strategy variants tested. Heating power, duration of the zero-flow preheating, and airflow rate fixed at 4kW, 22 seconds, and 10 kg/h, respectively. Variations in the duration of airflow preheating: 0, 5, 10, 20, and 30 seconds. Two variants of postheating duration tested: 10 and 15 seconds. Tailpipe cumulative emissions 50 seconds after engine startup normalized with respect to the passive heating strategy (EHCS OFF).

As expected, with an airflow rate of 10 kg/h (Figures 63-64), the heater temperature at engine startup is even higher than in the previous cases (approximately 750°C). However, even with 30 seconds of airflow preheating, the heating strategy does not manage to completely heat the front part of TWC1 (T2 is relatively low at engine startup). The preheating of a smaller front area compared to that monitored by T2 (T2 positioned at 1/4 of the length of TWC1) is still sufficient to achieve significantly lower tailpipe emissions respect to the case with shorter preheating.

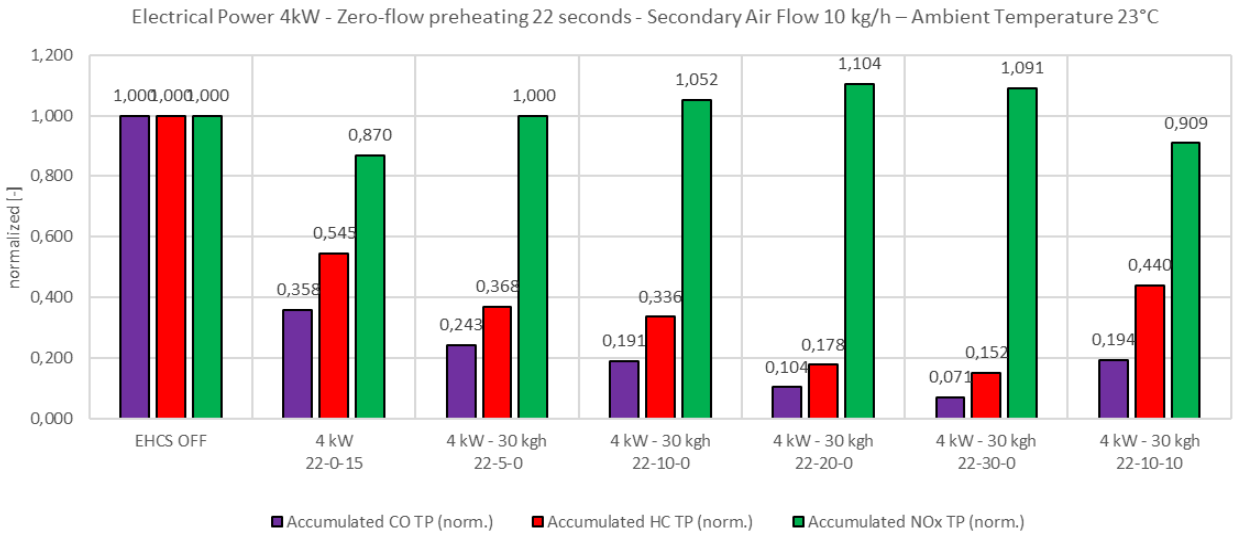

Figure 62 - Heating strategy variants tested. Heating power, duration of the zero-flow preheating, and airflow rate fixed at 4kW, 22 seconds, and 10 kg/h, respectively. The durations of zero-flow preheating, airflow preheating, and postheating are represented in the figure as three values separated by a dash (e.g. 22-10-10 stands for 22 seconds of zero-flow preheating, 10 seconds of airflow preheating, 10 seconds of postheating). Tailpipe cumulative emissions 50 seconds after engine startup normalized with respect to the passive heating strategy (EHCS OFF).

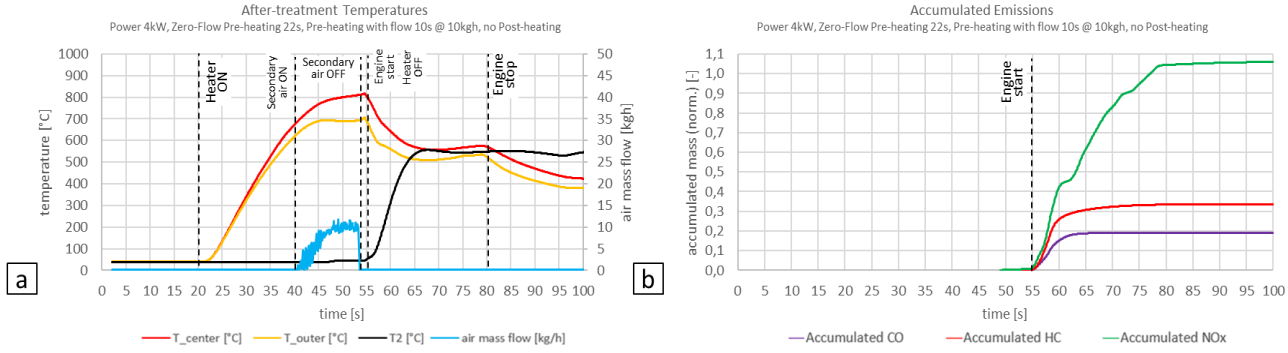

Figure 63 – (a) heater and TWC1 (T2) temperatures, (b) normalized tailpipe cumulative emissions. Heating strategy: heating power 4kW, duration of the zero-flow preheating 22s, duration of airflow preheating 10s, and airflow rate 10 kg/h. Tailpipe cumulative emissions 50 seconds after engine startup normalized with respect to the passive heating strategy (EHCS OFF).

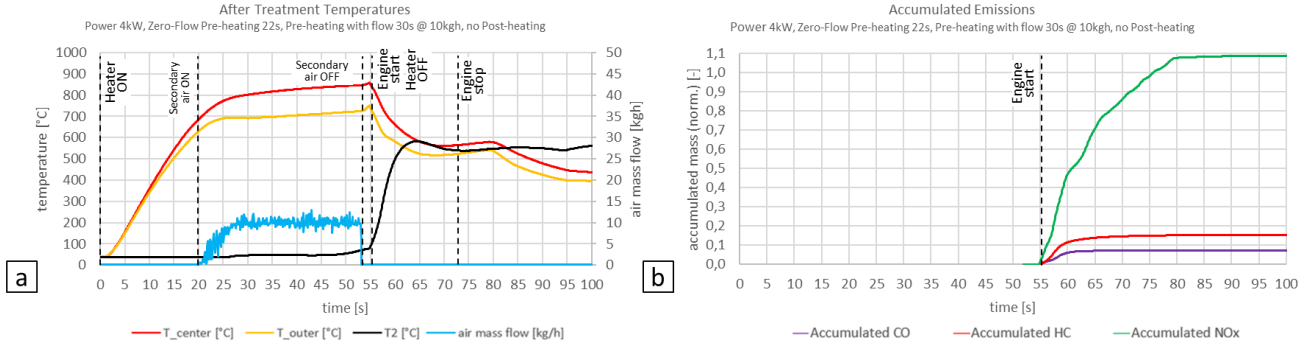

Figure 64 - (a) heater and TWC1 (T2) temperatures, (b) normalized tailpipe cumulative emissions. Heating strategy: heating power 4kW, duration of the zero-flow preheating 22s, duration of airflow preheating 30s, and airflow rate 10 kg/h. Tailpipe cumulative emissions 50 seconds after engine startup normalized with respect to the passive heating strategy (EHCS OFF).

Figure 65 shows the HC and CO tailpipe emissions as a function of airflow preheating duration and airflow rate. This representation indicates a clear tendency for CO emissions to decrease with increasing airflow preheating duration and rate.

Based on previous analysis, the temperature of the front zone of TWC1 at engine startup plays a key role in reducing tailpipe emissions. In fact, T2 at engine startup increases with the prolongation of the airflow preheating duration and with the increase of the airflow rate.

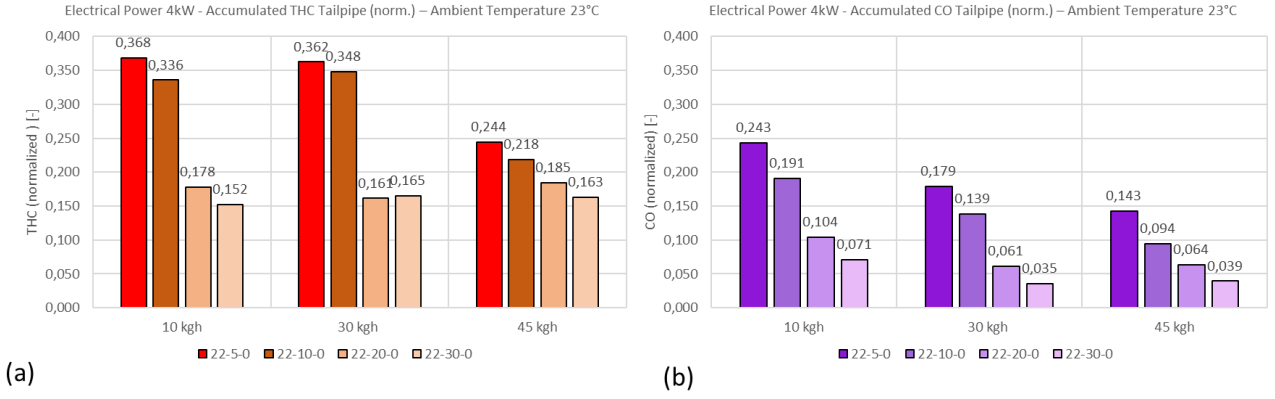

Figure 65 - Tailpipe cumulative HC (a) and CO (b) as a function of the airflow rate (10, 30, and 45 kg/h) and the airflow preheating duration (5, 10, 20, and 30 seconds). Zero-flow preheating, airflow preheating, and postheating durations are represented as three values separated by a dash (e.g. 22-10-10 stands for 22 seconds of zero-flow preheating, 10 seconds of airflow preheating, 10 seconds of postheating). Tailpipe cumulative emissions 50 seconds after engine startup normalized with respect to the passive heating strategy (EHCS OFF).

The cumulative HC emissions follow the same trend as CO, but once the airflow preheating duration exceeds 10 seconds, no significant differences are observed in the emission reduction. This behavior can be explained by considering that the activation temperatures of the catalytic reactions involving HC are higher than those for CO and benefit from the higher temperatures that TWC1 can reach right after engine startup for shorter airflow preheating periods.

The experimental behavior of the EHCS contradicted the results of the simulations (Par. 3.1.3), an explanation is provided in Par. 4.1.1.

3.1.5.3 Engine Cold Start at -7°C

At ambient temperature of -7°C, only two EHCS heating strategies were tested, in addition to the passive strategy, which was then used to normalize the emission results. The electrical power remained at 4 kW, and the duration of the zero-flow preheating was kept constant at 22 seconds. The two tested strategies are described in Table 10. The first strategy involves 10 seconds of postheating, while the second one includes 30 seconds of preheating with an airflow rate of 45 kg/h. This latter strategy replicates the one that achieved the best experimental results in reducing CO and HC emissions at 23°C (Par.3.1.5.2).

Parameter	unit	EHCS OFF	EHCS ON Zero-flow Pre-heating + Post-heating	EHCS ON Zero-flow Pre-heating + Pre-heating with flow
Electrical Heating Power [kW]	[kW]	-	4	4
Secondary air flow rate [kg/h]	[kgh]	-	0	45
Zero-flow pre-heating duration	[s]	0	22	22
Pre-heating with flow duration	[s]	0	0	30
Total pre-heating duration	[s]	0	22	52
Post-heating duration	[s]	0	10	0
Heating electrical energy	[Wh]	-	36	58
Accumulated CO TP (norm.)	[-]	1.000	0.827	0.158
Accumulated HC TP (norm.)	[-]	1.000	1.196	0.476
Accumulated NOx TP (norm.)	[-]	1.000	0.914	0.314

Table 10 - Heating strategy variants tested at -7°C. Heating power, duration of the zero-flow preheating, and airflow rate fixed at 4kW, 22 seconds, respectively. Tailpipe cumulative emissions 50 seconds after engine startup normalized with respect to the passive heating strategy (EHCS OFF).

Compared to the 23°C case, the engine-out emissions were significantly different (Figure 16): CO and HC emissions were higher, and the air-to-fuel ratio at which the engine operated was slightly shifted towards rich mixtures. These characteristics of engine operation enabled high efficiency of the catalysts in converting NOx, albeit at the expense of CO and HC. For all three species, a significant reduction in tailpipe emissions was detected, but it was less pronounced than in the 23°C case (Figure 66). In addition to the different engine operation characteristics, the starting temperature of TWC1 was lower, and the airflow was also at a lower temperature, accentuating the air-cooling effect on the heater.

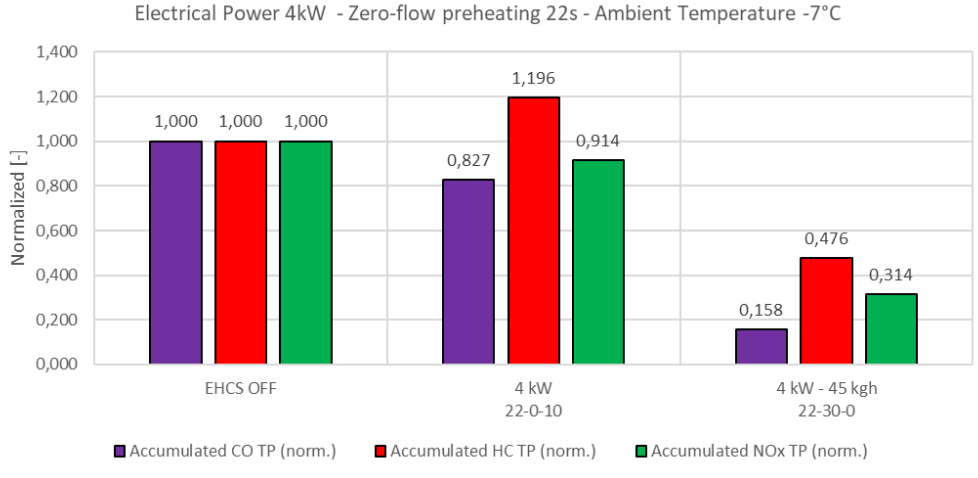

Figure 66 - Cumulative emission results testing at -7°C the heating strategies described in Table 10. The durations of zero-flow preheating, airflow preheating, and postheating are represented in the figure as three values separated by a dash (e.g. 22-0-10 stands for 22 seconds of zero-flow preheating, 0 seconds of airflow preheating, 10 seconds of postheating). Tailpipe cumulative emissions 50 seconds after engine startup normalized with respect to the passive heating strategy (EHCS OFF).

Figure 67 details the results of the most effective strategy. A total preheating time of 52 seconds (22 seconds of zero-flow followed by 30 seconds of airflow preheating) enables the engine to start with the front zone of TWC1 heated. Temperatures in the rear portion of TWC1 are still in the "plateau phase" of the water phase change (Par. 4.1.1). Once the engine is started, engine exhaust gas contributes to further heating both the front and rear portions of TWC1, as well as the remaining components in the exhaust system. At the time of engine start (time equal to 0 s in Figure 67), T2 is around 350°C while the heater is at about 300°C. These temperatures are close to the light-off threshold of TWC but lower than in the 23°C case.

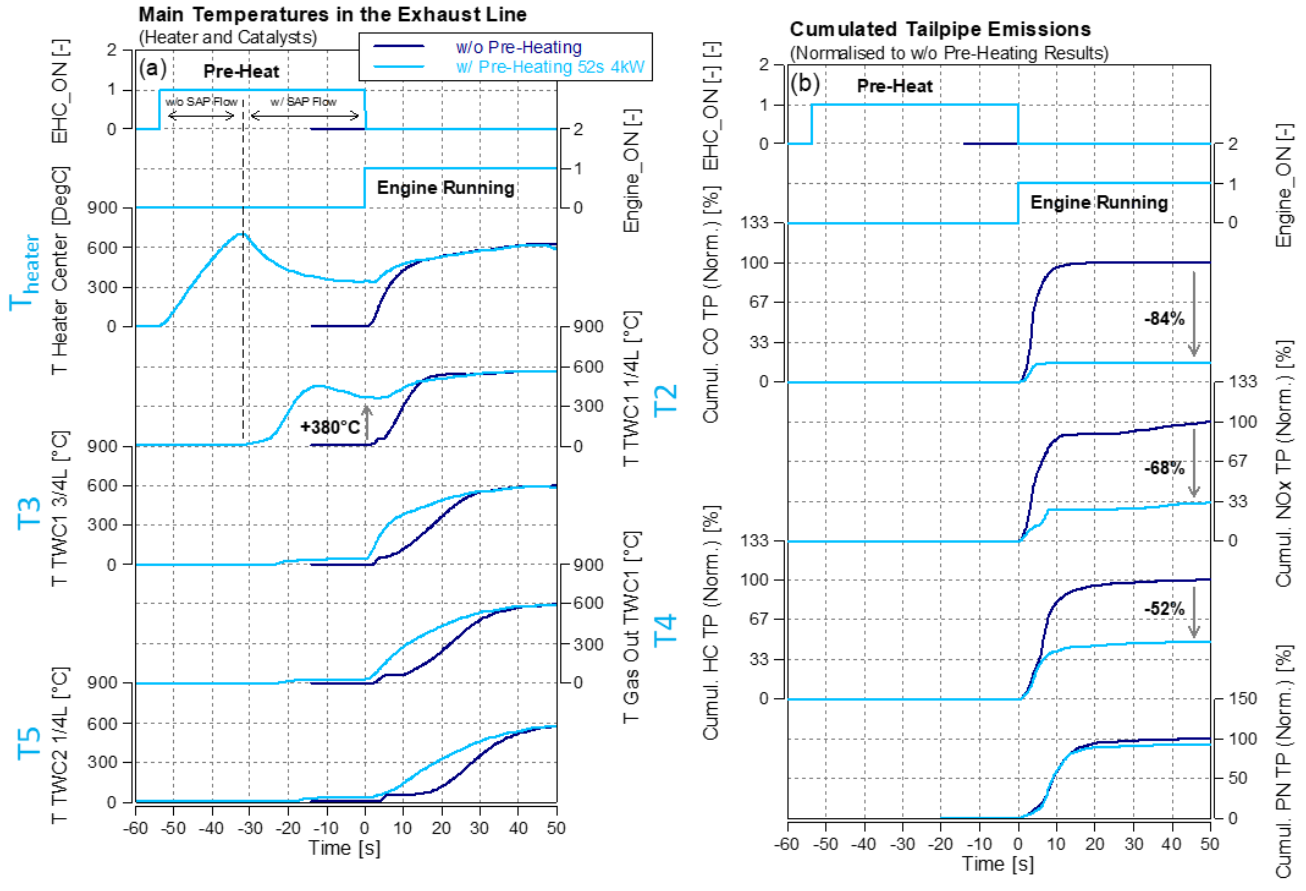

Figure 67: Experimental results of on-engine tests: EHC preheating (52s at 4kW) followed by 50s of engine cold-start idle at -7°C, compared to baseline without active heating. Graphs show heating performance of TWC1 and TWC2 as measured by thermocouples embedded in the bricks (a) and normalized cumulated tailpipe emissions results (b).

As the EHCS does not produce pollutants, tailpipe emissions come solely from the engine. Tailpipe cumulative emissions after 50 seconds of engine idling were reduced by 84% for CO, 68% for NOx, and 52% for HC, demonstrating the benefits of active heating during engine cold-start at -7°C.

3.2 Fuel Burner System (FBS)

3.2.1 Burner combustion and burner-out emissions optimization

The experimental activity on the FBS began with the characterization of the burner startup (methods described in Par. 2.2.1) in order to identify the correct heating strategy. During the burner startup, pollutant emissions exhibited a peak due to the time required to ignite the mixture (startup time), the lambda, the poor homogeneity of the mixture, and the low combustion efficiency influenced by the cold walls of the combustion chamber.

Figure 68.a shows that a stoichiometric or slightly rich startup lambda ensures quick burner fire-up with limited dispersion. The startup delay increases with leaner values of lambda. The line identified as "Front of worst-case startup" in Figure 68.a highlights this trend. However, a lean value of lambda minimizes peak pollutant concentrations at the start of CO (Figure 68.b) and PN (Figure 68.e). Significant mixture leaning is not beneficial for further reducing emissions. NOx concentration (Figure 68.c) decreases with lean lambda values due to the lower temperatures reached during combustion. The peak burner-out HC concentration (Figure 68.d) remains rather constant against lambda at the start. This is probably due to the worsening of startup delay: longer burner startups in lean conditions result in an increased amount of fuel injected before the start of combustion, thus compensating for the enleanement.

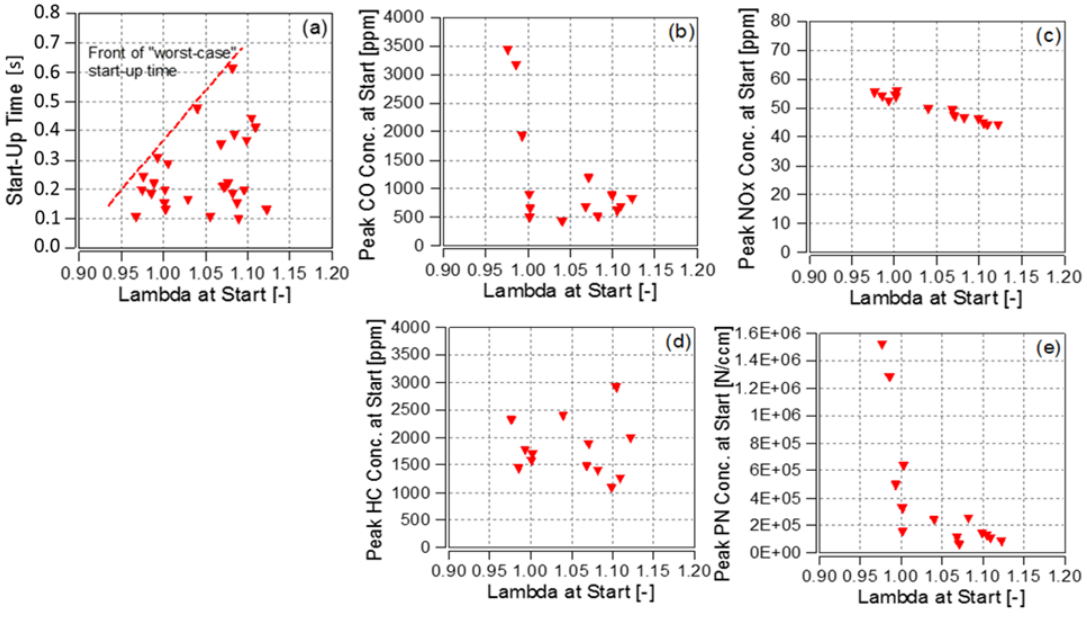

Figure 68: burner startup time (a), and peak burner-out pollutant concentrations, (b) to (e), during burner fire-up as a function of burner lambda at start. Measurements refer to ambient temperature of 23°C.

Consequently, the optimized startup lambda for the burner should be close to stoichiometric, with a slight lean bias to keep emissions to a minimum and achieve both good repeatability and short startup time. Similar results were observed at different ambient temperatures.

Once the correct startup control strategy was identified, the burner mixture was optimized for both thermal power and emissions in firing operation ("steady state operation").

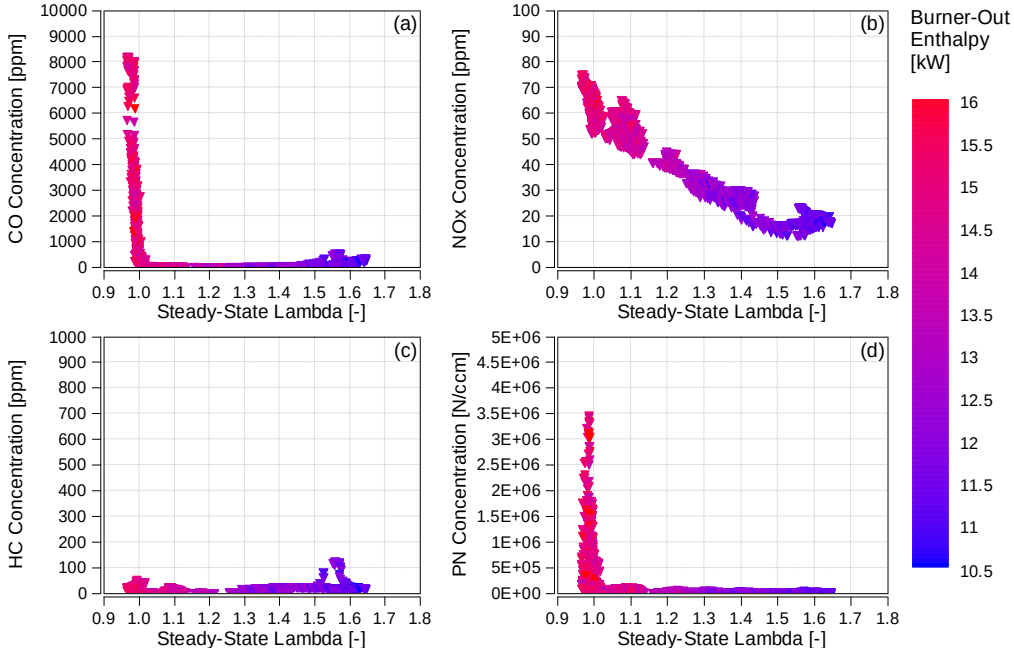

Figure 69 - Trade-off between burner mixture lambda, burner-out pollutant concentrations, (i.e., CO (a), NOx (b), HC (c), and PN (d)), and burner-out thermal power (refer to the color scale) during stabilized firing operation. Measurements refer to ambient temperature of 23°C.

Figure 69 illustrates the trade-off in firing operation at an ambient temperature of 23°C between burner mixture lambda, burner-out pollutant concentrations, and burner-out thermal power. The tested burner displayed a wide

and favorable spectrum of stable firing operation, with a broad range of calibratable lambda values that achieve low emissions (Figure 69.a/c/d), compared to typical engine-out pollutant concentrations. NOx concentration (Figure 69.b), on the other hand, never reached negligible levels during firing operation. Only a decreasing trend was observed with increasing enleanement. This is a consequence of the dilution of the mixture, which also lowers the peak flame temperature, thereby reducing the available thermal power. Combustion instability only arises with lambda values greater than 1.5, as indicated by the worsening of CO and HC emissions. Thermal power scales almost linearly with mixture lambda.

Overall, the most favorable calibration for burner operation is near-stoichiometric with a slight lean bias at startup, and lean (lambda approximately 1.1-1.2) for "steady-state" combustion (firing operation).

The best calibration data set was slightly adapted to lower ambient temperatures; quite similar results were obtained at 23°C and -7°C. This is likely due to the very fast thermal transient of the burner combustion chamber walls combined with adequate fuel-air mixture preparation, avoiding excessive fuel wall wetting.

The -7°C set of experimental data was then used to feed simulation tools to identify where the burner connection (gas-mixing connection) should be optimally placed along the exhaust after-treatment system (methods describes in Par. 2.2.2), and to design the optimized connection for gas mixing between the burner and the after-treatment system (methods described in Par. 2.2.3.1).

3.2.2 Identification of the best layout

An engine cold start in idling at -7°C with a duration of 50 seconds was simulated. The cumulative emissions results were normalized to those of the passive heating strategy (burner disabled). In these calculations, the burner operated for 20 seconds during preheating.

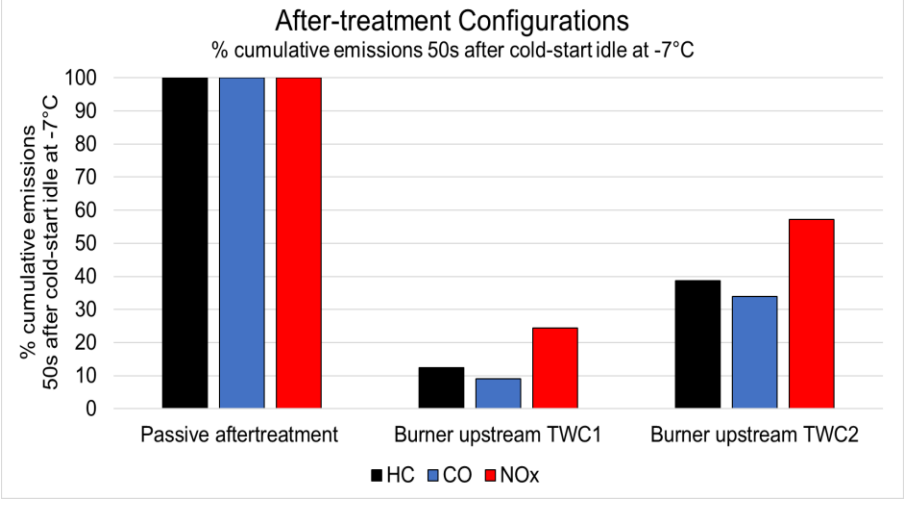

Figure 70 - Comparison of cumulative emissions simulation results after preheating and 50s of engine cold-start idle at -7°C: passive configuration, and with burner used in preheating for 20s in positions upstream TWC1 and upstream TWC2.

Results in Figure 70 show that operating the burner upstream of TWC1 (POS1) is more effective. By examining the CO conversion efficiencies in Figure 71.a/b, the overall system conversion efficiency is higher for the position upstream of TWC1 due to the consistent contribution of TWC1 at engine start.

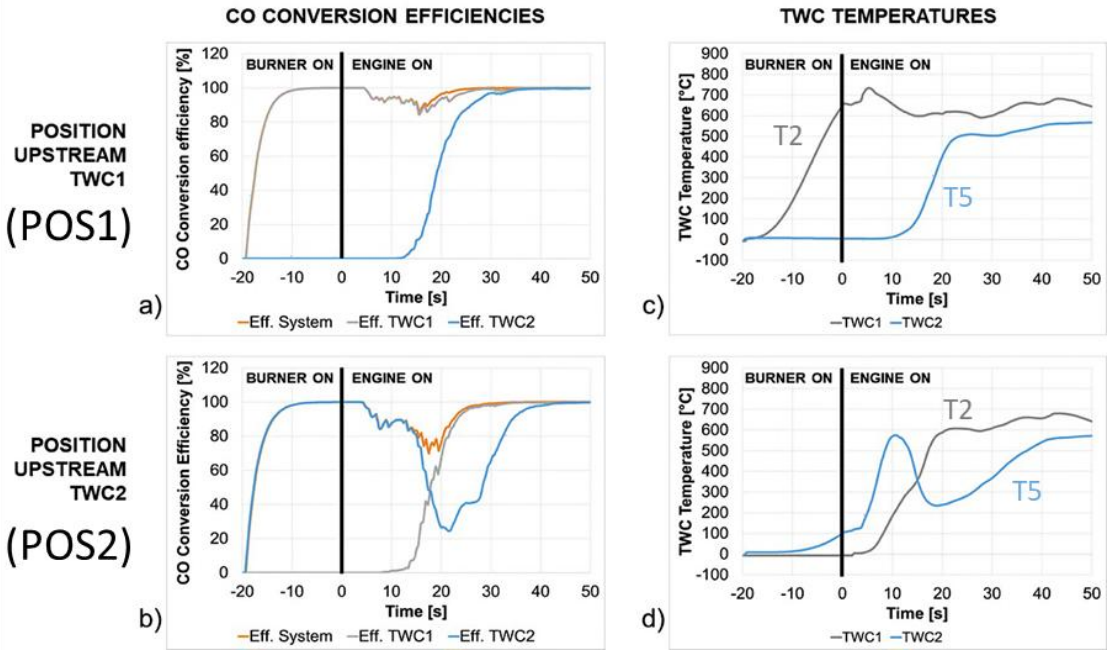

Figure 71 - Simulated CO conversion efficiencies, during burner preheating (20s) and 50s of engine cold-start idle at -7°C, for the whole system, for TWC1, and for TWC2, for configurations POS1 (upstream TWC1) (a) and POS2 (upstream TWC2) (c). Simulated temperatures in TWC1 (T2) and TWC2 (T5) for configurations POS1 (upstream TWC1) (b) and POS2 (upstream TWC2) (d).

These results are directly linked to the temperature of both TWCs during the preheating phase and engine start. In Figure 71.c/d, the wall temperatures of the catalysts T2 and T5 are shown. Focusing on the burner position upstream of TWC1 (Figure 71.c), TWC1 is efficiently heated in the preheating phase. After engine startup, exhaust gases only cause a small drop in temperature, and heat is transferred downstream along the exhaust. When TWC2 reaches light-off, TWC1 is almost 100% efficient.

Conversely, by examining the burner position between TWC1 and TWC2 (Figure 71.d), the preheating phase is less effective due to the higher thermal inertia of TWC2 (larger size and higher specific heat capacity of the ceramic). Right after engine startup, the engine exhaust gas exchanges heat with TWC1, so it reaches TWC2 at a lower temperature, causing the T5 to drop below the light-off threshold. The efficiency of the system is partially compensated by the light-off of TWC1, due solely to the engine exhaust gases. Based on these considerations, the position upstream of TWC1 was selected for experimental tests.

3.2.3 Gas-mixing connection geometry optimization

The gas-mixing connection was optimized through simulation with the goal of maximizing the enthalpic flow (thermal power) from the burner directed to TWC1, while simultaneously achieving the highest possible temperature uniformity. In fact, poor temperature uniformity could lead to cracks in the monolith due to uneven thermal expansion.

Figure 72 displays gas temperature distribution maps, temperature uniformity index, mean gas temperature, and available thermal power at the TWC1 interface for six relevant layouts from the design space. The attempt to increase the temperature at the TWC1 inlet initially led to a decrease in temperature uniformity (configurations b and c). Several iterations were necessary to identify the best solution (f), in terms of mean temperature and uniformity index. The geometry f cannot be showed for confidentiality reasons.

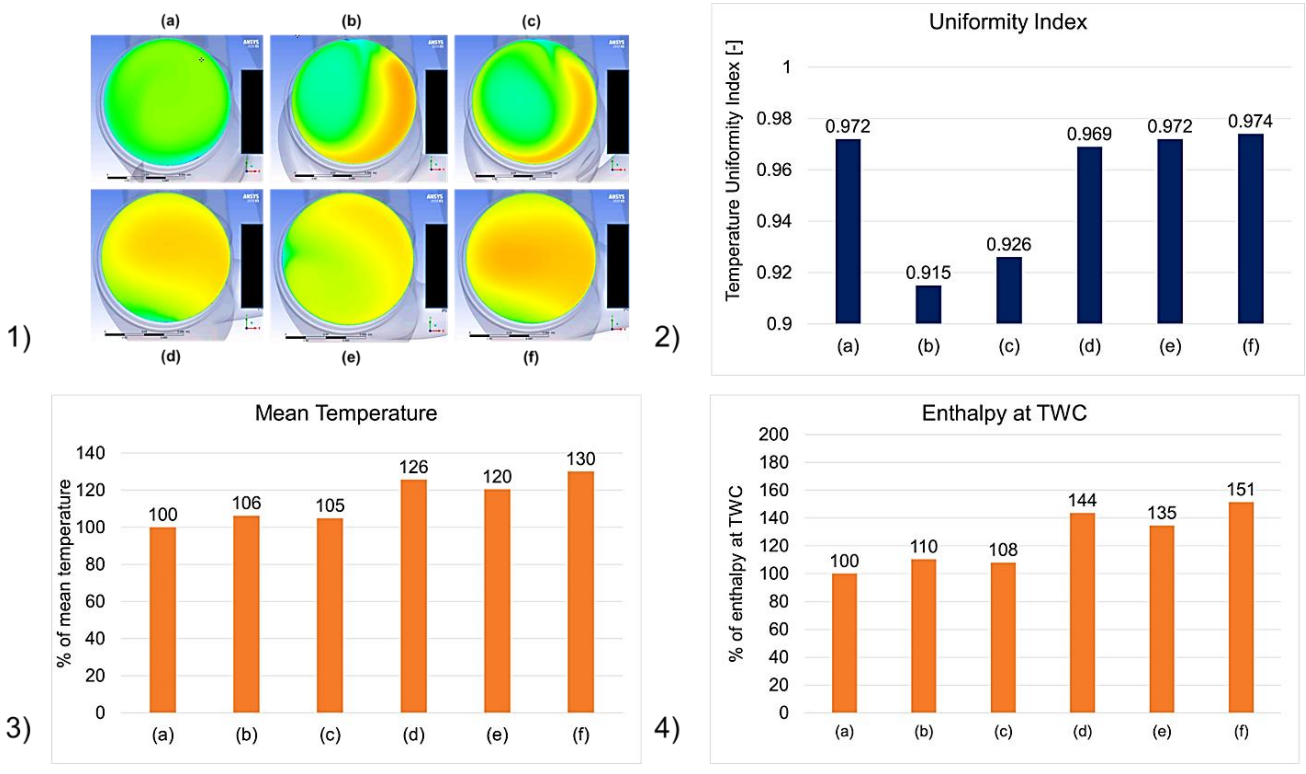

Figure 72 - Evolution of temperature and uniformity index for several designs of the gas-mixing connection (a-f). 1) Temperature contour plot for the tested configurations. Scales are obscured for confidentiality. 2) Temperature uniformity index at the TWC interface. 3) Mean temperature at the TWC interface, normalized to configuration (a) (value [K]). 4) Fluid thermal power at the TWC referred to ambient conditions, normalized to configuration (a).

Figure 73 presents the estimated results in terms of cumulative emissions for configurations (a) and (f). Increasing the gas temperature and thermal power at TWC1 significantly affects system performance.

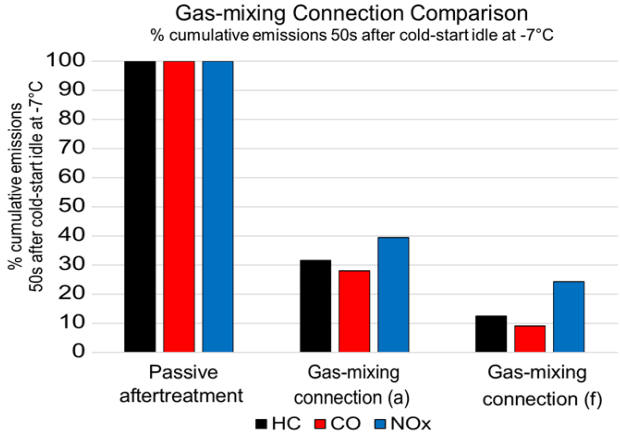

Figure 73 - Simulated cumulative emissions results expected after 20s of burner preheating and 50s of engine cold-start idle at -7°C with gas-mixing connections (a) and (f), compared to passive heating scenario.

Gas-mixing connection candidates (a) and (f) underwent rapid prototyping for testing. The thermal performance of the gas-mixing connection candidates was experimentally assessed. The burner operated under engine firing conditions. The thermal power available at the inlet of TWC1 was compared with the thermal power output at the outlet of the burner to evaluate heat losses. Tests were carried out at ambient temperatures of both 23°C and -7°C, each with its optimized burner calibrations.

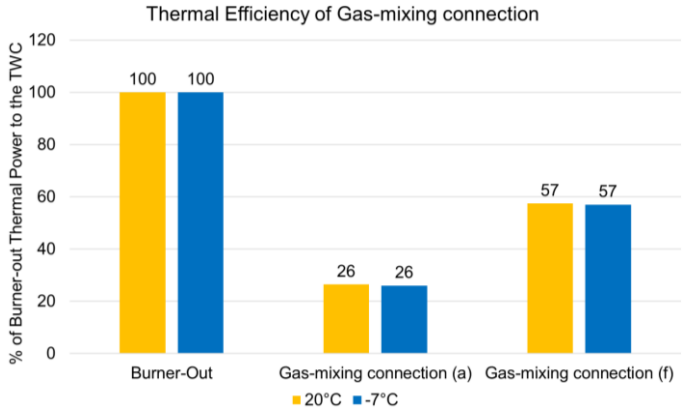

Figure 74 - Measured thermal performance of the burner system (burner, gas-mixing connection, and exhaust manifold) during preheating, evaluated as available thermal power at catalyst inlet location, compared to burner-out thermal power. Gas-mixing connections (a) and (f) are tested. Measurements were performed both at 23°C and -7°C starting temperatures, each with its optimized burner calibration.

Figure 74 shows the results of this test campaign. Gas-mixing connection (a) achieves a thermal efficiency of about 26%, meaning that nearly three-quarters of the thermal power from the burner is dissipated along the pathway to the TWC1 inlet. Gas-mixing connection (f) more than doubles this efficiency, reaching nearly 60%, due to reduced wet surfaces. Furthermore, the outcomes do not depend on the environmental temperature. A low ambient temperature does not significantly worsen heat losses: comparable results are obtained under different ambient conditions (23°C vs. -7°C), indicating that the "sink" temperature has limited influence on the very hot exhaust gases coming from the burner.

These tests confirm that gas-mixing connection (f) performs better than design (a). The overall experimental benefit exceeds what was predicted from CFD calculations. A possible explanation lies in the boundary conditions. In the virtual environment, the wall temperature was maintained constant at -7°C. However, in reality, the metal of the gas-mixing connection heats up during burner combustion, thus reducing the effective gas-to-metal temperature difference that governs heat transfer.

3.2.4 Heating strategy optimization

The numerical approach allowed to evaluate the influence of the preheating duration on pollutant emissions (methods described in Par. 2.2.2). A sensitivity to preheating duration is shown in Figure 75. The cumulated emissions are normalized with respect to passive heating. In order to significantly reduce emissions during engine cold-start idle at -7°C, the preheating time must be sufficiently long to heat a portion of TWC1 above the light-off threshold (the front zone of TWC1).

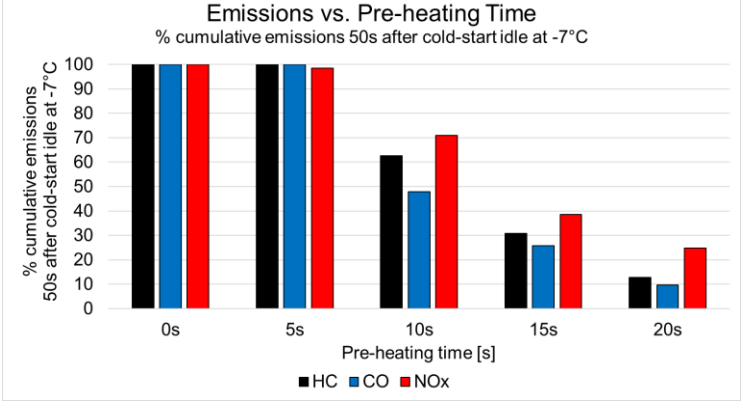

Figure 75 - Simulated cumulative emissions results after burner preheating and 50s of engine cold-start idle at -7°C with different burner preheating times. Cumulative emissions normalized with respect to the passive heating strategy (0 seconds of preheating)

Figure 76 shows the TWC1 temperature profiles (T2) as function of preheating duration. Indeed, with a preheating time of 5 seconds, at the moment of engine startup, T2 remains very low (close to ambient temperature of -7°C). Consequently, the performance of TWC1 is very similar to that observed when the burner is disabled. For longer durations, emissions decrease significantly. However, NOx levels decrease less because the burner emits NOx in non-negligible quantities.

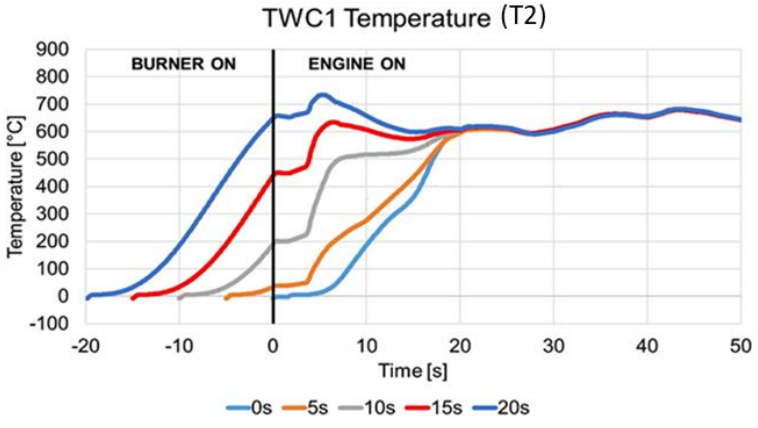

Figure 76 - T2, simulated temperature at 1/4 of the TWC1 length, during burner preheating and 50s of engine cold-start idle at -7°C. Five preheating durations tested: 0s (passive heating), 5s, 10s, 15s, 20s.

Approximately 18 seconds after the engine starts, TWC1 temperatures (T2) converge towards the same value, and the effect of active preheating completely disappears. Variations in burner exhaust gas flow rate were not evaluated because its thermo-fluid dynamic design makes it suitable for operating at a specific flow rate within a fairly narrow tolerance range.

A 3D CFD model was developed in the OpenFOAM environment to replicate the behavior of the FBS during preheating and the subsequent engine cold start in idling. The goal was to analyze the effect of the burner preheating on the TWC1 temperature transient and, consequently, on the TWC1 conversion efficiency. The burner was activated 20 seconds before the engine start. After starting, the engine operated in idling conditions for 30 seconds. The numerical analysis was conducted based on data available from experimental characterizations of the burner and engine outputs. Figure 77 presents the mass flow and gas temperature boundary conditions imposed at the burner outlet and engine exhaust flange.

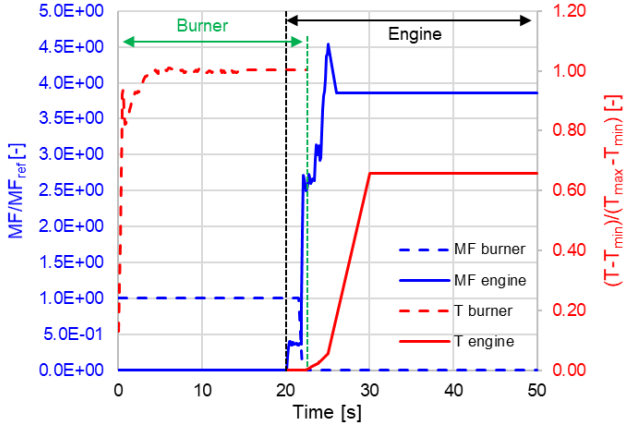

Figure 77 - Boundary conditions concerning gas mass flow rates and temperatures applied at the burner outlet and engine exhaust flange (exhaust manifold inlet). Engine starts at 20 s and the burner is turned off-off at 22.5 s. Data are normalized with respect to reference values.

The temperature of TWC1 during the cold start transient is illustrated in Figure 78, where four different locations along the catalyst axis are considered. During the activation of the burner (time < 20s), the temperature of TWC1 rises at different rates for the various locations. As expected, the temperature transient is quite rapid in the front zone of TWC1, while it is negligible in the rear part.

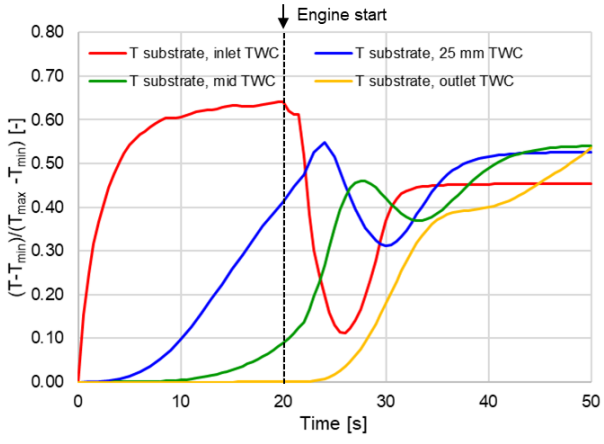

Figure 78 - TWC1 temperature transient in different locations along the catalyst axis: inlet section of the TWC, 25 mm downstream the inlet section, mid-section, outlet section. Data are normalized with respect to reference values.

20 seconds after burner startup, when the burner is turned off and the engine is started, the TWC1 temperature drops due to the cooling effect of the engine's exhaust gas, which is still cold during the cranking phase. Then, a few seconds later, the exhaust gas temperature begins to increase, even though the cooling effects of the cold metallic piping (mainly the exhaust manifold) are still present. The exothermic catalytic reactions occur in the zone where the temperature is above the light-off threshold, contributing to a further increase in temperature. This effect becomes evident after 35 seconds, when the temperature of the substrate in the central part and the second half of the TWC reaches a higher temperature compared to the inlet section.

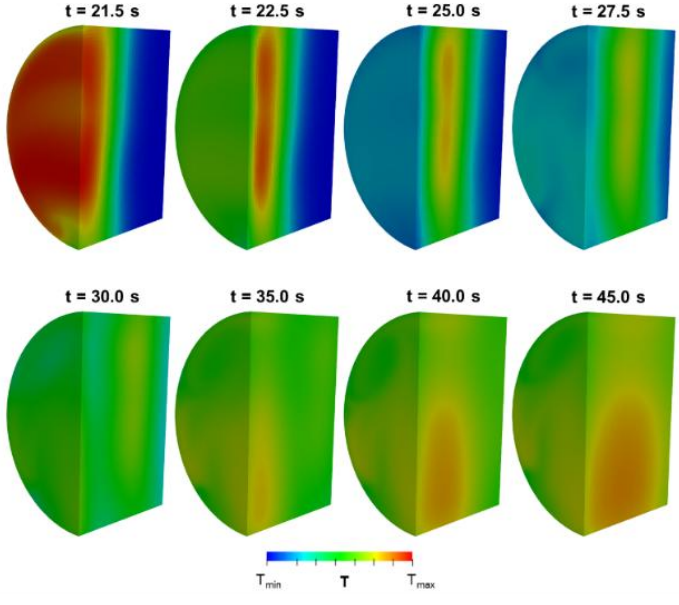

Figure 79 - Evolution of TWC1 temperature in the substrate during the engine's cold start phase at idle.

The evolution of the TWC1 substrate temperature distribution during the engine's cold start is depicted in Figure 79. At 21.5 seconds (upon burner deactivation), the temperature distribution exhibits a maximum temperature at the inlet section of the catalyst. Then, in the time interval from 22.5 to 27.5 seconds, the cold exhaust gas flow causes significant cooling of the substrate. In particular, the cooling effect is more pronounced near the inlet

section, while the highest temperature region progressively moves downstream. For times greater than 30 seconds, the temperature of the exhaust gas begins to increase, and at the same time, exothermic reactions with lower activation energy (e.g., CO oxidation) occur in the zones characterized by the highest temperature. This results in a progressive light-off of the catalyst starting from the central zone of the substrate.

Regarding burner-out emissions (Figure 80), CO and HC are almost negligible and can also be easily converted by TWC1 since the burner operates under slightly lean conditions. NOx emissions are more critical because the emissions from the burner are not negligible, and TWC1 is not extremely effective in reducing them due to the slightly lean air-fuel mixture.

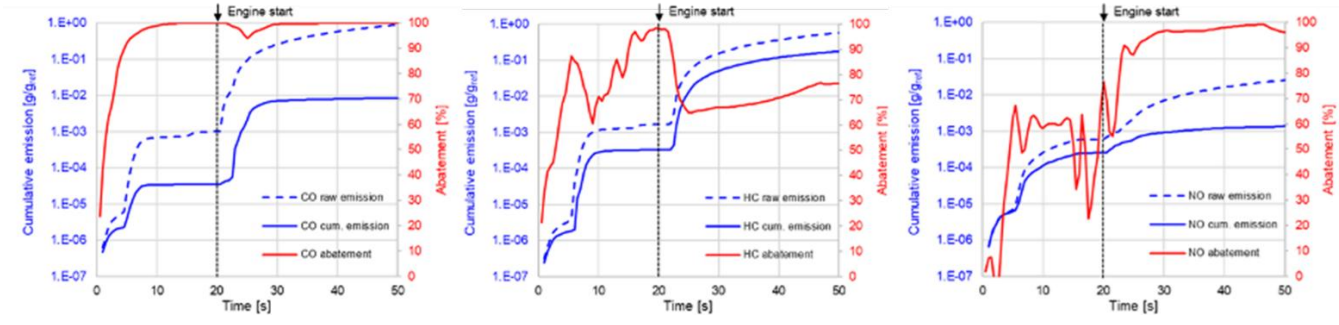

Figure 80 - Cumulative engine-out/raw (dashed blue line) and tailpipe emissions (solid blue line) before and after engine startup at -7°C. TWC1 conversion efficiencies (solid red line). From left to right: CO, HC, and NOx.

Cumulative emissions show a trend that is consistent with the TWC1 temperature evolution described so far. For all pollutants, the most critical phase occurs in the time interval between 20 and 30 seconds (right after engine startup) when the cold exhaust gas cools down the TWC1 substrate. Afterwards (from 30 to 50 seconds), the conversion efficiency of the pollutants rises and remains at high values. After 50 seconds from the burner startup, TWC1 reaches different conversion efficiencies for the various pollutants: CO conversion efficiency is greater than 99%, NOx is around 97%, and HC is around 76%. The lower HC conversion efficiency is due to the higher activation energies required by the catalyzed reactions responsible for HC conversion.

3.2.5 On-engine emission tests

Figure 81 presents the main results. The engine test bench is described in Par. 2.2.4. After the burner startup, all thermocouples in TWC1 register an initial rise followed by a plateau phase, indicating a water phase change. The duration of the plateau increases with the thermocouples positioned deeper along the axis of the catalyst (the shortest at the catalyst inlet and the longest at the catalyst outlet), consistent with the direction of gas flow. After this plateau, temperatures begin to rise further. Figure 81.a illustrates that the burner actively heats only the initial portion of TWC1. A longer preheating time would be necessary to increase the portion of TWC1 that is fully brought above the light-off temperature. Nonetheless, when the engine is fired up (engine startup) after 20 seconds of preheating, the front portion of TWC1 is well beyond the light-off threshold, reaching temperatures that would not be achieved by catalyst heating alone (passive heating). Once the engine is started, the exhaust gas flow lowers the temperature in the initial portion of TWC1 as heat is transferred downstream to the rear zone of TWC1 and to TWC2.

Tailpipe cumulative emissions during preheating are almost negligible except for NOx, which is the only species continuously emitted during "steady state" burner combustion, even with optimized burner calibrations, as shown in Figure 69. In fact, CO and THC tailpipe emissions are significant only during the brief moment of burner startup (approximately a tenth of a second with an optimized startup calibration), resulting in very low cumulative emissions of CO and THC during preheating.

Even though only the front zone of TWC1 is past light-off conditions when the engine starts, tailpipe cumulative emissions after 50 seconds of engine idling are reduced by 92% for CO, 76% for HC, and 46% for NOx, demonstrating the benefit of active heating during engine cold-start idle. Extending the preheating time is

expected to further lower CO and HC emissions, but it could negatively impact NOx emissions, so a proper trade-off must be identified. Burner operation does not affect PN emissions (the difference lies within test-to-test dispersion).

For further details about the FBS development and the obtained results, refer to Rossi et al. [58].

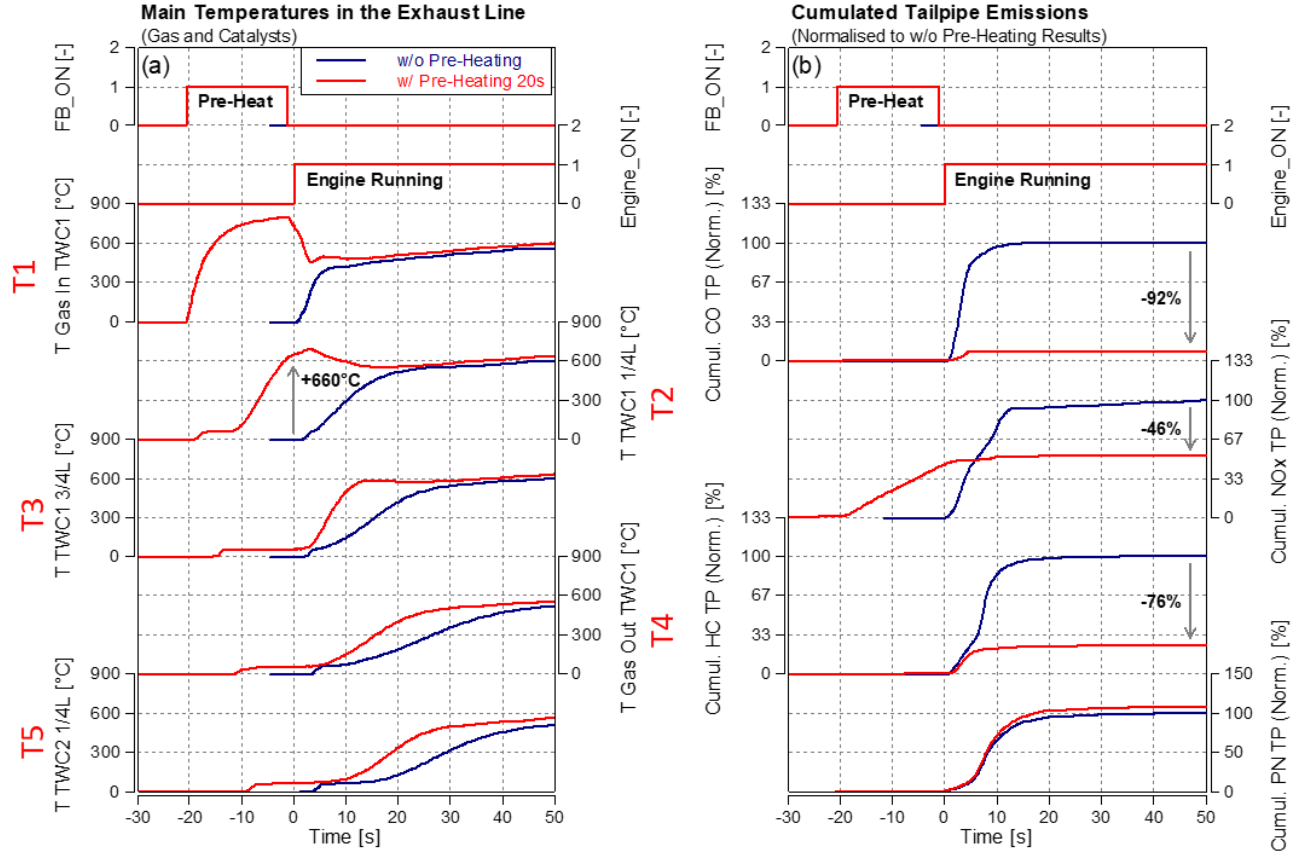

Figure 81 - Experimental results of on-engine tests: burner preheating (20s) followed by 50s of engine cold-start idle at -7°C, compared to baseline without active heating. Graphs show heating performance of TWC1 and TWC2 as measured by thermocouples embedded in the bricks (a), and normalized cumulated tailpipe emissions results (b).

4 Discussion

4.1 Simulation vs Experimental Results

4.1.1 Electrically Heated Catalyst (EHCS)

As already highlighted in the analysis of the experimental results (Par. 3.1.5), the experimental data indicated a reduction in tailpipe cumulative emissions of CO and HC with an increase in the flow rate of secondary air, whereas the simulations suggested the opposite (Figure 82). For short periods of airflow preheating, this inconsistency between calculations and experimental results was minor (refer to Figure 82.a/c for 5 seconds of airflow preheating), while it became significant for longer periods (refer to Figure 82.b/d for 30 seconds of airflow preheating). Before further considerations, it should be clarified that the experimental engine data used as input for the simulation differ from those measured in the experimental tests. In the simulations, the engine data were related to an RDE test, while in the experimental tests, the engine was idling. Therefore, this was not a completely fair comparison (calculated and measured tailpipe emissions cannot be compared each other), but it still highlighted significant differences between the numerical approach and the experimental outcome.

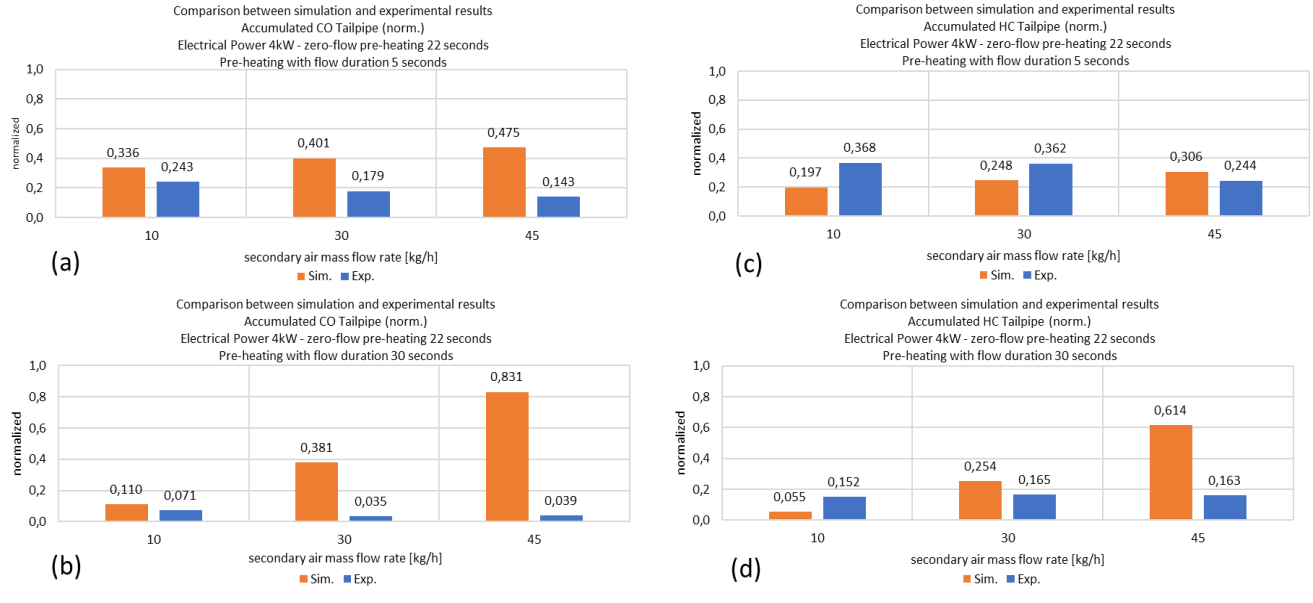

Figure 82 - Comparison between simulation and experimental results, electrical Power 4kW - zero-flow preheating 22 seconds. (a) tailpipe cumulated CO emissions, 5 seconds of airflow preheating, (b) tailpipe cumulated CO emissions, 30 seconds of airflow preheating, (c) tailpipe cumulated HC emissions, 5 seconds of airflow preheating, (d) tailpipe cumulated HC emissions, 30 seconds of airflow preheating.

To understand the origin of this discrepancy, it is useful to compare (Figure 83), for a given heating strategy, the calculated and experimental temperatures of the heater, TWC1 inlet, and TWC1 (T2). The strategy used is the following:

- 22 seconds of zero-flow preheating
- 30 seconds of preheating with an airflow rate of 30 kg/h.
- No postheating.

The simulation (black lines in Figure 83) accurately predicts the temperature transient of the heater in the absence of airflow, confirming the accuracy of the heater's thermal inertia modeling (Figure 83.c). Despite the absence of flow, the inlet temperature (T1) of TWC1 rises significantly, reaching almost 700°C at the activation of the airflow (Figure 83.b). As briefly discussed in Par. 3.1.3, the rise in T1 is caused by the inability to use a null value for the airflow in the 1D CFD model during zero-flow preheating. Airflow rates greater than zero but lower than 0.2 kg/h are permitted by the simulation code but lead to an incorrect estimation of the heater temperature, which remains constant despite the presence of electric heating power. Due to these limitations, setting the flow

to the minimum allowed by the simulation code has a significant impact on the calculated T1. The experimental T1 also rises up to approximately 200°C during the zero-flow preheating, it depends on the radiative heat exchange between the heater and the T1 thermocouple.

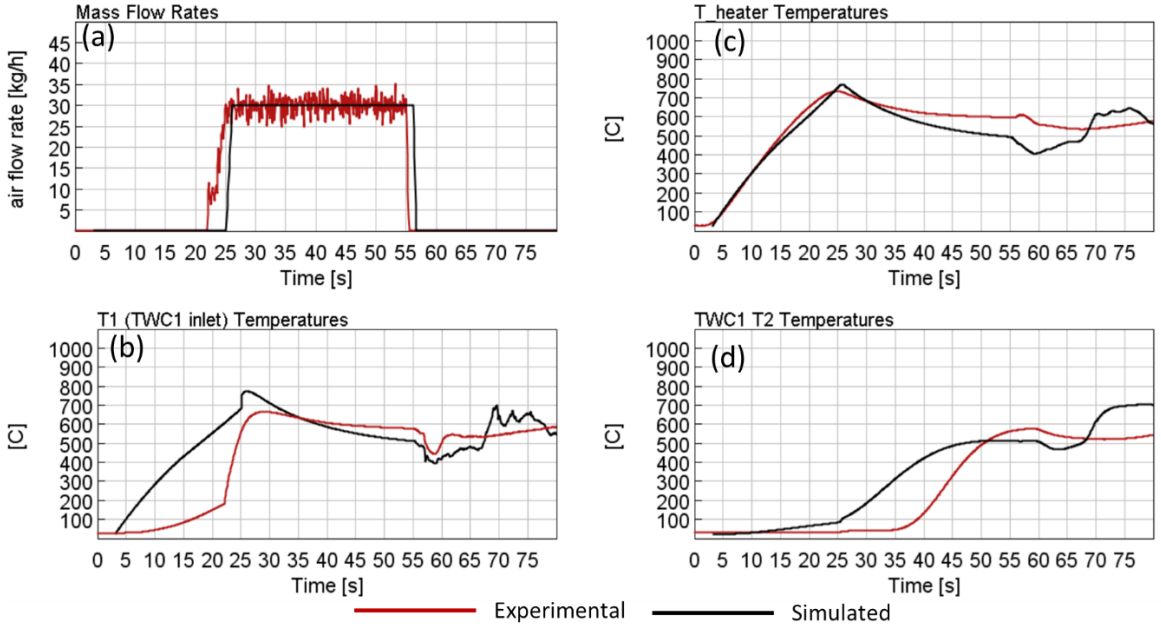

Figure 83 - Comparison of experimental (red lines) and numerical (black lines) cases for a preheating duration with airflow of 30 seconds and 30 kg/h of airflow rates. Zero-flow preheating duration and heating power kept fixed at 22 seconds and 4 kW respectively. (a) airflow rates, (b) T1 temperatures at TWC1 inlet, (c) heater temperatures, (d) TWC1 T2 temperatures.

During airflow preheating, the model tends to overestimate the convective heat exchange between the heater and the airflow. However, the temperatures of the heater (both simulated and experimental) show similar trends and are not significantly different from each other. The maximum difference is approximately 100°C at the end of preheating (Figure 83.c). During the same period, the T1 temperatures, both simulated and experimental, tend to converge towards similar values (Figure 83.b). On the other hand, the simulated and experimental T2 temperatures differ from each other. The simulated T2 temperature initially increases slowly during the zero-flow preheating phase (caused by the non-zero airflow required by the model), and then rises more quickly once the airflow is activated. Conversely, the experimental T2 temperature remains at the ambient level during the zero-flow preheating phase, as expected, and then, after the activation of the airflow, stabilizes at around 45°C for 10 seconds. Afterward, it increases sharply at a rate even higher than that of the calculated T2 (Figure 83.d). This temperature plateau likely indicates the presence of liquid-phase water in the exhaust line, which, when heated by the hot airflow, starts to evaporate. This phase transition occurs at a constant temperature. Once evaporation is complete, the temperature increases again.

Figure 84 shows the comparison between experimental and numerical cases for 30 seconds of airflow preheating at three different airflow rates: 10, 30, and 45 kg/h, respectively (see Figure 82.b/d for the corresponding normalized emissions). In the experimental scenario, for an airflow of 10 kg/h, the heater reaches very high temperatures (slightly above 800°C, see Figure 84.c), but the temperature of TWC1 does not increase due to the temperature plateau of T2 (T2 below 100°C at engine startup, see Figure 84.b). For higher airflow rates (30 and 45 kg/h), the opposite trend is observed; the heater reaches lower temperatures (600°C for 30 kg/h and 400°C for 45 kg/h at engine startup, see Figure 84.c), while TWC1 (T2) temperatures exceed the light-off threshold during preheating (as the T2 plateau is much shorter, Figure 84.b). The heater and TWC1 (T2) temperatures opposite behaviors almost completely balance each other in influencing the tailpipe emissions, the overall effect is a slight reduction of tailpipe cumulative emissions as the airflow rate increases.

In the simulated case, during preheating, for an airflow of 10 kg/h, the heater heats up similarly to the experimental case (Figure 84.c), and TWC1 (T2) also rises above light-off temperatures (Figure 84.b). The combined effect of the low airflow rate on heater and TWC1 temperatures makes these strategies very effective in reducing tailpipe emissions. For higher airflow rates (30 and 45 kg/h), the heater reaches lower temperatures (500°C for 30 kg/h and 370°C for 45 kg/h at engine startup, see Figure 84.c), while TWC1 (T2) temperatures exceed the light-off temperature during preheating (Figure 84.b). Right after engine startup, T2 for 10 kg/h of airflow rises up to 800°C due to the heat exchange between the heater and TWC1, leading to very high emission conversion efficiencies. T2 for 30 kg/h of airflow remains at an almost constant temperature (similar to that of the heater), while for 45 kg/h, T2 decreases, as the heater is at lower temperatures than T2. The result is lower conversion efficiencies as the airflow increases.

In summary, due to inherent limitations of the simulation code - restriction to non-zero flow rate and absence of a water phase transition model - the simulation overestimated the TWC1 temperature (T2) for low airflow rates, leading to an opposite dependence of the tailpipe emissions compared to the experimental case on the airflow rate.

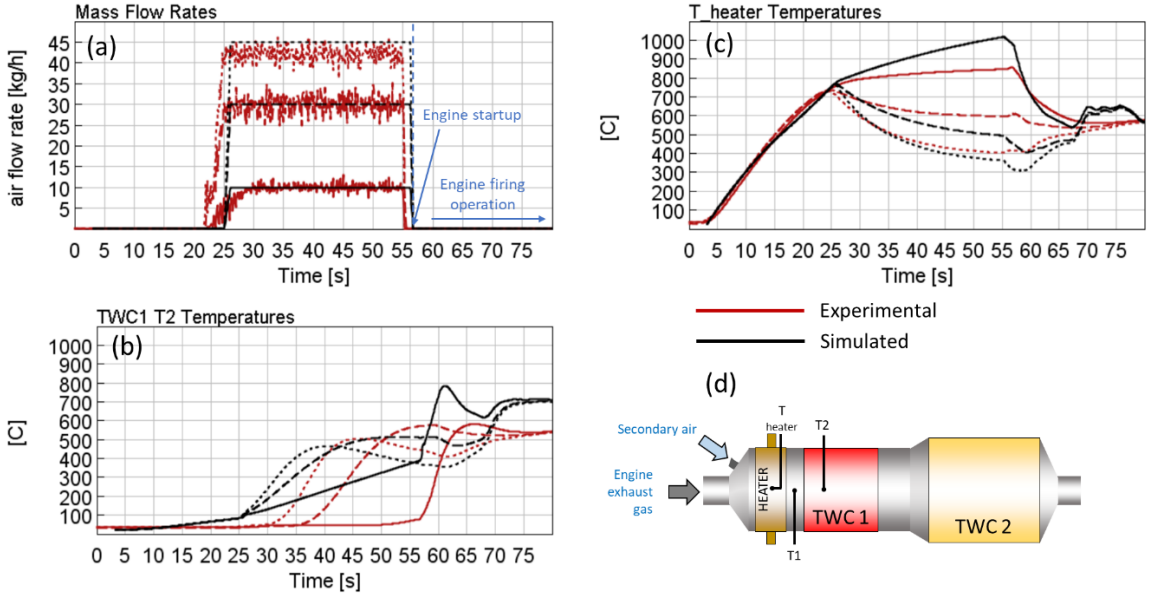

Figure 84 - Comparison of experimental (red lines) and numerical (black lines) cases for a preheating duration with airflow of 30 seconds and three different airflow rates: 10 (solid line), 30 (dashed lines), and 45 kg/h (dotted lines) respectively. Zero-flow preheating duration and heating power kept fixed at 22 seconds and 4 kW respectively. (a) airflow rates, (b) TWC1 T2 temperatures, (c) heater temperatures, (d) Temperature virtual sensors and thermocouples positions.

Experimental results confirmed the effectiveness of the electric catalyst in significantly reducing tailpipe cumulative emissions, despite the prolonged preheating times. This underlines the potential of the Electric Heating Catalyst System (EHCS) to comply with stricter environmental regulations. However, the challenge remains with the extended duration of preheating, which poses practicality issues for daily use. On the other hand, the effectiveness of postheating, though advantageous for eliminating waiting times for consumers, was limited. Therefore, further research is necessary to optimize thermal management strategies, aiming to effectively balance emission reduction and convenience for the end-user.

4.1.2 Fuel Burner System (FBS)

A comparison between the simulation and the experimental results is shown in Figure 85. Qualitatively, the trends of reduction in cumulative emissions were predicted. Quantitatively, comparable results in CO abatement were found. However, an overestimation of the conversion efficiency for both NOx and HC was observed. When comparing 1D CFD simulations to experimental results, it must be acknowledged that many 3D phenomena occur

during engine startup, especially in a naturally aspirated engine, such as uneven flow distribution. These phenomena are difficult to estimate with 1D CFD simulations. Moreover, 1D CFD simulations cannot account for engine-to-engine variability and engine start repeatability. However, the temperature reached by the TWC1 substrate at the end of the 20-second preheating was accurately predicted: the simulation estimated 655°C (as shown in Figure 76) while experimentally, 660°C was recorded (as shown in Figure 81). Overall, the 1D CFD simulation successfully predicted the burner's potential in terms of percentage cumulative reduction. Furthermore, the simulation tool has proven to be crucial during the design phase for defining the most efficient exhaust line layout.

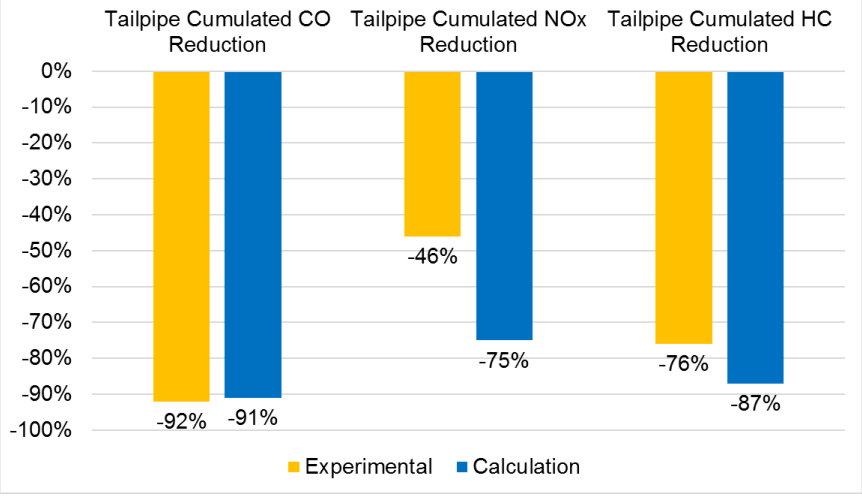

Figure 85 - Comparison between percentage reduction of both simulated and experimental tailpipe cumulated emission of CO, NOx, and HC for burner preheating (20s) followed by 50s of engine cold-start idle at -7°C.

Much work, both computational and experimental, still needs to be done for a complete assessment of the burner. Looking at the experimental cumulative results of NOx (Figure 81), it is evident that most of it originates from the burner itself. Therefore, achieving colder burner combustion (by using a leaner mixture) might offer a significant margin for improvement in NOx emissions at the expense of reduced thermal power output from the burner (as shown in Figure 69.b).

In this work, only preheating was evaluated; the potential for reducing tailpipe emissions by 20-second preheating during a cold start was demonstrated. The acceptance of such prolonged preheating times by drivers before driving is a matter for discussion. Even longer preheating times (not yet investigated) could lead to lower tailpipe cumulative emissions but need to be analyzed from a durability perspective. In fact, exhaust gas temperatures at the burner outlet and at the TWC1 inlet are very close to the maximum temperatures that exhaust piping and after-treatment systems can tolerate. Future research will investigate prolonged (more than 20 seconds) preheating and postheating strategies, implying that the burner operates in conjunction with the engine. A critical aspect of the burner is its robustness against the variability of commercially available fuels, in terms of both startability and burner-generated emissions. The burner must ensure reliability and startability under any environmental condition, necessitating durability tests. NVH (Noise, Vibration, and Harshness) investigations must evaluate the additional noise introduced by the SAP and combustion inside the burner. A thorough analysis of the additional CO2 impact was not performed. The engine catalyst heating strategy remained unchanged. As a preliminary estimate, the additional CO2 introduced by fuel combustion for the analyzed operating strategy is expected to increase CO2 emissions by less than 1% in any emission certification driving cycle.

4.2 Electrically Heated Catalyst System (EHCS) vs Fuel Burner System (FBS)

Emission results from engine cold start measurements at -7°C performed in the climatic test cell are compared in Table 11. The reduction in tailpipe cumulative emissions after preheating followed by 50 seconds of engine

cold-start idle at -7°C is shown. For both systems, EHCS and FBS, the tailpipe emission reduction is calculated in comparison to their respective cases without active heating.

Both technologies demonstrated comparable performance in abating CO emissions during engine cold-start idle at -7°C, aligning with expectations. For both EHCS and FBS, experimental results confirmed that NOx conversion efficiency is lower than that for CO. The lower NOx efficiency could be attributed to the saturation of the actual oxygen storage capacity of the TWCs at engine start after preheating in lean conditions. In fact, during preheating, the airflow (in the case of EHCS) and the slightly lean fuel-air mixture (in the case of FBS) supply the TWCs with oxygen-rich gas. With FBS, a slightly less lean bias in burner combustion calibration could be beneficial, provided it does not negatively impact other species. For both technologies, although HC reduction is significant, it is not as high as predicted. This discrepancy could be attributed to the challenges of replicating complex hydrocarbon behavior in a simulation environment.

Cold-start idle tailpipe cumulative emissions reduction after pre-heating followed by 50s of engine idle at -7°C, against respective cases without active heating (passive heating).					
Technology	**Pre-Heating Duration [s]**	**TWC1 Temperature Improvement (1/4 length) at Engine Start [°C]**	**Tailpipe Cumulated CO Reduction**	**Tailpipe Cumulated NOx Reduction**	**Tailpipe Cumulated HC Reduction**
FBS	20	+660	-92%	-46%	-76%
EHCS	52	+380	-84%	-68%	-52%

Table 11 - FBS and EHCS comparison from on-engine measurements. Tests are 50s of cold-start idle at -7°C after preheating. Preheating duration is also reported. Technologies comparison is expressed as tailpipe cumulated emissions reduction over respective cases without active heating.

Regarding preheating time, as indicated in Table 11, the total preheating duration with EHCS powered at 4kW is more than twice that of FBS. This difference is primarily due to the limited power supplied to the EHCS. Furthermore, FBS achieves a more effective heating of TWC1 compared to EHCS, as inferred from the TWC1 temperature at the end of the preheating phase shown in Table 11, explaining FBS's superior performance in CO and HC conversion.

For a more comprehensive comparison, several preheating durations were simulated for both FBS and EHCS using the same input dataset (engine-out emissions, exhaust gas temperatures and flow rates). The EHCS was evaluated at two different electrical power levels: 4kW and 8kW. The results, presented in Figure 86 in terms of cumulative emissions after preheating and 50 seconds of engine cold-start idle at -7°C, are normalized to the emissions obtained with passive after-treatment and expressed as a percentage.

As mentioned before, the EHCS heater element was placed upstream of TWC1. If not actively heated, it reduces the amount of heat provided to TWC1 during the first phase of engine operation after fire-up. Consequently, light-off is delayed for TWC1, resulting in higher tailpipe emissions.

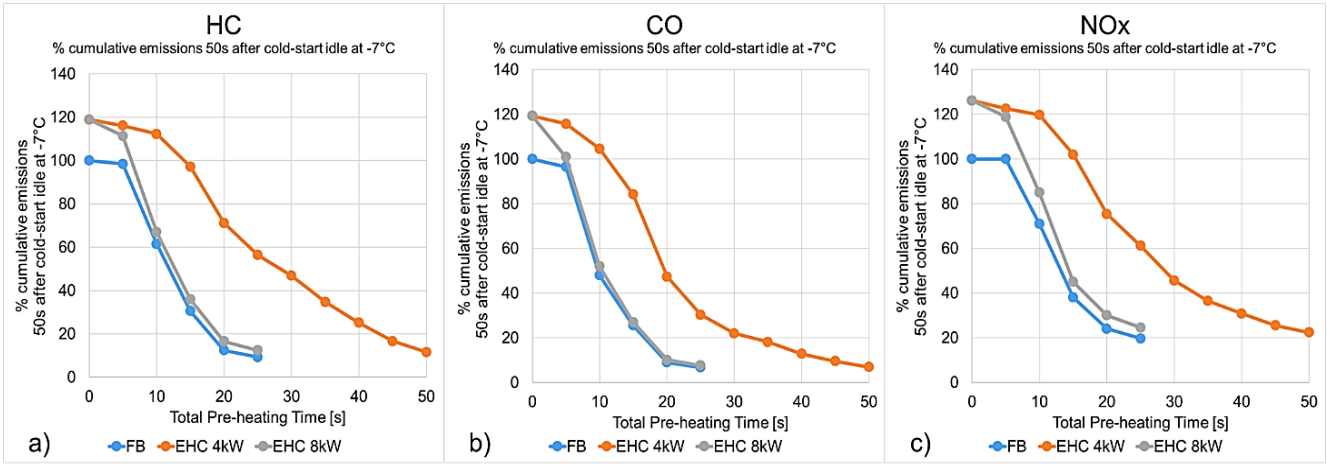

Figure 86: Numerical evaluation of the cumulative emissions for (a) HC, (b) CO and (c) NOx as a function of preheating for FB, EHC 4kW and EHC 8kW, after preheating and 50s of engine cold-start idle at -7°C.

Interestingly, the performance of the EHCS powered with 8 kW is comparable to that of the FBS. However, as previously mentioned, supplying 8 kW at an ambient temperature of -7°C poses a significant challenge, especially if two heater elements are to be powered in a two-bank layout.

An EHCS heater powered with lower electrical power requires a much longer preheating time to achieve the same level of cumulative emissions as the FBS. This longer preheating time is attributable to two main factors:

- The thermal power that the EHCS heater can deliver to TWC1 during the preheating phase is lower than that of the FBS;
- The most effective heating strategy for operating the EHCS involves an initial phase where electrical power is used to increase the temperature of the heater substrate. This phase is part of the preheating process (zero-flow preheating), but little thermal power is transferred to TWC1 through radiation, which is insufficient to raise the temperature within the TWC1 substrate significantly. The subsequent preheating phase, with SAP mass flow, is the effective one, actively transferring thermal power to TWC1.

5 Conclusions

Simulations and experimental results have shown that both EHCS and FBS are promising active-heating technologies that significantly reduce tailpipe cumulative gaseous emissions during engine cold-start, provided that a sufficiently long preheating time is guaranteed. A long preheating duration is hardly accepted by customers, and in the case of EHCS, it also implies high amounts of energy and power from the onboard network.

For the considered after-treatment layout, numerical investigations have demonstrated that both EHCS and FBS are most effective in reducing cumulative emissions when located upstream of the front catalyst TWC1. When comparing EHCS and FBS, the following considerations can be summarized:

- The implementation of FBS in the ATS requires a gas-mixing connection, whose design significantly impacts the thermal power provided to TWC1 and, consequently, the system's performance.
- The thermal power provided to the exhaust line by EHCS depends on the available electrical power and energy, which could be limited by both the vehicle's onboard network and heater design constraints.
- FBS thermal power, net of heat losses, is used directly to heat the TWCs, while EHCS electrical power first heats the heater and then, through radiative and convective heat transfer, the TWCs. This process, at the core of the EHCS's operating principle, leads to longer preheating times based on the electrical power available.
- FBS is not as effective in reducing NOx compared to CO and HC. Indeed, the burner itself produces non-negligible amounts of NOx emissions, which must be strictly controlled.
- Simulations showed that EHCS powered with 8kW and FBS have comparable preheating times for the same emissions reduction. However, supplying 8kW at an ambient temperature of -7°C is a challenging task, especially if two heater elements need to be powered in a two-bank layout.
- The lower the electrical power provided to EHCS, the higher the preheating times required to reach the same cumulative emissions level.
- A potential disadvantage of EHCS compared to FBS is the number of activations in preheating without recharging the vehicle battery. In fact, it could be limited by the energy available, depending on the vehicle's onboard network design. The quantity of fuel needed to use FBS is negligible, the number of activations is virtually unlimited.
- A critical aspect for FBS technology is its robustness against the variability of commercially available fuels, both in terms of startability and burner-generated emissions.
- Another concern for both technologies is that additional noise is generated during preheating, which could be unpleasant for the driver. In both layouts, while the engine is not running, an SAP is activated, and with FBS, combustion also occurs. This requires dedicated NVH investigations and potential countermeasures.
- A long preheating time before driving, crucial for the effectiveness of these technologies, could hardly be accepted by customers.

Post-heating strategies, meaning that active heating devices are operated together with the engine after engine startup, were investigated only for EHCS. It's necessary for the future to investigate these strategies for FBS as well. FBS postheating presents more challenges compared to EHCS, related to both fluid dynamics and burner controllability. Fluid dynamic interferences due to simultaneous engine operation could affect the stability of the burner combustion and the reading of lambda sensors used for controlling both the burner and the engine. Despite these challenges, postheating strategies could result in higher after-treatment performance. Moreover, for the same cumulative emissions level, a potential improvement due to postheating could be invested in reducing preheating time.

Another possible outcome of this work would be the investigation, both numerical and experimental, of a coated heater. A catalytic coating on the heater substrate could improve performance in light-off, despite introducing higher thermal inertia.

Finally, further experimental tests are required to deepen the assessment of FBS and EHCS technologies. For example, on-vehicle tests, such as driving cycles, need to be performed. In addition, both technologies still need to be proven effective under variable ambient conditions (not only temperature but also altitude), reliable over time, mileage, and use, throughout the entire life of the vehicle. Lastly, part-to-part dispersion between component samples also needs to be investigated.

From the methodological point of view, a novel 3D CFD numerical approach developed by Della Torre et al. [44-47], dedicated to the analysis of ICEs exhaust after-treatment systems, was applied to analyze EHCS and FBS performances. A comprehensive electrical heating modeling was implemented. The employed formulation is general; it can be applied to any heater geometry. A dedicated radiative coupling methodology was introduced to address the radiative heat transfer.

The comparison between the 1D CFD simulation results and the experimental tests of the EHCS has highlighted the current limits of the implemented simulation methodology. The integration in the simulation environment of a water phase transition model represents a software development that will be actively pursued in the future to improve the predictiveness of the simulations.

6 Abbreviations

ATS – After Treatment System

CFD - Computational Fluid Dynamics

CHT – Conjugate Heat Transfer

CO – Carbon Monoxide

CO2 – Carbon Dioxide

CPSI - Cell Per Square Inch

DOE – Design of Experiment

DOC – Diesel Oxidation Catalyst

DPF – Diesel Particulate Filter

ECU - Engine Control Unit

EGR – Exhaust Gas Recirculation

EHC – Electrically Heated Catalyst

EHCS - Electrically Heated Catalyst System

FBS - Fuel Burner System

FTIR - Fourier Transform Infrared

FTP – Federal test Procedure

GPF - Gasoline Particulate Filter

GSA – Geometric Surface Area

HC - Hydrocarbons

HCU - Heater Control Unit

LNT – Lean NOx Trap

MCT – Mercury-Cadmium-Telluride

NOx – Nitrogen Oxides

NO – Nitric Oxide

NO2 – Nitrogen Dioxide

OSC – Oxygen Storage Capacity

PC - Particle Counter

PGM – Platinum Group Metal

PNC – Particle Number Counter

PND – Particle Number Diluter

RDE – Real Driving Emissions

SAP - Secondary Air Pump

SCR - Selective Catalyst Reduction

SOC – State of Charge

SI-ICE – Spark-Ignition Internal Combustion Engine

THC - Total Hydrocarbon

TWC - Three Way Catalyst

VPR – Volatile Particle Remover

7 Bibliography

[1] Giechaskiel, B.; Joshi, A.; Ntziachristos, L.; Dilara, P. European Regulatory Framework and Particulate Matter Emissions of Gasoline Light-Duty Vehicles: A Review. Catalysts 2019, 9, 586.

[2] Awad, O. I.; Ma, X.; Kamil, M.; Ali, O. M.; Zhang, Z.; Shuai, S. Particulate emissions from gasoline direct injection engines: A review of how current emission regulations are being met by automobile manufacturers. Sci. Total Environ. 2020, 718, 137302.

[3] Demuynck, J.; Favre, C.; Bosteels, D.; Hamje, H.; Andersson, J. Real-World Emissions Measurements of a Gasoline Direct Injection Vehicle without and with a Gasoline Particulate Filter. SAE Technical Paper 2017, 2017−01−0985.

[4] The role of ceria-based nanostructured materials in energy applications M. Melchionna and P. Fornasiero Department of Chemical and Pharmaceutical Sciences, INSTM, ICCOM-CNR, University of Trieste, Via L. Giorgieri1, 34127 Trieste, Italy.

[5] Balenovic, M., Edwards, J., & Backx, T. (2006). Vehicle Application of Model-Based Catalyst Control. Control Engineering Practice, 223-233.

[6] Gandhi, H., Graham, G., & McCabe, R. (2003). Automotive Exhaust Catalysis. *Journal of Catalysis,* 433-442.

[7] Heimrich, M. J. (1990). Air Injection to an Electrically-Heated Catalyst for Reducing Cold-Start Benzene Emissions from Gasoline Vehicles. International Fuels and Lubricants Meeting and Exposition. Tulsa: SAE International.

[8] Chen, H.-Y., Chang, H.-L. (Russell) “Development of Low Temperature Three-Way Catalysts for Future Fuel-Efficient Vehicles,” Johnson Matthey Technol. Rev., 2015, 59, (1), 64-67, doi: 10.1595/205651315X686011

[9] Giechaskiel, B.; Lähde, T.; Drossinos, Y. Regulating particle number measurements from the tailpipe of light-duty vehicles: The next step? Environ. Res. 2019, 172, 1−9.

[10] Andrew Bean Getsoian & Joseph R. Theis & Christine K. Lambert “Sensitivity of Three-Way Catalyst Light-Off Temperature to Air-Fuel Ratio” Ford Motor Company, under exclusive license to Springer International Publishing AG, part of Springer Nature 2018

[11] Robert J. Farrauto, Michel Deeba and Saeed Alerasool, “Gasoline automobile catalysis and its historical journey to cleaner air”, doi:10.1038/s41929-019-0312-9

[12] Recent advances in gasoline three-way catalyst formulation: A review. Shawn Rood, Salvador Eslava, Alexis Manigrasso and Chris Bannister. Proc IMechE Part D: J Automobile Engineering 2020, Vol. 234(4) 936–949.

[13] Shelef M. and McCabe RW. Twenty-five years after introduction of automotive catalysts: what next? Catal. Today 2000; 62: 35–50.

[14] Nakanishi, Y., Suehiro, Y., Hashimoto, M., Narishige, T. et al., “Development of Low Temperature Active Three-Way Catalyst,” SAE Technical Paper 2019-01-1293, 2019, doi:10.4271/2019-01-1293.

[15] Sung Bong Kang, Seok Jun Han, Sung Bang Nama, In-Sik Nama, Byong K. Cho, Chang Hwan Kim, Se H. Oh - Activity function describing the effect of Pd loading on the catalytic performance of modern commercial TWC Chemical Engineering Journal 207–208 (2012) 117–121.

[16] Towards dense single-atom catalysts for future automotive applications (2020) A. Beniya and S. Higashi, Toyota Central R&D Laboratories, doi: 10.1038/s41929-019-0282-y.

[17] Benefits of Pd Doped Zeolites for Cold Start HC/NOX Emission Reductions for Gasoline and E85 Fueled Vehicles (2018), Xu, L. et al.

[18] Moser, D.H., Nunan, J., Alltizer, C., Nipunage, S. et al., “Durability of an UF HC Trap/SCR Catalyst System Applied to a 4-Cylinder PZEV Calibrated Vehicle,” SAE Technical Paper 2018-01-0336, 2018, doi:10.4271/2018-01-0336.

[19] Lupescu, J., Xu, L., Jen, H., Harwell, A. et al. “A New Catalyzed HC Trap Technology that Enhances the Conversion of Gasoline Fuel Cold-Start Emissions,” SAE Int. J. Fuels Lubr. 11(4):411-425, 2018, doi:10.4271/2018-01-0938.

[20] Keifer, W., Plodek, B., Ehmann, P., Felwisch-Drentrup, R., & Diringer, J. (1998, November). BMW 750i with Electrically Heated Catalytic Converter. MTZ Worldwide.

[21] Hanel, F., Otto, E., and Brück, R., “Electrically Heated Catalytic Converter (EHC) in the BMW ALPINA B12 5.7 Switch-Tronic,” SAE Technical Paper 960349, 1996, doi: 10.4271/960349.[46].

[22] Hanel, F., Otto, E., Brück, R., Nagel, T. et al., “Practical Experience with the EHC System in the BMW ALPINA B12,” SAE Technical Paper 970263, 1997, doi: 10.4271/970263.

[23] Manuel Presti and Lorenzo Pace, EMITEC G.m.b.H., Luca Poggio and Vincenzo Rossi Ferrari Auto Spa “Cold Start Thermal Management with Electrically Heated Catalyst: A Way to Lower Fuel Consumption”. SAE 2013-24-0158.

[24] Jean, E. and Goncalves, M., “Electrically Heated Catalyst: A Powerful Tool for Aftertreatment Optimization” SAE Technical Paper 2023-01-0351, 2023, doi:10.4271/2023-01-0351

[25] Leahey, N., Crawford, R., Douglas, J., and Bauman, J., "Induction Heating of Catalytic Converter Systems and its Effect on Diesel Exhaust Emissions during Cold Start" SAE Technical Paper 2018-01-0327, 2018, doi: 10.4271/2018-01-0327.

[26] Socha L., Thompson F., Weber P., “Optimization of Extruded Electrically Heated Catalysts” SAE Technical Paper 940468, 1994, doi: 10.4271/940468.

[27] Meruva P., Matheaus A., Sharp C., McCarthy J., Collins T., and Joshi A., “Meeting future NOx emissions using electric heater in an advanced aftertreatment system” Frontiers in Mechanical Engineering, 2022, doi:10.3389/fmech.2022.979771.

[28] Boger T., Rose D., He S., Joshi A., “Developments for future regulations and path to zero impact emissions – A catalyst substrate and filter supplier’s perspective”, Transportation Engineering, 2022, doi: 10.1016/j.treng.2022.100129.

[29] Sadamitsu, T., Oki, T., Korenaga, S., Hirooka, S. et al., "Development of a Ceramic EHC," SAE Int. J. Adv. & Curr. Prac. in Mobility 5(1):141-147, 2023, https://doi.org/10.4271/2022-01-0536.

[30] Socha, L. S., & Thompson, D. F. (1992). “Electrically Heated Extruded Metal Converters for Low Emissions Vehicles”. International Congress & Exposition. SAE Technical Paper 920093.

[31] Breuer, J., Hirth, P., Bruck, R., & Kruse, C. (1996). Electrically Heated Catalyst for Future USA and European Legislation. SAE International Congress and Exposition. Detroit: SAE International.

[32] Kubsh, J. E. (1994). Alternative EHC Heating Patterns and Their Impact on Cold-Start Emissions Performance. *Fuels & Lubricants Meeting & Exposition.* Baltimore: SAE International.

[33] Laurell, M., Pace, L., Ekström, F., and Konieczny, K., “Strive for Zero Emissions Impact from Hybrids,” SAE Technical Paper 2019-24-0146, 2019, doi:10.4271/2019-24-0146.

[34] Hepburn, J., Adamczyk, A., and Pawlowicz, R., “Gasoline Burner for Rapid Catalyst Light-Off,” SAE Technical Paper 942072 (1994). https://doi.org/10.4271/942072.

[35] Polat Öser and Eckart Mueller Volkswagen A.G., Günter R. Härtel and Armin O. Schürfeld Pierburg GmbH "Novel Emission Technologies with Emphasis on Catalyst Cold Start Improvements Status Report on VW-Pierburg Burner/Catalyst Systems" SAE: 940474.

[36] Zu Schweinsberg, A., Klenk, M., and Degen, A., "Engine-Independent Exhaust Gas Aftertreatment Using a Burner Heated Catalyst," SAE Technical Paper 2006-01-3401 (2006). doi.org: 10.4271/2006-01-3401.

[37] Dr.-Ing. Thomas Pauer, Dipl.-Ing. Heiko Weller, Dr.-Ing. Erik Schünemann, Dr.-Ing. Jochen Walther, Dipl.-Ing. Armin Hassdenteufel, Dr.-Ing. Vinzenz Neubert Robert Bosch GmbH, Powertrain Solutions Division, Stuttgart, Germany A gasoline powertrain with negligible influence on air quality. 39th Wiener Symposium.

[38] Koci, P., Schejbal, M., Trdlicka, J., Gregor, T., Kubicek, M., Marek, M., "Transient behaviour of catalytic monolith with NOx storage capacity". Catalysis Today, 2006.

[39] Hofstetter, J., Boucharel, P., Atzler, F., and Wachtmeister, G., "Fuel Consumption and Emission Reduction for Hybrid Electric Vehicles with Electrically Heated Catalyst," SAE Int. J. Advances & Curr. Prac. in Mobility 3(1):702-714, 2021, doi:10.4271/2020-37-0017.

[40] Sivakumar, S., Shingyouchi, H., Yan, X., Okajima, T. et al., "Effects of Using an Electrically Heated Catalyst on the State of Charge of the Battery Pack for Series Hybrid Electric Vehicles at Cold Start," SAE Technical Paper 2020-01-0444, 2020, doi:10.4271/2020-01-0444.

[41] Postrioti, L., Battistoni, M., Zembi, J., Brizi, G. et al., "Experimental and Numerical Analysis of a Swirled Fuel Atomizer for an Aftertreatment Diesel Burner," SAE Technical Paper 2023-24-0106, 2023, doi:10.4271/2023-24-0106.

[42] Battistoni, M., Zembi, J., Casadei, D., Ricci, F. et al., "Burner Development for Light-Off Speed-Up of Aftertreatment Systems in Gasoline SI engines," SAE Technical Paper 2022-37-0033, 2022, doi:10.4271/2022-37-0033.

[43] Harris, T., Bellard, R., Muhleck, M., and Palmer, G., "Pre-Heating the Aftertreatment System with a Burner," SAE Technical Paper 2022-01-0554, 2022, doi:10.4271/2022-01-0554.

[44] Della Torre, A., Montenegro, G., Onorati, A., and Cerri, T., "CFD Investigation of the Impact of Electrical Heating on the Light-off of a Diesel Oxidation Catalyst," SAE Technical Paper 2018-01-0961 (2018). https://doi.org/10.4271/2018-01-0961.

[45] Della Torre, A., Barillari, L., Montenegro, G., Onorati, A. et al., "Numerical Assessment of an After-Treatment System Equipped with a Burner to Speed-Up the Light-Off during Engine Cold Start," SAE Technical Paper 2021-24-0089, 2021, doi:10.4271/2021-24-0089.

[46] Della Torre, A., Montenegro, G., Onorati, A., Cerri, T. et al., "Numerical Optimization of a SCR System Based on the Injection of Pure Gaseous Ammonia for the NOx Reduction in Light-Duty Diesel Engines," SAE Technical Paper 2020-01-0356 (2020). https://doi.org/10.4271/2020-01-0356.

[47] Della Torre, A., Montenegro, G., Onorati, A., and Cerri, T., "CFD Investigation of the Impact of Electrical Heating on the Light-off of a Diesel Oxidation Catalyst." SAE Technical Paper 2018-01-0961, 2018, doi:10.4271/2018-01-0961.

[48] Samaras, Z., Kontses, A., Dimaratos, A., Kontses, D. et al., "A European Regulatory Perspective towards a Euro 7 Proposal." SAE Technical Paper 2022-37-0032, 2022, https:// doi.org/10.4271/2022-37-0032.

[49] Bauer, H., Haldenwanger, H.G., Hirth, P., Bruck, R., "Thermal Management of Close Couples Catalyst". SAE Technical Paper 1999-01-1231.

[50] Ramanathan, K. and Shekhar, C., "Kinetic Parameters Estimation for Three Way Catalyst Modeling," Industrial & Engineering Chemistry Research 50, no. 17 (2011): 9960-9979, doi:10.1021/ie200726j.

[51] Horiba, MEXA 7170 User Guide.

[52] Koltsakis, G., Konstantinidis, P., and Stamatelos, A. “Development and application range of mathematical models for 3-way catalytic converters,” Appl. Catal. B.: Environmental, 12:161-191, 1997.

[53] AVL eStorage LV 20kW, 32kW 05/2015 AT6091, REV. 01.

[54] AVL SESAM i60 FT SII User’s Manual, November 209 AT6401E, REV. 10.

[55] AVL APC Plus Product Guide, AT2858E Rev. 13 - 06/2017.

[56] JULABO PRESTO W50, Operating Manual, 1.953.3041-V11 07/18.

[57] A. Della Torre, G. Montenegro, A. Onorati, S. Paltrinieri, F. Rulli, and V. Rossi. Calibration of the Oxygen Storage Reactions for the Modeling of an Automotive Three-Way Catalyst. Ind. Eng. Chem. Res. 2021, 60, 6653−6661

[58] Rossi, V., Brocchi, L., Medda, M., Paltrinieri, S. et al., “Design and Assessment of an Exhaust After-Treatment System Equipped with a Fuel Burner for High-Performance Engines,” SAE Technical Paper 2023-01-0355, 2023, doi:10.4271/2023-01-0355.

[59] “Worldwide Emission Standards and Related Regulations Passenger Cars / Light and Medium Duty Vehicles”, Continental, May 2019

8 Appendix

8.1 Heating strategy optimization

8.1.1 DOE at ambient temperature of 23°C

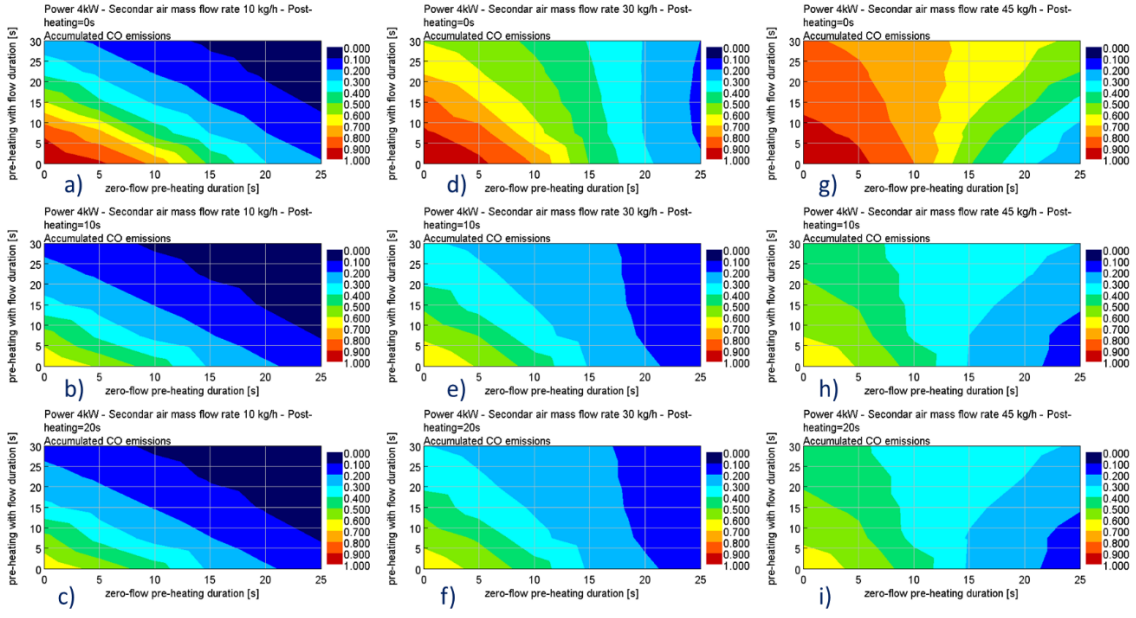

Figure 87 - DOE results at ambient temperature of 23°C: CO cumulative emissions 50 seconds after engine startup for respectively 0, 10, and 20 seconds of postheating, as a function of zero-flow preheating and airflow preheating durations. (a, b, c) airflow rate 10 kg/h, post heating of 0, 10, and 20 seconds, respectively. (d, e, f) airflow rate 30 kg/h, post heating of 0, 10, and 20 seconds, respectively. (g, h, i) airflow rate 45 kg/h, post heating of 0, 10, and 20 seconds, respectively. Accumulated emissions are normalized with respect to the passive heating results 50 seconds after engine startup.

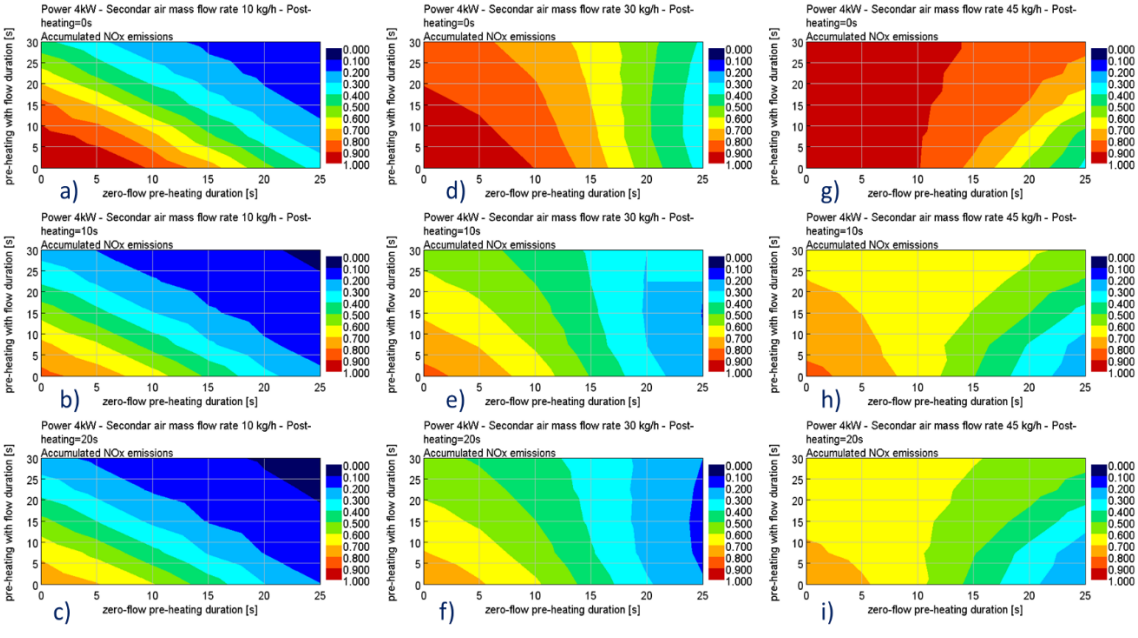

Figure 88 - DOE results at ambient temperature of 23°C: HC cumulative emissions 50 seconds after engine startup for respectively 0, 10, and 20 seconds of postheating, as a function of zero-flow preheating and airflow preheating durations. (a, b, c) airflow rate 10 kg/h, post heating of 0, 10, and 20 seconds, respectively. (d, e, f) airflow rate 30 kg/h, post heating of 0, 10, and 20 seconds, respectively. (g, h, i) airflow rate 45 kg/h, post heating of 0, 10, and 20 seconds, respectively. Accumulated emissions are normalized with respect to the passive heating results 50 seconds after engine startup.

8.1.2 DOE at ambient temperature of -7°C

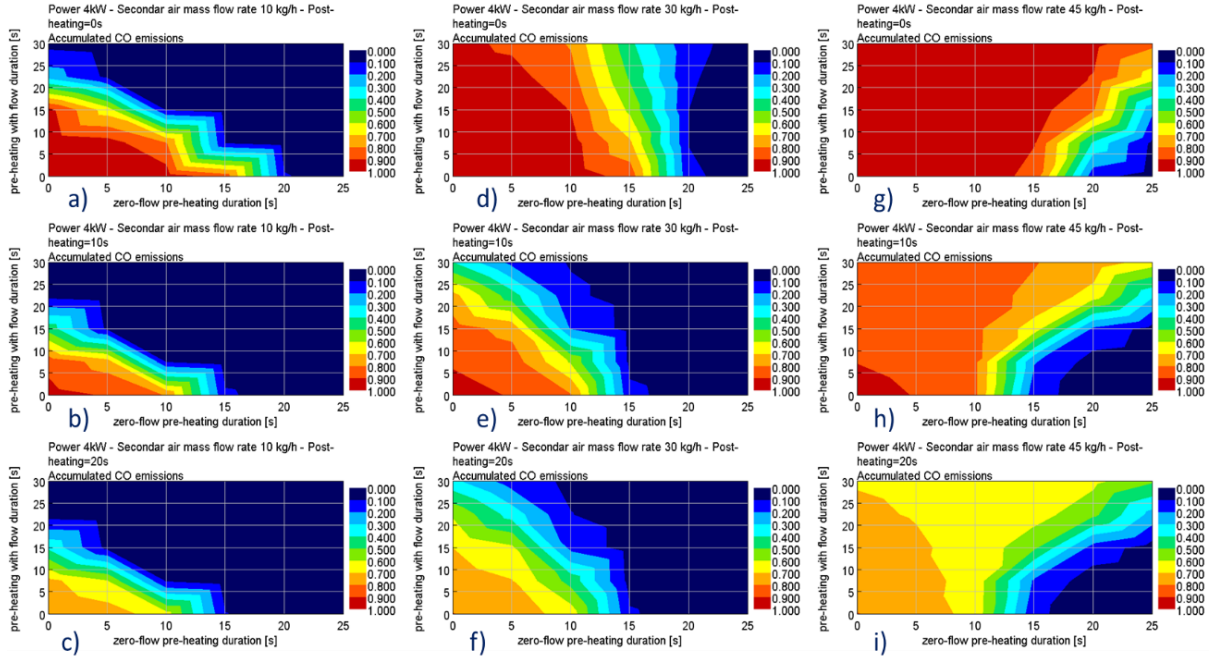

Figure 89 – DOE results at ambient temperature of -7°C: CO cumulative emissions 50 seconds after engine startup for respectively 0, 10, and 20 seconds of postheating, as a function of zero-flow preheating and airflow preheating durations. (a, b, c) airflow rate 10 kg/h, post heating of 0, 10, and 20 seconds, respectively. (d, e, f) airflow rate 30 kg/h, post heating of 0, 10, and 20 seconds, respectively. (g, h, i) airflow rate 45 kg/h, post heating of 0, 10, and 20 seconds, respectively. Accumulated emissions are normalized with respect to the passive heating results 50 seconds after engine startup.

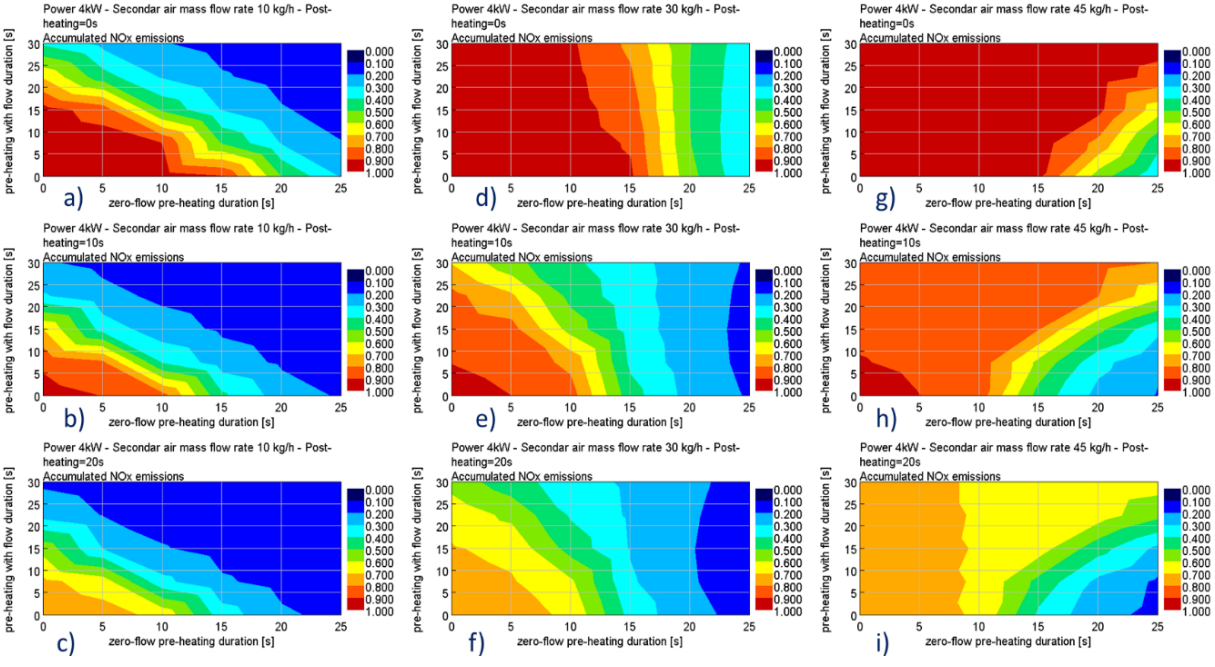

Figure 90 – DOE results at ambient temperature of -7°C: HC cumulative emissions 50 seconds after engine startup for respectively 0, 10, and 20 seconds of postheating, as a function of zero-flow preheating and airflow preheating durations. (a, b, c) airflow rate 10 kg/h, post heating of 0, 10, and 20 seconds, respectively. (d, e, f) airflow rate 30 kg/h, post heating of 0, 10, and 20 seconds, respectively. (g, h, i) airflow rate 45 kg/h, post heating of 0, 10, and 20 seconds, respectively. Accumulated emissions are normalized with respect to the passive heating results 50 seconds after engine startup.